



**HAL**  
open science

# the research of optical and electrical properties on nanowire LED and photodetector

Hezhi Zhang

► **To cite this version:**

Hezhi Zhang. the research of optical and electrical properties on nanowire LED and photodetector. Optics / Photonic. Université Paris Saclay (COMUE), 2016. English. NNT : 2016SACLS096 . tel-01323953v2

**HAL Id: tel-01323953**

**<https://theses.hal.science/tel-01323953v2>**

Submitted on 15 Jun 2016

**HAL** is a multi-disciplinary open access archive for the deposit and dissemination of scientific research documents, whether they are published or not. The documents may come from teaching and research institutions in France or abroad, or from public or private research centers.

L'archive ouverte pluridisciplinaire **HAL**, est destinée au dépôt et à la diffusion de documents scientifiques de niveau recherche, publiés ou non, émanant des établissements d'enseignement et de recherche français ou étrangers, des laboratoires publics ou privés.

NNT : 2016SACLS096

THESE DE DOCTORAT  
DE  
L'UNIVERSITE PARIS-SACLAY  
PREPAREE A  
UNIVERSITE PARIS-SUD

ECOLE DOCTORALE N °575  
Electical, Optical, Bio-physics and Engineering (EOBE)  
Institut d'Électronique Fondamentale (IEF)

Spécialité de doctorat PHYSIQUE  
Par

**Hezhi Zhang**

la recherche des propriétés optiques et électriques sur les nanofils LEDs et photodétecteur

Thèse présentée et soutenue à Orsay, le 10 Mai 2016:

**Composition du Jury :**

<b>M, Julien, François</b>	Directeur de recherche UNIVERSITE PARIS-SUD	Président
<b>M, Schwarz, Ulrich</b>	professor TU Chemnitz	Rapporteur
<b>M, Larrieu, Guilhem</b>	Chargé de recherche LAAS	Rapporteur
<b>Mme, Tchernycheva, Maria</b>	Chargé de recherche UNIVERSITE PARIS-SUD	Directeur de thèse
<b>Mme Blandine Alloing</b>	Chargé de recherche CHREA	Invité
<b>M, Christophe Durand</b>	Chargé de recherche CEA-INAC	Invité

**Titre :** la recherche des propriétés optiques et électriques sur les nanofils LEDs et photodétecteur

**Mots clés :** diodes électroluminescentes (LED), photodétecteurs, nanofils, InGaN / GaN, structure cœur/coquille

**Résumé :** Le premier chapitre résume brièvement les propriétés de base des semi-conducteurs nitrures et décrit les méthodes d'élaboration des nanofils. Dans le deuxième chapitre, je présente mon travail sur la fabrication et la caractérisation de LED à nanofil unique InGaN/GaN ayant un contact transparent en graphène pour l'injection des trous.

Dans le troisième chapitre, je décris la fabrication et la caractérisation des LEDs à nanofils uniques fabriqués à partir d'une matrice de nanofils verticaux avec une morphologie des contacts identique à celle mise en œuvre pour les LEDs à base d'ensemble de nanofils.

Le dernier chapitre est consacré à l'étude des photodétecteurs à nanofils de nitrure. Je décris d'abord la fabrication et la caractérisation d'un photodétecteur de rayonnement ultraviolet basé sur un ensemble de nanofils de GaN avec un contact transparent en graphène. Ensuite, des détecteurs à nanofils uniques InGaN / GaN ont été fabriqués fonctionnant dans la gamme spectrale du visible à ultraviolet. Dans la dernière partie, je présente une technique pour la fabrication de photodétecteurs flexibles basée sur des ensembles de nanofils verticaux et je discute leurs performances.

**Title :** the research of optical and electrical properties on nanowire LED and photodetector

**Keywords :** light emitting diodes (LEDs), photodetectors, nanowires, InGaN/ GaN, core/shell structure

**Abstract :** First chapter briefly summarizes the nitride semiconductor basic properties and discusses the present status of nanowire elaboration. In the second chapter, I present my work on the fabrication and in-depth characterization of single nanowire InGaN/GaN LEDs with a transparent graphene contact for hole injection. Reference single wire LEDs with metal contacts are also investigated for comparison.

In the third chapter, I describe the fabrication and characterize single wire LEDs made out of a vertical NW array with the contacting scheme identical to array LEDs. The dependence of the electroluminescence on the contact morphology opens the way to control the LED emission color at the device processing stage.

The last chapter is dedicated to the study of nitride nanowire photodetectors. I first describe the fabrication and characterization of a GaN ultraviolet (UV) photodetector based on a NW array with a transparent graphene contact. Moreover, single NW InGaN/GaN detectors were fabricated operating in the visible to ultraviolet spectral range. In the last part, I present an up-to-date technique for fabricating flexible photodetectors based on vertical NW arrays and I discuss their performances.



# Table of Contents

<b>Abstract</b> .....	<b>IV</b>
<b>R ésum é</b> .....	<b>VI</b>
<b>Chapter 1 General Introduction</b> .....	<b>1</b>
1.1 Basic properties of III-nitride semiconductors.....	1
1.1.1 Crystalline structure.....	1
1.1.2 Material properties of wurtzite III-nitride structure.....	3
1.1.3 Polarity of III-nitride materials.....	5
1.2 Growth of GaN nanowires.....	10
1.2.1 Catalyst-assisted “ vapor-liquid-solid” (VLS) growth.....	10
1.2.2 Catalyst-free GaN nanowires growth .....	14
I.Molecular beam epitaxy (MBE) growth.....	14
II.Metal Organic Chemical Vapor Phase Deposition (MOCVD) growth .....	17
1.3 Conclusion.....	21
<b>Chapter 2 In-plane InGaN/GaN Core–Shell Single Nanowire Light Emitting Diodes with Graphene-BasedP-Contact</b> .....	<b>27</b>
2.1 Introduction .....	27
2.2 InGaN/GaN core-shell nanowire growth and sample structure.....	30
2.3 Optical properties.....	32
2.3.1 Photoluminescence spectroscopy .....	32
2.3.2 Cathodoluminescence spectroscopy .....	32
2.4 Device fabrication .....	34
2.5 Device characterization .....	36
2.5.1 Electrical characterization.....	36
2.5.2 Electron beam induced current characterization .....	37
2.5.3 Electroluminescence characterizations.....	40
2.5.5 Cathodoluminescence mapping.....	41

2.6 Electrical model of the nanowire LEDs.....	44
2.7 Conclusion.....	50
<b>Chapter 3 characterization of vertical single and array NWs LEDs.....</b>	<b>54</b>
3.1 Nanowires growth method .....	56
3.2 Nanowire internal structure .....	56
3.3 Optical properties .....	57
3.3.1 Micro-photoluminescence spectroscopy .....	57
3.3.2 Cathodoluminescence spectroscopy .....	58
3.4 Single nanowire LEDs.....	60
3.4.1 Fabrication of single nanowire LEDs.....	60
3.4.2 Electrical characterization of single nanowire LEDs .....	62
3.4.3 Electroluminescence of single nanowire LEDs.....	63
3.5 Array LED color control by a post-growth treatment .....	66
3.5.1 Processing of array LEDs with different contacting schemes .....	65
3.5.2 Electrical characterization of array LEDs with different contacting schemes .....	68
3.5.3 EBIC characteristics of array LEDs with different contacting schemes .....	69
3.5.4 Electroluminescence of array LEDs with different contacting schemes .....	70
3.6 EBIC signal transient at the core/under layer interface of n-GaN.....	73
3.7 Correlation between EBIC maps and electroluminescence maps .....	79
3.8 Front n-contact LED.....	81
3.9 Conclusions.....	87
<b>Chapter 4: Nitride single nanowire and nanowire array photodetectors....</b>	<b>91</b>
4.1 GaN NW array ultraviolet photodetectors with a graphene transparent contact.....	94
4.1.1 NWs synthesis .....	94
4.1.2 Device fabrication .....	95
4.1.3 Device characterization .....	97
4.1.4 Conclusion .....	99
4.2 single InGaN/GaN core-shell NW photodetectors .....	100
4.2.1 InGaN/GaN core/shell NWs growth method.....	101

4.2.2 Optical properties .....	102
4.2.3 Fabrication process of single InGaN/GaN core/shell NW photodetectors .....	103
4.2.4 Characterization of photodetectors with a localized metal contact .....	105
4.2.5 Characterization of photodetectors with ITO conformal contact .....	108
4.2.6 Conclusion.....	117
4.3 Flexible vertical InGaN/GaN core-shell NW photodiodes.....	119
4.3.1 Fabrication of the flexible photodetectors .....	119
4.3.2 Device characterization .....	120
4.3.3 Conclusion.....	126
<b>Chapter 5 General conclusion.....</b>	<b>129</b>
Appendix A: list of Abbreviations .....	132
Appendix B: list of publication .....	134
Appendix C: Code of silvaco of 30MQWs photodetector .....	136
Appendix D: Synth èse en Fran çais.....	142

## Abstract

III-nitride semiconductors have known a strong regain of interest at the end of 1990's thanks to the successful demonstration of p-type doping, which has enabled a large palet of applications such as light emitting diodes (LEDs), laser diodes (LDs), photodetectors and solar cells. However, the material quality remains the key issue for thin film nitride devices. In the recent years, nanostructuring of the active region i the form of one-dimensional nanowires has been proposed as a primissing solution for the material quality problem. Indeed, the efficient strain relaxation allows to fabricate defect-free nanoobjects on lattice-mismatched substrates. In addition, the large lateral surface of nanowires allows to increase the absorption or emitting area by using core/shell heterostructures. Finally, growth along the non-polar m-plane nanowire facets suppresses the internal electrical field and enhances the absorption / emission efficiency.

In this manuscript, I present my work dedicated to the realization and characterization of nitride nanowire light emitters and detectors. I detail the device fabrication using state-of-the-art nanofabrication tools as well as the investigation of their electrical and optical properties.

First chapter briefly summarizes the nitride semiconductor basic properties and discusses the present status of nanowire elaboration. In the second chapter, I present my work on the fabrication and in-depth characterization of single nanowire InGaN/GaN LEDs with a transparent graphene contact for hole injection. Reference single wire LEDs with metal contacts are also investigated for comparison. The electroluminescence of single nanowire LEDs evidences the impact of the contact layout on the emission properties. In particular, the position of the contact determines the spectral evolution with injection current. Namely, for an extended contact and a contact localized on the m-plane, a transition from the green to blue emission is observed whereas for a localized contact on the m-plane/semipolar plane junction the emission remains green.

In the third chapter, I describe the fabrication and characterize single wire LEDs made out of a vertical NW array with the contacting scheme identical to array LEDs. The emission shows a similar evolution as the lateral-contacted single nanowire LEDs. The dependence of the electroluminescence on the contact morphology opens the way to control the LED emission color at the device processing stage. I used fluorine plasma treatment to reduce the conductivity of the p-doped GaN shell for inhibiting the electrical injection in the In-rich region of the quantum well. Furthermore, I analyze the injection

inhomogeneity effect. In order to avoid this effect, I developed a top down contacting scheme with electrons injected directly into n-GaN underlayer, which is called “front contacting” process. The “front contacting” LEDs show an enhanced yield of active nanowires from 19% to 65%.

The last chapter is dedicated to the study of nitride nanowire photodetectors. I first describe the fabrication and characterization of a GaN ultraviolet (UV) photodetector based on a NW array with a transparent graphene contact. Moreover, single NW InGaN/GaN detectors were fabricated operating in the visible to ultraviolet spectral range. The influence of the contact morphology is also investigated by comparing two types of contacts, namely a partial metal contact and an indium tin oxide (ITO) conformal contact, respectively. In the last part, I present an up-to-date technique for fabricating flexible photodetectors based on vertical NW arrays and I discuss their performances.

**Keyword:** light emitting diodes (LEDs), photodetectors, nanowires, InGaN/ GaN, core/shell structure

## Résumé

Les semi-conducteurs III-N ont connu un fort regain d'intérêt à la fin des années 1990 grâce à la démonstration du dopage p du GaN, qui a ouvert la porte à une grande palette d'applications notamment dans le domaine photonique avec des dispositifs comme les diodes électroluminescentes (LEDs), les diodes laser (LDs), les photodétecteurs et les cellules solaires. Cependant, la qualité du matériau reste le problème clé pour les dispositifs à couches minces de nitrure. Dans les dernières années, la nanostructuration de la région active sous forme de nanofils a été proposée comme une solution prometteuse pour améliorer considérablement la qualité du matériau. En effet, la relaxation des contraintes par les bords libres des nanofils permet de fabriquer des nano-objets sans défauts sur des substrats à fort désaccord de maille. En outre, la grande surface latérale des nanofils permet d'augmenter la surface d'absorption ou d'émission en utilisant des hétérostructures cœur/coquille. Enfin, la croissance sur des facettes non polaires des nanofils supprime le champ électrique interne et améliore l'efficacité d'absorption / émission.

Dans ce manuscrit, je présente mon travail dédié à la réalisation et à la caractérisation des émetteurs et détecteurs de lumière à base de nanofils de nitrures. Je détaille la fabrication des dispositifs utilisant des outils de nanofabrication à l'état de l'art, ainsi que l'étude de leurs propriétés électriques et optiques.

Le premier chapitre résume brièvement les propriétés de base des semi-conducteurs nitrures et décrit les méthodes d'élaboration des nanofils. Dans le deuxième chapitre, je présente mon travail sur la fabrication et la caractérisation de LED à nanofil unique InGaN/GaN ayant un contact transparent en graphène pour l'injection des trous. L'électroluminescence des LEDs à nanofils uniques montre l'impact de la forme du contact sur les propriétés d'émission. En particulier, la position du contact détermine l'évolution spectrale avec le courant d'injection. À savoir, pour un contact étendu et un contact localisé sur le plan m, l'émission passe du vert au bleu en fonction du courant d'injection alors que pour un contact localisé sur la jonction entre le plan m et le plan semipolaire l'émission reste verte. Dans le troisième chapitre, je décris la fabrication et la caractérisation des LEDs à nanofils uniques fabriqués à partir d'une matrice de nanofils verticaux avec une morphologie des contacts identique à celle mise en œuvre pour les LEDs à base d'ensemble de nanofils. L'émission montre une évolution similaire à celle observée pour les LEDs à nanofils uniques avec un contact latéral. L'influence de la

morphologie des contacts sur l'électroluminescence ouvre la possibilité de contrôler la couleur d'émission de la LED à l'étape de la fabrication. J'ai utilisé un traitement par plasma de fluor afin de réduire la conductivité de la coquille GaN dopé p et d'inhiber l'injection électrique dans la région riche en In du puits quantique. En outre, j'ai analysé l'effet de l'inhomogénéité d'injection. Afin d'améliorer l'homogénéité, j'ai développé un système de contact par le haut permettant d'injecter les électrons directement dans la sous-couche n-GaN. Les LEDs fabriquées selon cette procédure montrent un rendement amélioré avec 65% de nanofils actifs contre 19% pour une procédure standard.

Le dernier chapitre est consacré à l'étude des photodétecteurs à nanofils de nitride. Je décris d'abord la fabrication et la caractérisation d'un photodétecteur de rayonnement ultraviolet basé sur un ensemble de nanofils de GaN avec un contact transparent en graphène. Ensuite, des détecteurs à nanofils uniques InGaN / GaN ont été fabriqués fonctionnant dans la gamme spectrale du visible à ultraviolet. L'influence de la morphologie de contact est également étudiée en comparant deux types de contacts, à savoir un contact métallique localisé et un contact étendu en oxyde d'indium-étain (ITO). Dans la dernière partie, je présente une technique pour la fabrication de photodétecteurs flexibles basé sur des ensembles de nanofils verticaux et je discute leurs performances.

**Mot-clé** diodes électroluminescentes (LED), photodétecteurs, nanofils, InGaN / GaN, structure cœur/coquille

# Chapter 1 General Introduction

## Table of contents

---

1.1 Basic properties of III-nitride semiconductors .....	1
1.1.1 Crystalline structure .....	1
1.1.2 Material properties of wurtzite III-nitride structure .....	3
1.1.3 Polarity of III-nitride materials .....	5
1.2 Growth of GaN nanowires .....	10
1.2.1 Catalyst-assisted “ vapor-liquid-solid” (VLS) growth .....	10
1.2.2 Catalyst-free GaN nanowires growth .....	14
I. Molecular beam epitaxy (MBE) growth .....	14
II. Metal Organic Chemical Vapor Phase Deposition (MOCVD) growth .....	17
1.3 Conclusion .....	22

---

## 1.1 Basic properties of III-nitride semiconductors

First we focus on the basic materials properties of the III-nitride semiconductors. The nitride material family (gallium nitride (GaN), indium nitride (InN), aluminum nitride (AlN) and their alloys) is of major importance for optoelectronic devices. Other binary III-nitride compounds exist, like boron nitride (BN), but this material is far less used for devices, so it will not be discussed here. GaN, InN and AlN semiconductors share a certain number of common features.

### 1.1.1 Crystalline structure

A stable crystalline phase for nitride materials is the hexagonal phase with a wurtzite structure. Note that it is also possible to obtain a cubic zincblende phase for III-nitrides grown under certain conditions, however this cubic phase is metastable. The wurtzite structure is characterized by an AB

AB sequence along the [0001] direction. For the zincblende structure, it has an ABC ABC stacking in [111] direction. Each atomic layer is rotated in-plane by  $30^\circ$  with respect to the subsequent one. Due to this structural similarity, some structural defects like stacking faults allow the coexistence of hexagonal and cubic phase in the epitaxial layers.

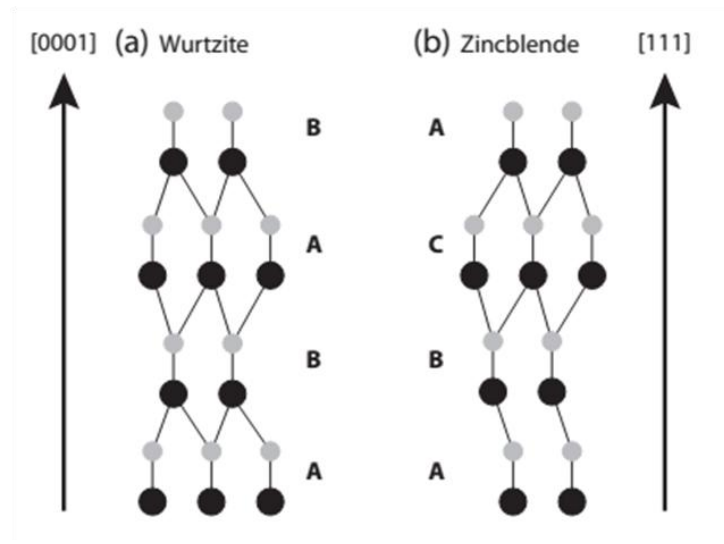


Figure 1.1 Schematic drawings of the (a) AB AB and (b) ABC ABC stacking orders along the polar  $c$ -axis for wurtzite and [111] for zincblende crystals, respectively.

Here we mainly talk about the hexagonal wurtzite structure since it is dominant in nanowires. The wurtzite structure follows the space group  $P63mc$  ( $C_{4v}$ ). A schematic of the wurtzite structure is displayed in Fig. 1.2. The metal atom (Al, Ga and In) and nitrogen atoms are stacked in a hexagonal close-packed system, shifted one with respect to the other along the  $c$ -axis ([0001]). The edge length of the basal hexagon is named by  $a$ , the height of the hexagonal prism  $c$  and, the anion-cation bond length along the [0001] axis  $u$ . The ratio  $u/c$  is a measure of the non-ideality of the crystal in comparison to an ideal wurtzite structure with  $u/c = 3/8 = 0.375$  in the ideal wurtzite lattice. Another measure of the non-ideality is the ratio of lattice constants  $c/a$ , which is equal to  $p=1.633$  for an ideal wurtzite crystal.

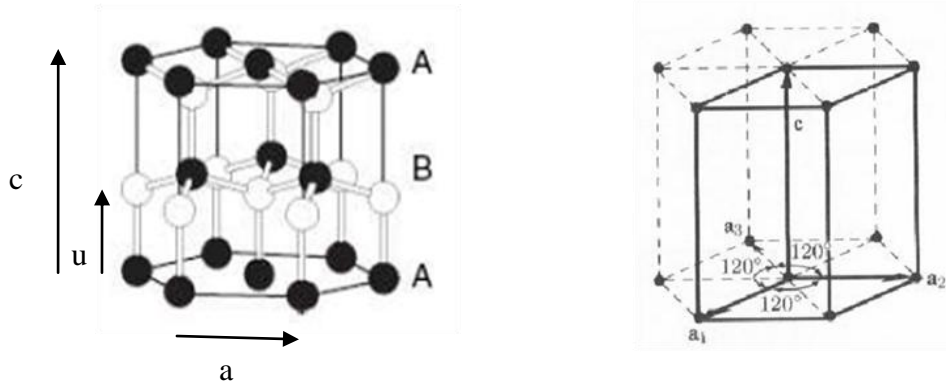


Figure 1.2 Schematic of a wurtzite crystal.

### 1.1.2 Material properties of wurtzite III-nitride semiconductors

The importance of the III-nitrides for the optoelectronic industry comes from the fact that they are wide bandgap semiconductors. Their bandgap is direct, which allows for efficient light emission. According to data that adorned the literature for years, the established bandgap values are 0.6 eV for InN<sup>[1]</sup>, 3.42 eV for GaN<sup>[2]</sup>, and 6.0 eV<sup>[3]</sup> for AlN at room temperature. The variation of the band gap with temperature is given by the Varshni law<sup>[4]</sup>:

$$E_g(T) = E_g(0) - \frac{\alpha T^2}{\beta + T} \quad (1.1)$$

where  $E_g(0)$  is the bandgap energy at 10 K. The parameters  $\alpha$  and  $\beta$  are tabulated in table 1.1, taking into account the electron-phonon interaction.

Quantity	symbol	AlN	GaN	InN	(Unit)
Crystal structure <sup>[2]</sup>		W	W	W	
Gap		Direct	Direct	Direct	
Lattice constant <sup>[2]</sup>	$A_0=$	3.112	3.189	3.545	Å
Thermal expansion <sup>[2]</sup>		4.2	5.6	3.8	$10^{-6}/K$
Lattice constant <sup>[2]</sup>	$C_0=$	4.982	5.185	5.703	Å
Thermal expansion <sup>[2]</sup>		5.3	3.2	2.9	$10^{-6}/K$
$c/a$ <sup>[2]</sup>		1.601	1.626	1.680	
$u/c$ <sup>[2]</sup>		0.379	0.376	0.378	
Bandgap energy <sup>[1][2][3]</sup>	$E_g=$	6.0	3.42	0.6	eV
Varshni parameter <sup>[2]</sup>	$\alpha$	1.799	0.909	0.414	meV/K
	$\beta$	1462	830	454	K

Table 1.1 summarizes the values of bandgap energy, Varshni parameters, the lattice parameters including  $a$  and  $c$ , the metal-N bond length  $u$ , and the  $c/a$  and  $u/c$  ratios for GaN, AlN and InN at room temperature. The thermal expansion coefficients are also displayed in table 1.1.

The bandgaps of the three binary compounds cover a broad spectral range (Table 1.1), from the ultraviolet (6.0 eV for AlN) to the infrared (0.6 eV for InN). For the majority of applications, combinations of binary compounds are used to synthesize ternary alloys. Their bandgaps vs lattice parameters are displayed in Figure. 1.3. The evolution of the bandgap of ternary alloys as a function of the composition is non-linear, they are bent following Eq. (1.2) for an  $A_{1-x}B_xN$  alloy<sup>[2]</sup>:

$$E_g(x) = E_g(AN) (1-x) + E_g(BN) x - b x (1-x) \quad (1.2)$$

with  $b$  the bowing parameter, given by Table 1.2 for each ternary alloy.

	AlN-GaN	GaN-InN	AlN-InN
Alloy bandgap bowing <sup>[5][6][7]</sup>	0.62	1.43	4.9

Table 1.2 Bowing parameters of ternary alloys.

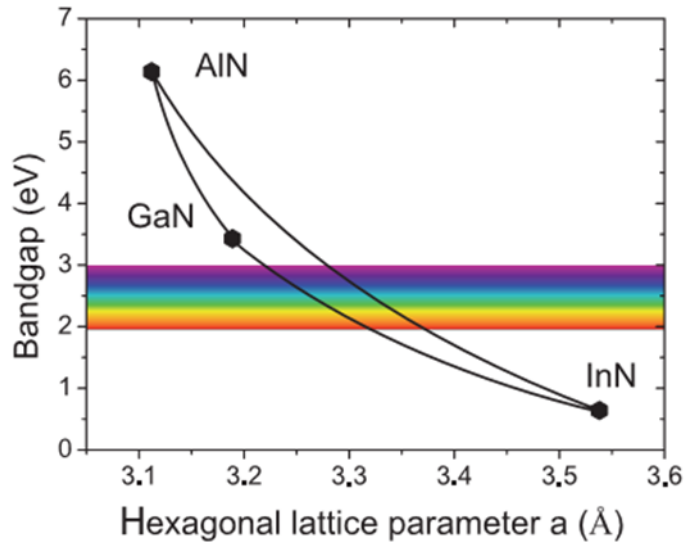


Figure 1.3. Bandgap energy as a function of in-plane lattice parameter for III-nitrides compounds<sup>[5][6][7]</sup>.

### 1.1.3 Polarity of III-nitride materials

The wurtzite structure has a polar axis due to the lack of a symmetry inversion center<sup>[8][9][10]</sup> (Figure 1.4). The polarity is determined by the direction of the vector associated to the metal-N bond along the [0001] axis. The c-axis is defined positive when such a vector points from the metal atom towards the N atom, as illustrated in Figure 1.4(a). In this case, the polarity of the crystal is called polarity [0001], metal or Al-, Ga-, In-polarity. The basal surface shows the cations (Al, Ga or In) on the top position of the (0001) bilayer. On the contrary, if the basal surface of the (0001) bilayer shows the N anions, the polarity corresponds to [000-1], or N-polarity.

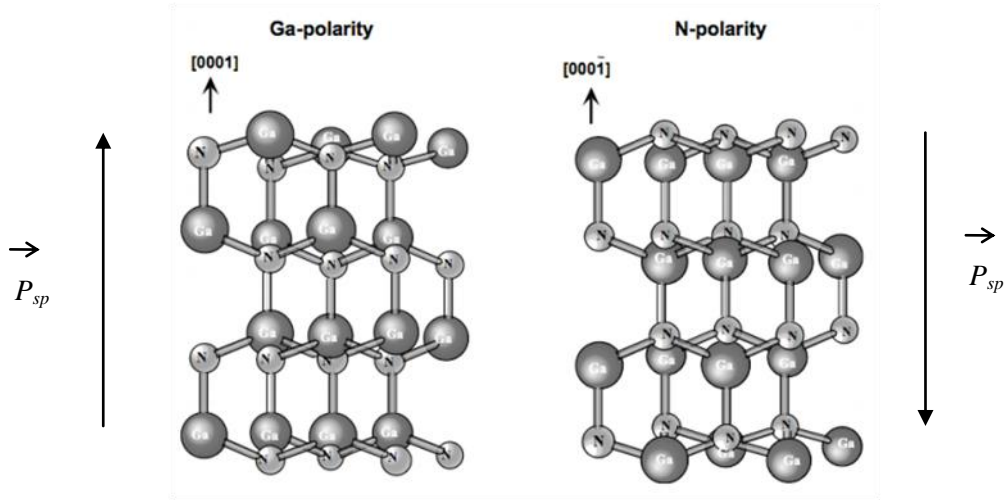


Figure 1.4 Ga-face and N-face polarities in a wurtzite GaN structure.

Since nitrogen atoms have a smaller atomic radius and higher ionization energy than metal atoms, nitrogen atoms are more electronegative than metal atoms and bonds can be considered as an electrostatic dipole. This charge distribution in the tetrahedron is not compensated by the atomic stacking because of the noncentrosymmetric nature along the [0001]-direction, resulting thus in a macroscopic spontaneous polarization ( $\vec{P}_{sp}$ )<sup>[11][12]</sup> in nitride materials. Theoretical values of spontaneous polarization given by Vurgaftman et al<sup>[2]</sup>. are presented in Table 1.3. As seen in Fig. 1.4,  $\vec{P}_{sp}$  points from the metal- to the N-atom, being thus negative for metal-face and positive for N-face crystals. The increase of the  $\vec{P}_{sp}$  magnitude in nitrides, from GaN to InN and finally to AlN, is related to the deviation of the lattice from the ideal wurtzite structure given by the  $u/c$  and  $c/a$  parameters in Table 1.1.

	AlN	GaN	InN
Spontaneous polarization ( C/m2 ) <sup>[2]</sup>	-0.09	-0.034	-0.042

Table 1.3 Spontaneous polarization for wurtzite-type GaN, AlN and InN.<sup>[2]</sup>

Stress modifies the atomic positions in the crystal leading to a different spatial distribution of the charges and inducing a piezoelectric polarization ( $\vec{P}_{pz}$ )<sup>[11][12]</sup>. Usually, III-nitrides are grown on the (0001)-plane and the layers show a biaxial stress perpendicular to the [0001]-axis due to the lattice and thermal mismatch between the substrate and the layer. In this case, the piezoelectric polarization in each direction is given by<sup>[13][14]</sup>

$$\vec{P}_{pz}^x = \vec{P}_{pz}^y = 0 \quad 1.3$$

$$\vec{P}_{pz}^z = 2 \frac{a - a_0}{a_0} \left[ e_{31} - e_{33} \left( \frac{c_{13}}{c_{33}} \right) \right] \quad 1.4$$

Then, the piezoelectric field is positive (i.e. in the [0001]-direction) or negative (i.e. in the [000-1]-direction) if the material is under compressive strain ( $a < a_0$ ) or tensile strain ( $a > a_0$ ), respectively. The total polarization of the layer is the sum of the spontaneous and piezoelectric polarizations. Table 1.4 shows the piezoelectric coefficients for III-nitrides<sup>[2]</sup>.

	AlN	GaN	InN
$e_{31}$ ( C/m <sup>2</sup> )	-0.50	-0.35	-0.57
$e_{33}$ ( C/m <sup>2</sup> )	1.79	1.27	0.97

Table 1.4: Piezoelectric coefficients  $e_{31}$  and  $e_{33}$  for GaN, AlN and InN.<sup>[2]</sup>

Due to the discontinuity of the piezoelectric and spontaneous polarizations, the nitride heterostructures exhibit bound charges at the interfaces, which affect the properties of the whole structure as detailed below<sup>[14][15]</sup>.

InGaN light emitting diodes (LEDs)<sup>[16][17]</sup> and laser diodes (LDs)<sup>[18][19]</sup> are based on a sandwich-type structure made of GaN/InGaN/GaN layers, where the difference in bandgap creates a quantum well (QW) structure, the so-called InGaN QW. The smaller bandgap of the InGaN layer leads to a trapping of the holes and electrons from the valence and conduction band, respectively. The recombination of

the excitons (electron-hole pairs) takes place in the InGaN QWs as schematically displayed in Figure 1.5 (a) showing an InGAN/GaN QW in the absence of internal field. The confinement leads to the quantification of the energy states in the QW. Usually the recombination occurs between the ground state in the QW conduction band and the heavy hole (A-band) in the valence band. On the other side, the above mentioned piezoelectric and spontaneous polarizations are important for polar structures. Indeed, the polarization discontinuity at the interfaces leads to building of surface charges, which create an electric field in the QWs. This results in a band-bending and leads to a red-shift of the emission wavelength<sup>[20]</sup>, but also to a strong reduction in the overlap of the electron and hole wavefunctions as illustrated in Figure 1.5 (b). This effect is known as the Quantum Confined Stark Effect (QCSE). The reduced overlap strongly lowers the radiative-recombination probability and thus strongly affects the emission efficiency. While the red-shift allows one to reach longer wavelengths with lower indium content, the reduced efficiency is detrimental for the device performance.

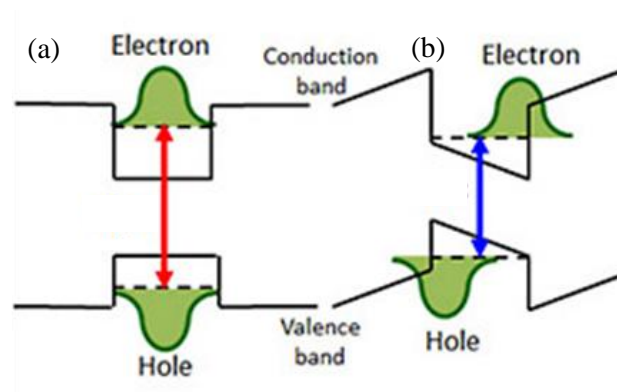


Figure 1.5 Schematics of a single InGaN quantum well structure (a) without and (b) with internal electric field.

Therefore, it is desirable to grow InGaN-GaN heterostructures with reduced or completely suppressed internal fields. This is possible by performing the growth on crystal facets perpendicular to the  $c$ -plane, i.e. for the  $\{1-100\}$   $m$ - and  $\{11-20\}$   $a$ - plane of GaN as shown in figure 1.6 (b) and (c). For facet orientations having an intermediate angle with the  $c$ -axis, the internal fields are typically reduced, but not zero (examples of these planes are shown in figure 1.6(a) to (e)); hence, the respective crystal planes are called ‘semipolar’. For about 10 years, the idea to reduce the internal fields by using non- or semipolar crystal facets has triggered a huge number of research studies worldwide<sup>[21][22][23][24][25][26]</sup>.

Among these studies, nanowire devices open a way to grown III-nitride material along m- plane or a-plane using the deposition on the sidewalls.

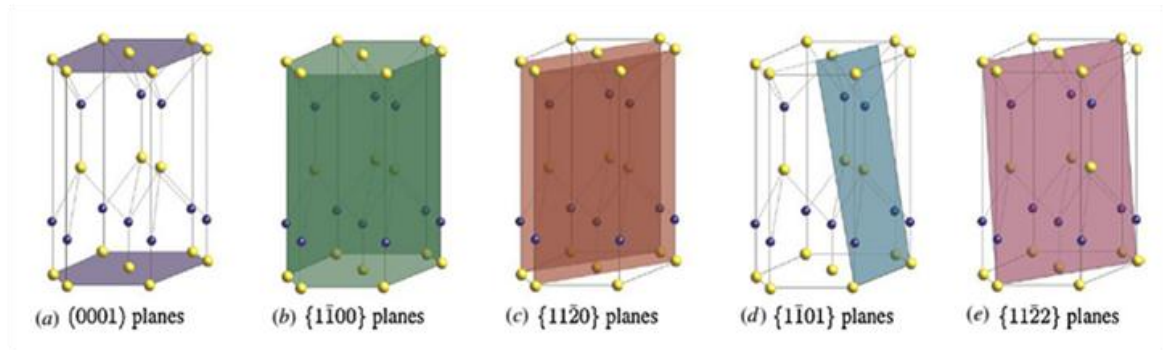


Figure 1.6 Different crystallographic planes in GaN.

Another challenge present for the thin film growth is the large number of dislocations emerging during the growth due to the difference of lattice parameters with the substrate, which are called “misfit dislocations”<sup>[27]</sup>. The most common dislocation type in wurtzite systems are threading dislocations which propagate through the whole film, from the interface with the substrate to the surface of the layer. The mismatch problem has less consequences on the crystal quality in nanostructures because of their small diameter allowing strain to be relaxed laterally (figure 1.7(b)) in contrast with the planar growth where strain can only be relaxed along one dimension (figure 1.7(a)). Indeed, defect free GaN nanowire growth has been demonstrated on highly mismatched substrate such as sapphire<sup>[28][29]</sup>, and also low-cost substrates: Si (111)<sup>[30]</sup> and Si (001)<sup>[31]</sup>.

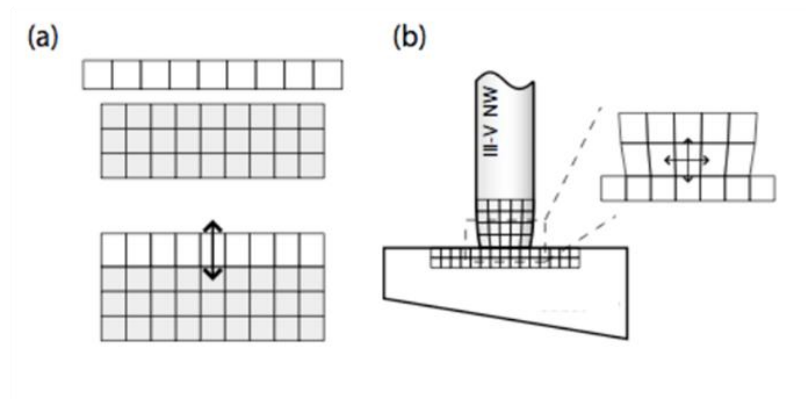


Figure 1.7 Illustration of the Si/III-V interface. (a) Planar growth for normal heterointerface, strain can only be relaxed along one dimension. (b) NW growth, strain can be relaxed laterally, allowing 3D strain relaxation.

## 1.2 Growth of GaN nanowires

### 1.2.1 Catalyst-assisted “vapor-liquid-solid” (VLS) growth

In 1964, Wagner and Ellis first described the VLS growth method on Si whiskers with Au as a catalyst <sup>[32]</sup>. The growth mechanism can be explained as follows: Si atoms enter the Au from the gas phase forming Au-Si alloy. As the Au drop becomes super-saturated, Si precipitates in solid form at the liquid/solid interface with the substrate, and crystal growth takes place selectively under the Au particle.

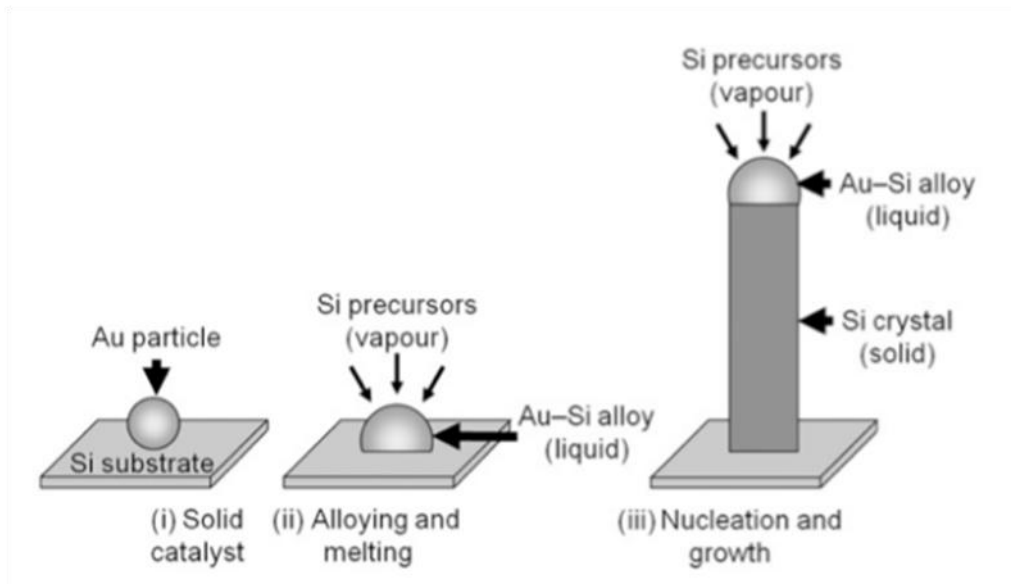


Figure 1.7 Schematic illustration of the VLS growth of Si wires using an Au catalyst particle. The grey arrow, and labels (i), (ii) and (iii) illustrate the different stages of nanowire growth

Similar to Si, GaN nanorods have also been achieved by the VLS growth method by using Au<sup>[33][34]</sup>, Ni<sup>[35]</sup> and Ta<sup>[36]</sup> as a catalyst. Figures 1.8 (a) and (b) illustrate GaN VLS growth method with Au<sup>[33]</sup>. Figure 1.8 (c) proves that most of GaN nanorods are well aligned vertically with respect to the Si (111) substrate.

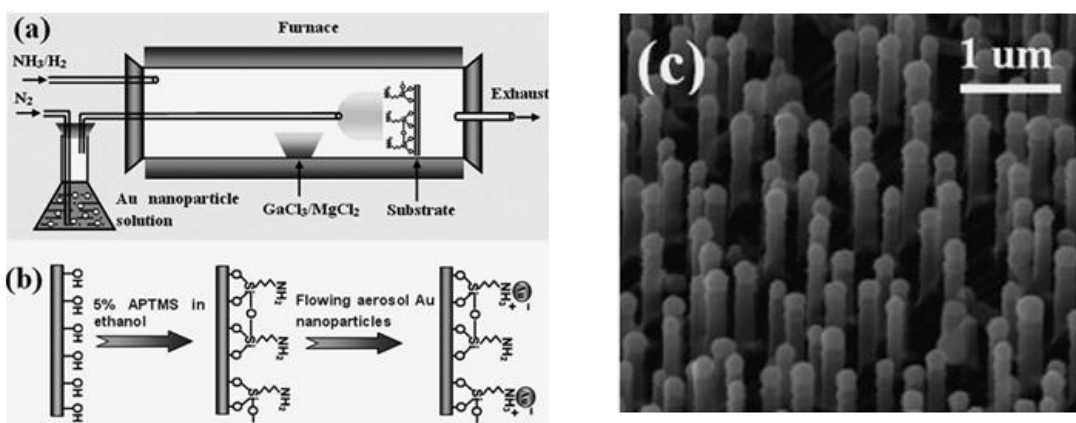


Figure 1.8 (a) and (b) illustrate the GaN VLS growth method using an Au catalyst. (c) SEM image of GaN nanorods<sup>[33]</sup>.

In 2004, Qian et.al<sup>[37]</sup> used these high quality p-type GaN nanowires to realize radial heterostructures for nanophotonics. The well-defined doped n-GaN/InGaN/p-GaN core/shell nanowire heterostructures provided a new strategy for efficient carrier injection. Photoluminescence (PL) data further show that the optical properties are controlled by the core/shell structure with a strong emission from the InGaN layer centered at 448 nm. Electrical measurements with separate contacts to the core and outer shell have demonstrated that these core-shell nanowires behave as p-n diodes with a blue light emission arising from the electron-hole recombination in the InGaN layer.

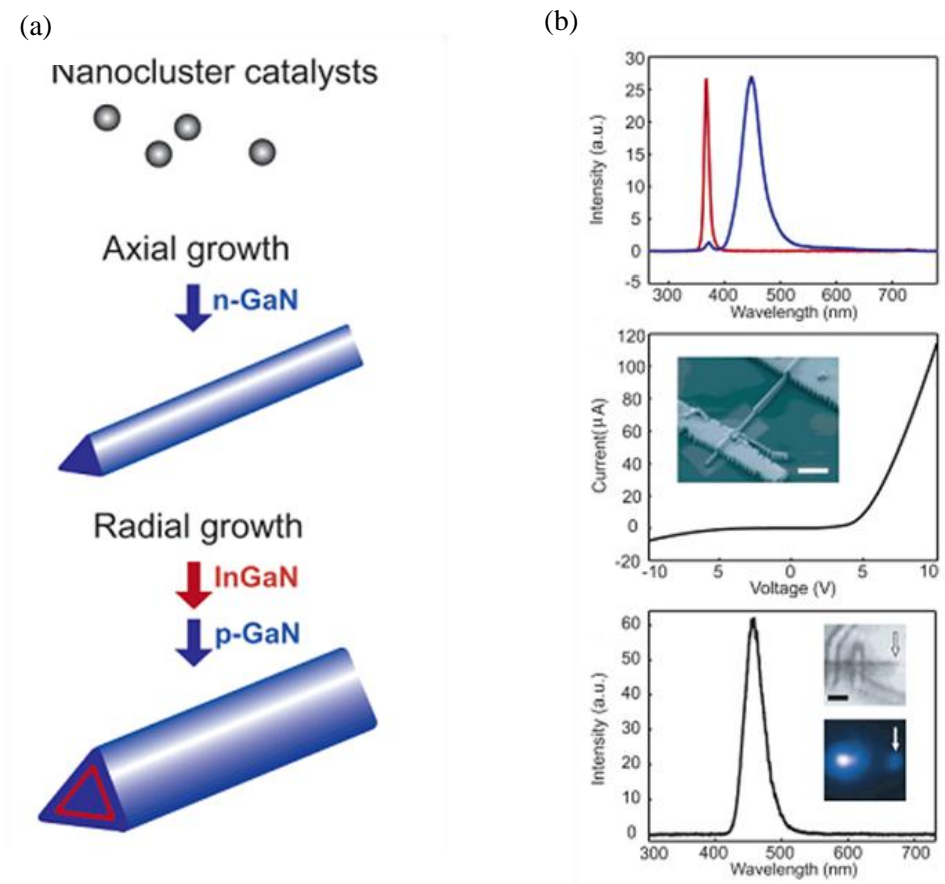


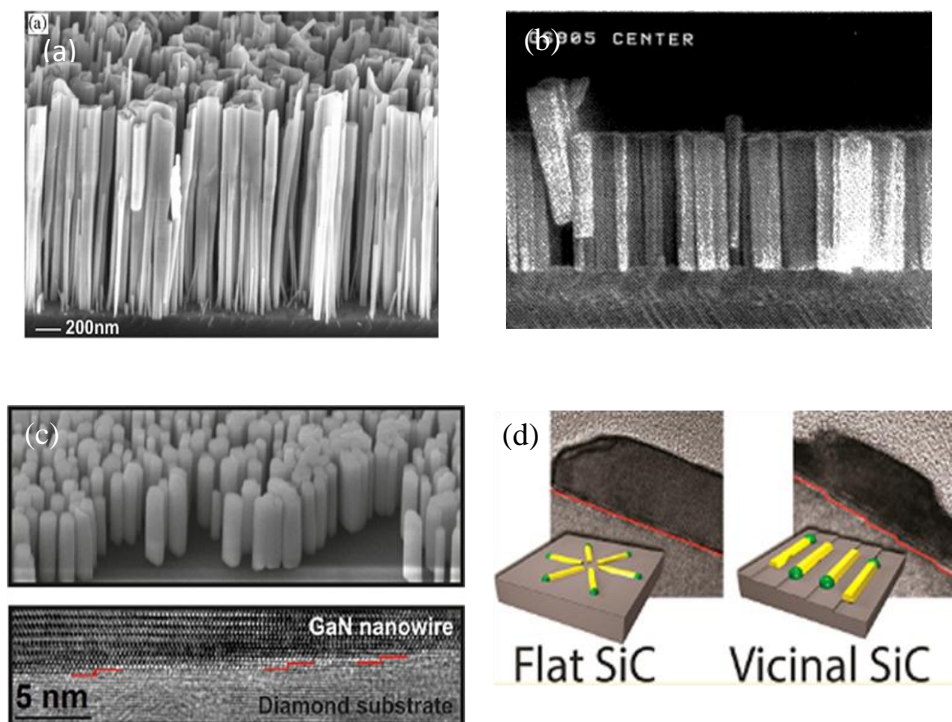
Figure 1.9 (a) Synthesis of core-shell nanowire heterostructures. (b) Optoelectronic properties of n-GaN/InGaN/p-GaN core-shell nanowires<sup>[38]</sup>.

Nevertheless, the GaN nanowires grown via a VLS growth mode often present defects such as a tilt, twist, intersect and branch. For large scale and industrial solid-state lighting application, this growth method may not be suitable due to these defects as well as the difference in height and orientation of GaN nanorods.

## 1.2.2 Catalyst-free GaN nanowires growth

### I. Molecular beam epitaxy growth

The GaN nanowires have been synthesized by catalyst-free plasma assisted molecular-beam epitaxy (MBE) growth. Several groups have reported the self-induced growth of GaN NWs on various substrates such as Si<sup>[30][31][38]</sup>, sapphire<sup>[29]</sup>, diamond<sup>[39]</sup> and silicon carbide (SiC)<sup>[40]</sup>. Figures 1.10 (a), (b), (c) and (d) show GaN NWs growth on Si, sapphire, diamond and SiC, respectively.



The figures 1.10 (a), (b), (c) and (d) present SEM images of GaN NWs on Si<sup>[30][31][38]</sup>, sapphire<sup>[29]</sup>, diamond<sup>[39]</sup> and SiC<sup>[40]</sup>, respectively.

Among these substrates, single crystalline Si substrates are commonly used today to fabricate catalyst-free GaN NWs. The growth method and mechanism have been studied intensively. Bertness et al<sup>[41]</sup>. demonstrated that inserting an AlN layer buffer between the Si and GaN NWs is essential to

improve the growth (in particular, the nanowire verticality) and the thickness of the buffer is also a key parameter for controlling morphology of the NWs. They discussed the nucleation mechanism and showed that the GaN nanorods nucleate not on top of the AlN layer, but are rather highly correlated with the formation of hexagonal pits with  $\{1-102\}$  facets

Furthermore, the growth processes was also investigated by Ristic et al<sup>[42]</sup>. During the nucleation process, the substrate surface is covered by GaN islands of different sizes as shown in figure 1.11 (a). When the nucleus reaches its critical size, the NW starts to grow on GaN islands. Some NWs start to grow earlier than others due to different nucleation times, resulting in a height dispersion. The Ga diffuses along the NWs sidewalls up to the apex. The wider the NWs, the slower is its growth rate. The following steps depend on two contributions 1) Ga atom impinging on the nanowire apex will incorporate directly to the crystal; 2) Ga atoms arriving to the substrate surface will diffuse to the nanorods base, climb along the lateral sidewalls up to their apex and incorporate to the crystal as shown by the diagram in Figure 1.11 (b).

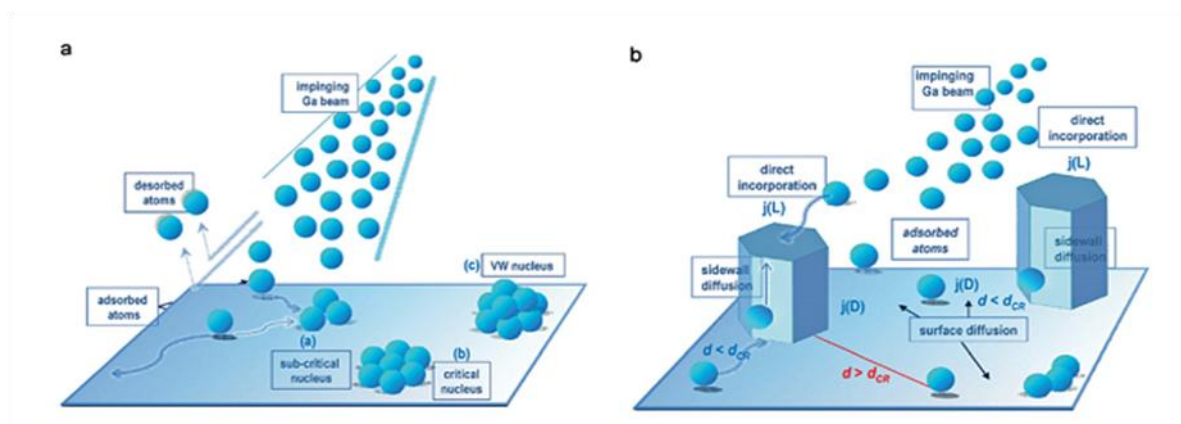


Figure 1.11 Diagram showing how nucleation proceeds by Volmer-Weber growth mode <sup>[42]</sup>.

For the MBE growth, the V/III ratio is also a critical parameter. Normally, a high aspect ratio GaN nanorod growth requires high V/III ratios. As illustrated in Figure 1.12, the high V/III ratio leads to a GaN nanorod growth, while a low V/III (Ga-rich) allows a 2D layer growth <sup>[43]</sup>.

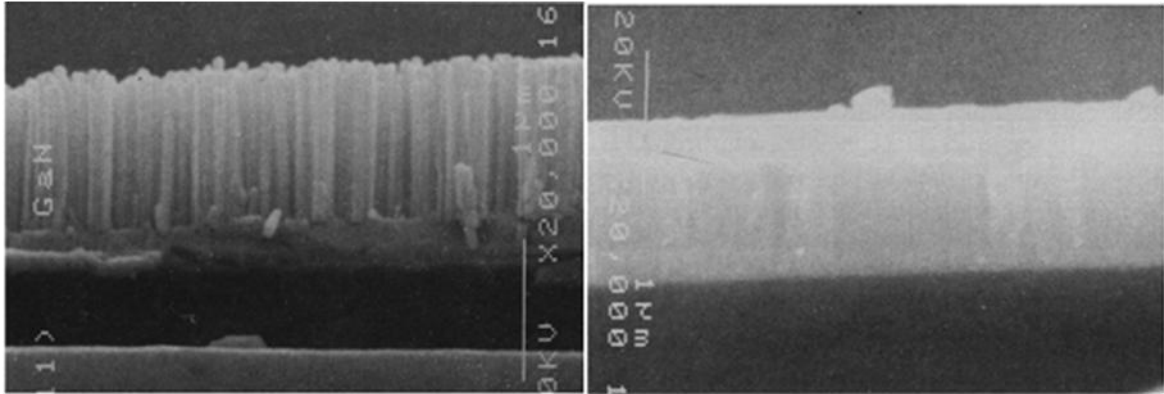


Figure 1.12 SEM micrographs of two GaN layers grown directly on Si (111) substrates under different flux conditions: (a) N-rich and (b) Ga-rich<sup>[43]</sup>.

Organized GaN nanocolumns grown by MBE have been fabricated by Hiroto et al<sup>[44]</sup>. They used patterned Ti film as a selective area growth (SAG) mask. The diameters of the mask openings were designed from 100 nm to 250 nm. They found that the selectivity can only be achieved at high temperature above 900 °C. The mechanism of SAG was simply explained in terms of the dependence of the desorption and diffusion of Ga adatoms on Ti.

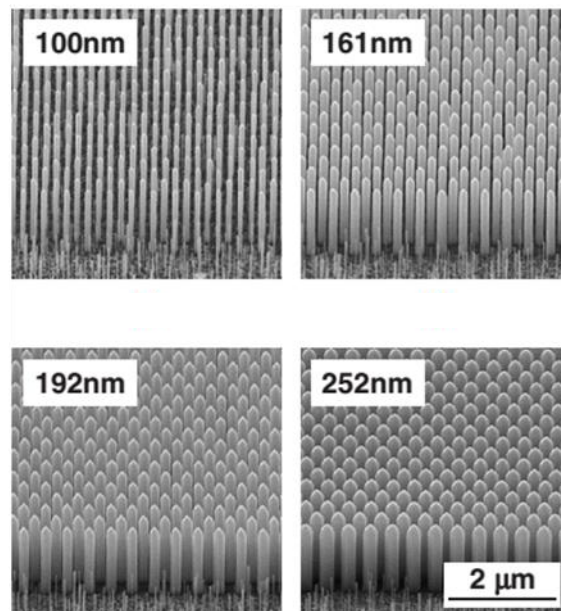


Figure 1.13 The SEM image of GaN nanowires grown by MBE on a patterned Ti mask<sup>[44]</sup>.

The formation mechanisms of GaN nanowires grown by SAG has been explained in detail by Gacevic et al<sup>[45]</sup> who showed that the formation of SAG GaN NWs proceeded in two stages, driven by SAG kinetics and free-surface energy minimization, respectively. The first growth stage consists of the following three steps: initial nucleation at the nano hole inner periphery (driven by Ga adatom diffusion on a discontinuous surface), coalescence onset, and full coalescence, finishing when the growing nanocrystal fills the entire nanohole area. In the second growth stage, the nanocrystal undergoes morphological evolution through unstable cylindrical-like and dodecagonal shapes, ending when the thermodynamically stable hexagonal NW is formed.

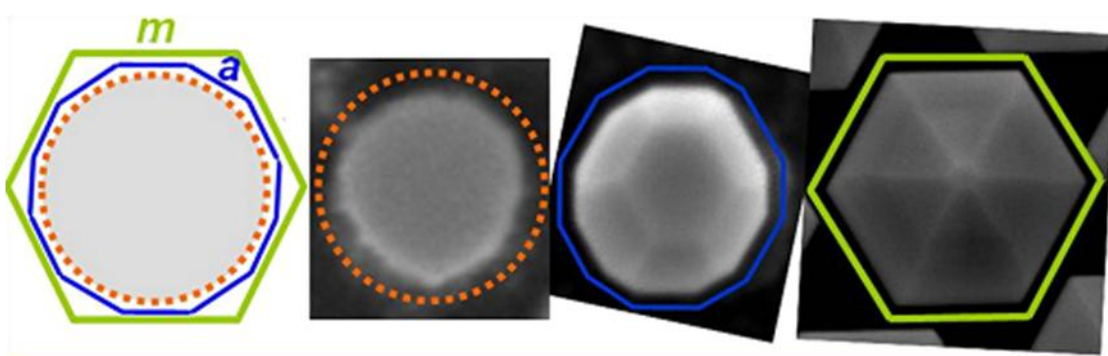


Figure 1.14 Explanation of the formation mechanisms of GaN nanowires grown by SAG<sup>[47]</sup>

## II. Metal Organic Chemical Vapor Phase Deposition growth

GaN nanowires synthesis by MOCVD was first achieved on patterned templates. In 2006, Hersee et. al<sup>[28]</sup> presented the growth of high quality GaN nanowires and uniform nanowire arrays. For their experiment, a 30 nm silicon nitride mask was deposited on GaN film for defining the position of each GaN nanowire. A pulsed MOCVD was used allowing the nanowire diameter to remain constant after the nanowires had emerged from the selective growth mask. The SEM image of selective area growth GaN by MOCVD is shown in figure 1.15.

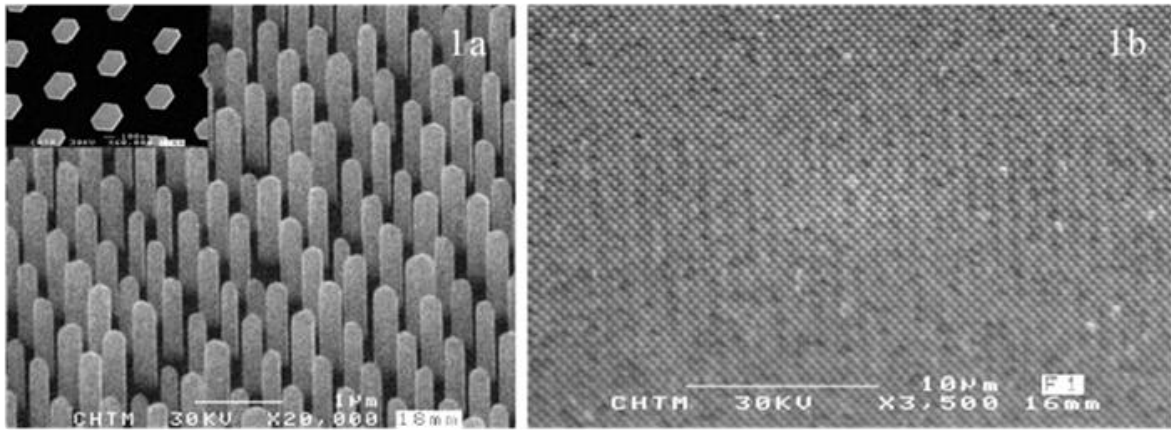


Figure 1.15 Scanning electron micrograph of a GaN nanorod array consisting of 1  $\mu\text{m}$  GaN nanorods (The inset shows a top view and reveals the hexagonal symmetry of the nanorods). (b) A lower magnification SEM image reveals the long-range order of the GaN nanorod arrays <sup>[28]</sup>.

In 2010, the continuous-flux growth of GaN nanorod has been reported<sup>[46]</sup>. The nanorods were grown on a patterned sapphire with  $\text{SiO}_2$  mask layer. It was found that the nanowire structure is dependent on the  $\text{H}_2/\text{N}_2$  ratio. The lower  $\text{H}_2/\text{N}_2$  ratio produces a pyramidal structure, while a higher  $\text{H}_2/\text{N}_2$  ratio leads to a nanorod structure growth. The diameter of nanorods is inversely proportional to the  $\text{H}_2/\text{N}_2$  ratio.

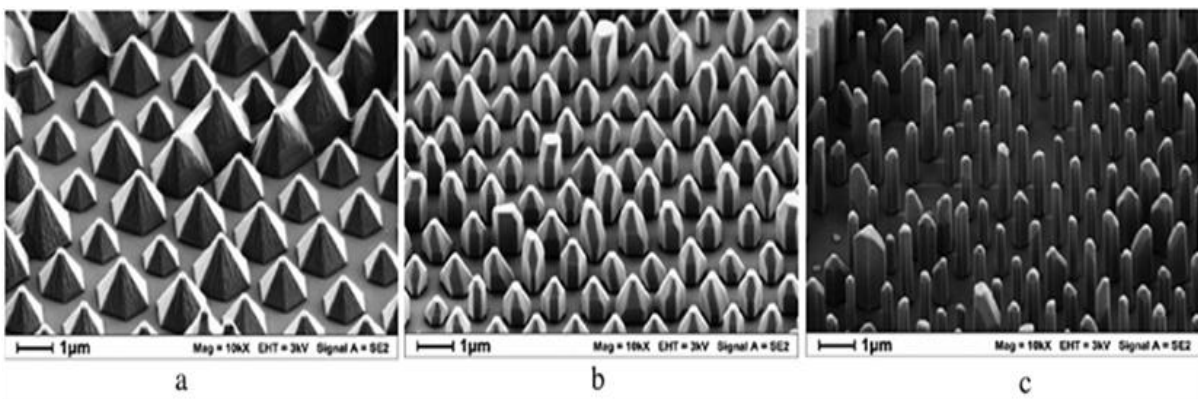


Figure 1.16 (a) Growth with pure nitrogen as carrier gas leads to pyramidal-shaped GaN growth, (b) whereas nanorod growth occurs with  $\text{H}_2/\text{N}_2$  carrier gas mixture of 1/2, and (c) still improves for  $\text{H}_2/\text{N}_2$  carrier gas mixture of 2/1<sup>[46]</sup>.

Moreover, the morphology of GaN nanorods also has a strong relationship with Ga polar and N polar

nature of the crystal. In 2012, Li et al. reported nitrogen-polar core-shell GaN LEDs grown by selected area MOVPE<sup>[47]</sup>. The nanorods were grown on a SiO<sub>2</sub> patterned N-polar GaN/sapphire substrate. The nanowires show clear vertical sidewalls and the top part has a flat platform, which is different with the growth on a Ga polar substrate. In 2013, the Ga polar GaN nanocolumn LED grown by continuous-flow MOVPE has been realized by Wang et. al<sup>[48]</sup>. The Ga polar LEDs show a pyramidal GaN structure, which has an evident {10-11} facet boundary. This can be explained by the fact that, for Ga polar orientation, the r-planes {10-11} or {10-1-1} are terminated by N atom, which can be passivated by hydrogen. Thus, the r-plane keeps stable and has a low growth rate.

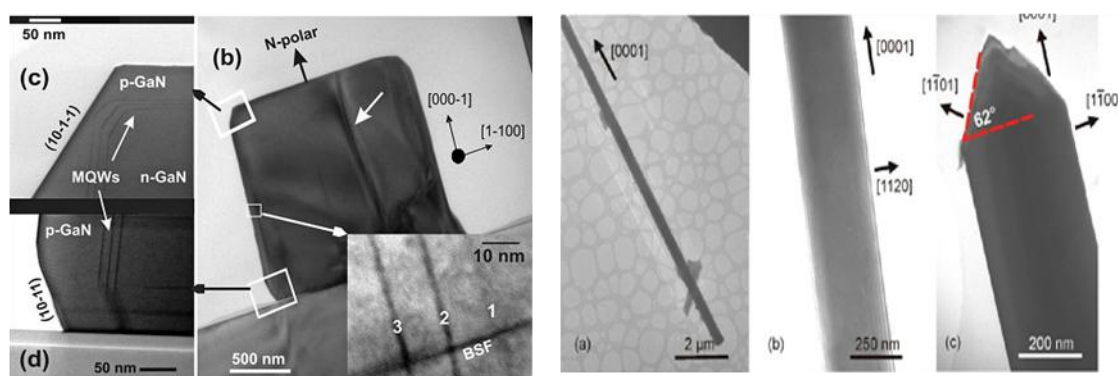


Figure 1.17 SEM image of GaN naowires grown on N polar<sup>[47]</sup> and Ga polar<sup>[48]</sup>.

Self-assemble GaN single-crystal nanowires have been reported in 2010 by Koester et.al<sup>[49]</sup>. The self-assembled nanowires are grown directly on c-plane sapphire without depositing neither a buffer layer nor a mask. The nanowire growth is promoted by a thin SiN<sub>x</sub> layer (2nm) to enable a vertical growth of c-oriented wires with 200-1500 nm diameters. The GaN seed nucleation time determines the mean diameter and the structure quality.

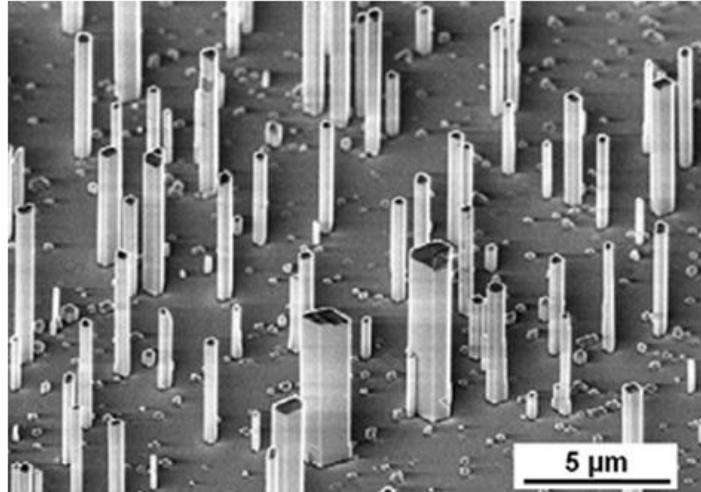


Figure 1.18 SEM image of self-assembled GaN nanowires grown on c-plane sapphire<sup>[49]</sup>

Wang et al<sup>[50]</sup> reported the growth mechanism of catalyst-free self-organized GaN nuclei and three-dimensional columns on sapphire by MOVPE. They performed temperature and time dependent growth studies. They found that the growth behaviour can be characterized by two different kinetic regimes: mass-transport-limited growth and thermodynamically limited growth. The sum of the activation energies for the thermodynamic barrier of nucleation and for the surface diffusion/mass-transport limitation, i.e.  $W_{\text{het}} + Ed$ , is 0.57 eV in the ‘low’-temperature region and 2.43 eV in the “high”-temperature region. GaN columns grown under the same conditions have a comparable height, which is not dependent on their diameter or on the distance to other columns. Therefore, the growth rate is presumably limited by the incorporation rate on the top surface of columns. The height and diameter at the top of the GaN columns increase linearly with time and no height limit is observed.

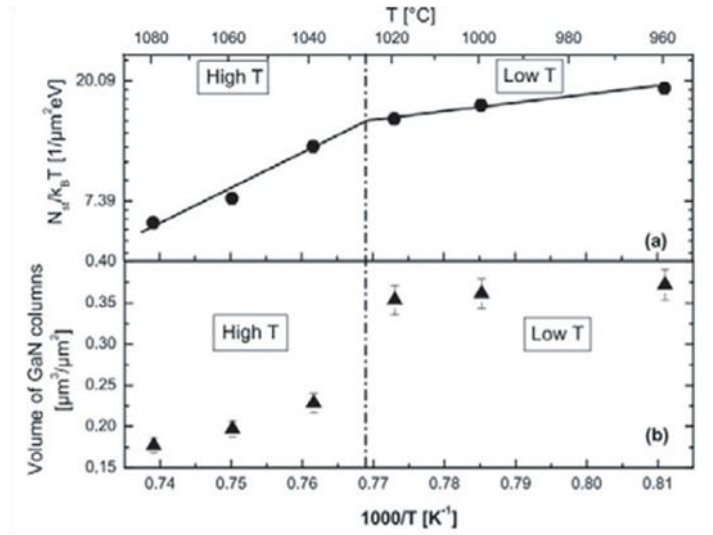


Figure 1.19 The growth mechanism of catalyst-free self-organized GaN nuclei and three-dimensional columns on sapphire<sup>[50]</sup>

## 1.3 Conclusion

In this chapter, first I summarize the basic physical properties of III-nitride materials. The wurtzite structure of III-nitride alloys leads to the strong internal electrical fields induced by spontaneous and piezoelectric polarizations, which significantly reduce the efficiency of optical devices such as solar cells or LEDs. One of the promising solutions to get rid of this effect is to make use of III-nitride NWs for devices. Several growth methods are reviewed including the VLS, and catalyze-free growth by MEB and MOCVD method. The different morphologies obtained are analyzed by controlling the growth conditions. In the next three chapters, I will present the NWs optical devices grown mainly by MOVPE and discuss their performance. I will provide the state of art for the different devices in the corresponding chapters.

## References

- [1] Haddad, D. B., et al. "Optical and electrical properties of low to highly-degenerate InN films." *MRS Proceedings*. Vol. 798. Cambridge University Press, 2003.
- [2] Vurgaftman, I., and J. R. Meyer. "Band parameters for nitrogen-containing semiconductors." *Journal of Applied Physics* 94.6 (2003): 3675-3696.
- [3] Silveira, E., et al. "AlN bandgap temperature dependence from its optical properties." *Journal of Crystal Growth* 310.17 (2008): 4007-4010.
- [4] Varshni, Yatendra Pal. "Temperature dependence of the energy gap in semiconductors." *Physica* 34.1 (1967): 149-154.
- [5] Wu, J., et al. "Narrow bandgap group III - nitride alloys." *physica status solidi (b)* 240.2 (2003): 412-416.
- [6] Lee, S. R., et al. "The band-gap bowing of Al<sub>x</sub>Ga<sub>1-x</sub>N alloys." *Applied physics letters* 74.22 (1999).
- [7] Terashima, Wataru, et al. "Growth and characterization of AlInN ternary alloys in whole composition range and fabrication of InN/AlInN multiple quantum wells by RF molecular beam epitaxy." *Japanese journal of applied physics* 45.6L (2006): L539.
- [8] Northrup, John E., Jörg Neugebauer, and L. T. Romano. "Inversion domain and stacking mismatch [9] boundaries in GaN." *Physical review letters* 77.1 (1996): 103.
- Hellman, E. S. "The polarity of GaN: a critical review." *MRS Internet Journal of Nitride Semiconductor Research* 3 (1998): e11.
- [10] Austerman, Stanley B., and William G. Gehman. "The inversion twin: prototype in beryllium oxide." *Journal of Materials Science* 1.3 (1966): 249-260.
- [11] Bernardini, Fabio, Vincenzo Fiorentini, and David Vanderbilt. "Spontaneous polarization and piezoelectric constants of III-V nitrides." *Physical Review B* 56.16 (1997): R10024.
- [12] Ambacher, O., et al. "Role of Spontaneous and Piezoelectric Polarization Induced Effects in Group - III Nitride Based Heterostructures and Devices." *physica status solidi (b)* 216.1 (1999): 381-389.
- [13] Takeuchi, Tetsuya, et al. "Quantum-confined Stark effect due to piezoelectric fields in GaInN

strained quantum wells." *Japanese Journal of Applied Physics* 36.4A (1997): L382.

[14] Yu, E. T., et al. "Spontaneous and piezoelectric polarization effects in III–V nitride heterostructures." *Journal of Vacuum Science & Technology B* 17.4 (1999): 1742-1749.]

[15] Waltereit, P., et al. "Nitride semiconductors free of electrostatic fields for efficient white light-emitting diodes." *Nature* 406.6798 (2000): 865-868.

[16] Nakamura, Shuji, Masayuki Senoh, and Takashi Mukai. "High - power InGaN/GaN double - heterostructure violet light emitting diodes." *Applied Physics Letters* 62.19 (1993): 2390-2392.

[17] Nakamura, Shuji, et al. "High-brightness InGaN blue, green and yellow light-emitting diodes with quantum well structures." *Japanese Journal of Applied Physics* 34.7A (1995): L797.

[18] Nakamura, Shuji. "The roles of structural imperfections in InGaN-based blue light-emitting diodes and laser diodes." *Science* 281.5379 (1998): 956-961.

[19] Nakamura, Shuji, et al. "InGaN-based multi-quantum-well-structure laser diodes." *Japanese Journal of Applied Physics* 35.1B (1996): L74.

[20] Chichibu, S. F., et al. "Effective band gap inhomogeneity and piezoelectric field in InGaN/GaN multiquantum well structures." *Applied Physics Letters* 73.14 (1998): 2006.

[21] Tyagi, Anurag, et al. "Semipolar (1011) InGaN/GaN laser diodes on bulk GaN substrates." *Japanese journal of applied physics* 46.5L (2007): L444.

[22] Enya, Yohei, et al. "531 nm green lasing of InGaN based laser diodes on semi-polar {2021} free-standing GaN substrates." *Applied Physics Express* 2.8 (2009): 082101.

[23] Yeh, Ting-Wei, et al. "InGaN/GaN multiple quantum wells grown on nonpolar facets of vertical GaN nanorod arrays." *Nano letters* 12.6 (2012): 3257-3262.

[24] Koester, Robert, et al. "M-plane core–shell InGaN/GaN multiple-quantum-wells on GaN wires for electroluminescent devices." *Nano letters* 11.11 (2011): 4839-4845.

[25] Zhang, Hezhi, et al. "Color control of nanowire InGaN/GaN light emitting diodes by post-growth treatment." *Nanotechnology* 26.46 (2015): 465203.

[26] Tchernycheva, M., et al. "InGaN/GaN core–shell single nanowire light emitting diodes with graphene-based p-contact." *Nano letters* 14.5 (2014): 2456-2465.

- [27] Ning, X. J., et al. "Growth defects in GaN films on sapphire: The probable origin of threading dislocations." *Journal of materials research* 11.03 (1996): 580-592.
- [28] Hersee, Stephen D., Xinyu Sun, and Xin Wang. "The controlled growth of GaN nanowires." *Nano letters* 6.8 (2006): 1808-1811.
- [29] Wang, George T., et al. "Highly aligned, template-free growth and characterization of vertical GaN nanowires on sapphire by metal-organic chemical vapour deposition." *Nanotechnology* 17.23 (2006): 5773.
- [30] Calarco, Raffaella, et al. "Nucleation and growth of GaN nanowires on Si (111) performed by molecular beam epitaxy." *Nano letters* 7.8 (2007): 2248-2251.
- [31] Guo, Wei, et al. "Catalyst-free InGaN/GaN nanowire light emitting diodes grown on (001) silicon by molecular beam epitaxy." *Nano letters* 10.9 (2010): 3355-3359.
- [32] Wagner, R. S., and W. C. Ellis. "Vapor - liquid - solid mechanism of single crystal growth." *Applied Physics Letters* 4.5 (1964): 89-90.
- [33] Tang, Yong - Bing, et al. "Controllable Synthesis of Vertically Aligned p - Type GaN Nanorod Arrays on n - Type Si Substrates for Heterojunction Diodes." *Advanced Functional Materials* 18.21 (2008): 3515-3522.
- [34] Liu, Baodan, et al. "Quasi-aligned single-crystalline GaN nanowire arrays." *Applied Physics Letters* 87.7 (2005): 73106-73106.
- [35] Li, Qiming, and George T. Wang. "Improvement in aligned GaN nanowire growth using submonolayer Ni catalyst films." *Applied Physics Letters* 93.4 (2008): 043119.
- [36] Shi, Feng, Hong Li, and Chengshan Xue. "Fabrication of GaN nanowires and nanorods catalyzed with tantalum." *Journal of Materials Science: Materials in Electronics* 21.12 (2010): 1249-1254.
- [37] Qian, Fang, et al. "Gallium nitride-based nanowire radial heterostructures for nanophotonics." *Nano letters* 4.10 (2004): 1975-1979.
- [38] Meijers, R., et al. "GaN-nanowhiskers: MBE-growth conditions and optical properties." *Journal of crystal growth* 289.1 (2006): 381-386.
- [39] Schuster, Fabian, et al. "Self-assembled GaN nanowires on diamond." *Nano letters* 12.5 (2012): 2199-2204.
- [40] Tsivion, David, and Ernesto Joselevich. "Guided growth of epitaxially coherent GaN nanowires

on SiC." *Nano letters* 13.11 (2013): 5491-5496.

[41] Bertness, K. A., et al. "Spontaneously grown GaN and AlGa<sub>N</sub> nanowires." *Journal of Crystal Growth* 287.2 (2006): 522-527.

[42] Ristić, Jelena, et al. "On the mechanisms of spontaneous growth of III-nitride nanocolumns by plasma-assisted molecular beam epitaxy." *Journal of crystal growth* 310.18 (2008): 4035-4045.

[43] Sanchez-Garcia, M. A., et al. "The effect of the III/V ratio and substrate temperature on the morphology and properties of GaN-and AlN-layers grown by molecular beam epitaxy on Si (1 1 1)." *Journal of crystal growth* 183.1 (1998): 23-30.

[44] Kishino, K., et al. "Selective-area growth of GaN nanocolumns on titanium-mask-patterned silicon (111) substrates by RF-plasma-assisted molecular-beam epitaxy." *Electronics Letters* 44.13 (2008): 819-821.

[45] Gačević, Žarko, Daniel Gómez Sánchez, and Enrique Calleja. "Formation mechanisms of GaN nanowires grown by selective area growth homoepitaxy." *Nano letters* 15.2 (2015): 1117-1121.

[46] Bergbauer, W., et al. "Continuous-flux MOVPE growth of position-controlled N-face GaN nanorods and embedded InGa<sub>N</sub> quantum wells." *Nanotechnology* 21.30 (2010): 305201.

[47] Li, Shunfeng, et al. "Nitrogen-polar core-shell GaN light-emitting diodes grown by selective area metalorganic vapor phase epitaxy." *Applied Physics Letters* 101.3 (2012): 032103.

[48] Wang, Xue, et al. "Continuous-flow MOVPE of Ga-polar GaN column arrays and core-shell LED structures." *Crystal Growth & Design* 13.8 (2013): 3475-3480.

[49] Köster, Robert, et al. "Self-assembled growth of catalyst-free GaN wires by metal-organic vapour phase epitaxy." *Nanotechnology* 21.1 (2009): 015602.

[50] Wang, Xue, et al. "Mechanism of nucleation and growth of catalyst-free self-organized GaN columns by MOVPE." *Journal of Physics D: Applied Physics* 46.20 (2013): 205101.

# Chapter 2: In-plane InGaN/GaN Core–Shell Single Nanowire Light Emitting Diodes with Graphene-Based P-Contact

## Table of contents

---

2.1 Introduction .....	27
2.2 InGaN/GaN core-shell nanowire growth and sample structure.....	30
2.3 Optical properties .....	32
2.3.1 Photoluminescence spectroscopy .....	32
2.3.2 Cathodoluminescence spectroscopy .....	32
2.4 Device fabrication .....	34
2.5 Device characterization .....	36
2.5.1 Electrical characterization.....	36
2.5.2 Electron beam induced current characterization.....	37
2.5.3 Electroluminescence characterizations .....	40
2.5.5 Cathodoluminescence mapping .....	41
2.6 Electrical model of the nanowire LEDs .....	44
2.7 Conclusion.....	50

---

## 2.1 Introduction

### *Advantages of nanowire-based LEDs*

Light emitting diodes (LEDs) based on InGaN materials are a timely subject of research aimed to improve the efficiency and reduce the cost of solid state lightning. Despite the achieved high performance and the ongoing development of thin film LEDs, nanostructured materials appear to be a promising way to further boost their performance.

Indeed, three-dimensional nanowire-based LEDs can improve the crystal quality of material. They also offer new opportunities for strain engineering. Moreover, the core-shell geometry makes it possible to increase the active surface for the same physical surface which is expected to reduce the

efficiency droop at high injection current. For nanowires having their elongated axis aligned with the [0001] direction, this geometry eliminates the Quantum Confined Stark Effect (QCSE) thanks to the growth of the active region on non-polar m-planes<sup>[1][2]</sup>.

#### ***New functionalities enabled by nanowires***

Additionally, the nanowires open the way for making light sources with new functionalities. For example, thanks to the dependence of the indium concentration on the wire diameter, it is possible to change the nano-LEDs emitting color on the same substrate by changing the size of nano-apertures of the patterned substrate<sup>[3][4]</sup>. Thanks to their small diameter, the nanowires can be transferred to flexible substrates such as plastic or metal for making bendable LEDs<sup>[5][6]</sup>.

Besides macroscopic LEDs, single nanowires can also be used to fabricate bright and ultra-compact light sources. The nanowire LEDs can be removed from the original substrate and subsequently embedded in planar photonic circuits<sup>[7][8]</sup>. They can also be used in a vertical architecture as point light sources for optical stimulation in biomedical applications<sup>[9]</sup> or for making micro-array pixels<sup>[10]</sup>.

#### ***State of the art of nanowire-based LEDs***

First nanowire-based LEDs have used an axial heterostructure with an active region containing GaN/InGaN multiple quantum wells (in this case called "quantum discs") embedded between n- and p-doped segments, respectively. With this geometry, Kim et al.<sup>[11]</sup> have shown a nanowire LED emitting at 470 nm grown by HVPE and Kikuchi, et al.<sup>[12]</sup> have demonstrated a nanowire-based LED grown by MBE with an emission wavelength tuned from blue to red. LEDs using a core-shell structure containing InGaN/GaN multiple quantum wells on lateral facets appeared soon after the first demonstrations of axial devices. The first core/shell LED was demonstrated by the Lieber's group at Harvard using a catalyzed nanowire growth<sup>[13]</sup>. This pioneering achievement was followed by numerous studies using a catalyze-free growth<sup>[14][15]</sup> and later the selective area growth<sup>[16][17]</sup>. Currently, large industrial groups (e.g. OSRAM) as well as start-ups (e.g. GLO, Aledia) invest a lot of efforts to bring organized nanowires LED technology to maturity in order to propose a commercial product able to compete with planar LED technology.

Organized growth following the selective area epitaxy procedure allows for a much better control of the wire morphology in comparison with spontaneous growth. It reduces the composition fluctuation between the nanowires and thus facilitates the control of the emission wavelength and the spectral

broadening. However, the complexity of the three-dimensional growth makes it difficult to control the homogeneity of In concentration inside the quantum well resulting in In gradients and the formation of In rich regions. In particular, the change of the emission color with the injection current was observed not only in self-assembled nanowires<sup>[6][15]</sup>, but also in organized nanowire LEDs<sup>[8][18][19]</sup>. The transition from a 2D to a 3D geometry also affects the electrical and optical properties of the LEDs.

### ***Graphene electrodes for single nanowire LEDs***

The integration of graphene electrodes with one-dimensional semiconductor nanostructures has recently attracted a strong interest. The graphene/nanowire hybrid materials have demonstrated their promise for a broad range of optoelectronic devices, such as, for example, photodetectors<sup>[20][21]</sup> or LEDs<sup>[22][23][24]</sup>. Single nanowire/graphene LEDs have been demonstrated using ZnO, CdS, and CdSe materials<sup>[25]</sup>. However, until my PhD work, no single wire InGaN/GaN LEDs with graphene contact have been reported. The main benefits of a graphene transparent contact are its enhanced transparency, high conductivity, mechanical robustness, and flexibility. These properties in particular enable the fabrication of flexible nanowire-based LEDs or of novel photonic platforms combining nanoscale active optical elements on flexible substrates. Single wire LEDs with graphene contacts present also a fundamental interest. Indeed, taking advantage of the graphene good transparency to photons and electrons, the properties of these nanoscale devices can be studied by a wide range of complementary characterization techniques such as cathodoluminescence (CL), charge collection microscopies, or scanning near-field optical microscopy in order to achieve a complete understanding of the device physics.

### ***Summary of the chapter***

In this chapter, I present my work on the fabrication and in-depth characterization of single nanowire InGaN/GaN LEDs with a transparent graphene contact for hole injection. Core-shell n-p junction nanowires with a radial InGaN QWs were grown by MOVPE on GaN/sapphire templates with a SiN<sub>x</sub> hard mask patterned by nanoimprint lithography. The epitaxy was performed by O. Kryliouk at GLO-AB. The nanowire array shows excellent wire-to-wire morphological and compositional homogeneity confirmed by CL studies. Single wire LEDs were fabricated using a metal contact for electron injection and a transparent graphene sheet structured by e-beam lithography for hole injection. Reference single wire LEDs with metal contacts to both p and n parts as well as an LED sample based

on the nanowire array were also fabricated for comparison. The fabrication procedure was validated by electrical measurements. Electron beam induced current (EBIC) mapping of the single nanowire LEDs has shown that for graphene-contacted devices, the radial p-n junction produces an electrical current homogeneous over the cylindrical part of the nanowire, whereas a signal reduction toward the wire top is observed for metal-contacted reference device. Single wire LEDs with graphene contact present efficient electroluminescence starting from  $\sim 0.16 \mu\text{A}$  injection current. The EL is peaked at 494 nm at low injection, whereas for high injection the spectrum becomes dominated by a peak at 415 nm. The reference LEDs exhibit a similar spectral behavior with injection current. The high resolution CL on cleaved nanowires allows to unambiguously attribute the high energy EL peak to the emission of the radial QW on the m-planes, whereas the low energy peak arises from the In-rich region at the junction between the m-planes and the semipolar planes. A simple electrical model is developed showing that at low injection, the current is concentrated in the upper nanowire part in correspondence to the In-rich region; however, at high current, the injection in the lower nanowire part covered with the graphene electrode becomes more favorable.

## 2.2 InGaN/GaN core-shell nanowire growth and sample structure

The InGaN/GaN core-shell organized nanowires have been grown by MOVPE on n-doped GaN/sapphire templates with an SiN mask with submicrometer openings. The mask has been patterned by nanoimprint lithography and dry etching. First n<sup>+</sup>-doped GaN core is formed (doping concentration of about  $1 \times 10^{19} \text{ cm}^{-3}$ ), then it is laterally overgrown with an n-doped GaN layer with a lower doping concentration ( $\sim 5 \times 10^{18} \text{ cm}^{-3}$ ), an undoped 5-10 nm thick InGaN QW, an AlGaIn electron blocking layer, and a p-doped GaN exterior shell (thickness  $\sim 150 \text{ nm}$ , Mg concentration about  $\sim 5 \times 10^{19} \text{ cm}^{-3}$ ). The growth is terminated with a p<sup>+</sup>-doped GaN surface layer to achieve a low contact resistance. This growth procedure results in a homogeneous array of identical nanowires with a density of  $5 \times 10^7 \text{ nanowire/cm}^2$  as illustrated in Figure 2.1(a). The total nanowire height is 2.5  $\mu\text{m}$ , and the diameter is 0.9  $\mu\text{m}$ . The nanowires have a cylindrical shape with a hexagonal cross section over the lower 2  $\mu\text{m}$  with lateral facets defined by m planes. The top pyramidal part is formed by semipolar (10-11) planes. Figure 2.1(b) displays a schematic of the nanowire internal structure.

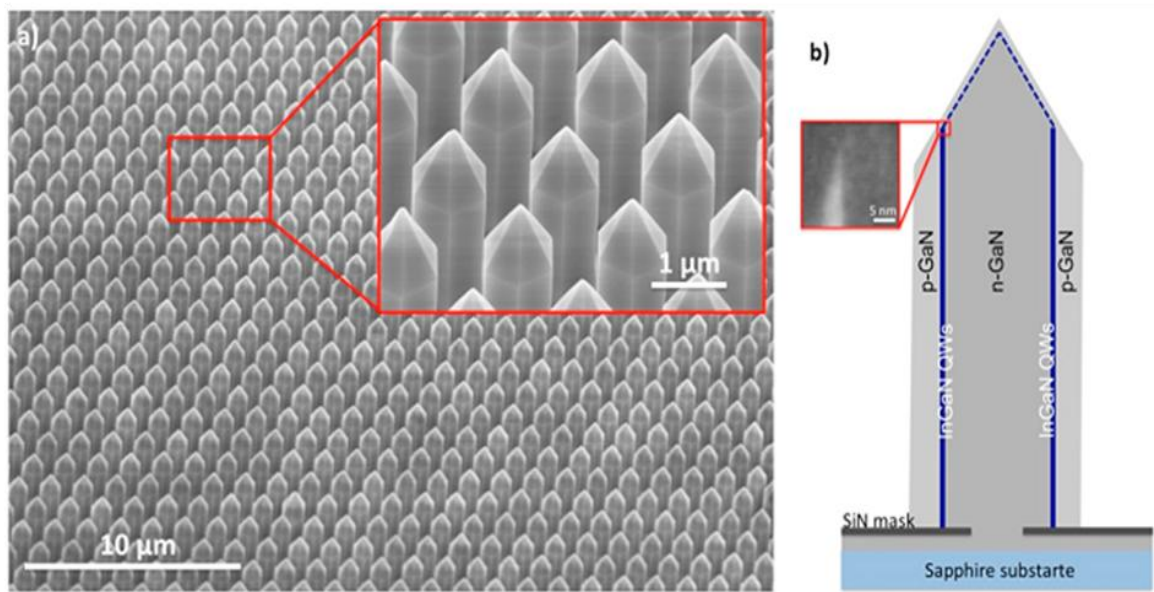


Figure 2.1 (a) SEM image of a nanowire array. (b) Schematic of the nanowire structure. The inset shows a TEM image of the region at the junction between the m-plane and the semipolar plane.

The growth conditions have been optimized in order to minimize the growth on the semipolar planes. A transmission electron microscopy study on a sample grown under similar conditions has revealed that the thickness of the InGaN QW is less than 0.5 nm on the semipolar plane to be compared with 5-10 nm on the m-planes (cf. inset of Figure 2.1(b)). Therefore, no luminescence from InGaN on semipolar planes is expected, which is indeed confirmed by CL maps as discussed in the following. The thickness of the p-doped GaN shell is also strongly reduced at the semipolar planes down to  $\sim 20$  nm. This part of the shell is expected to be depleted and therefore strongly resistive. The QW thickness is found to be homogeneous over the m-plane except for the top region at the m-plane and semipolar plane junction, which is slightly broadened. The CL studies have evidenced the presence of an In gradient in the QW. By using the dependence of the InGaN bandgap on the In content, the composition of the QW is estimated to be 10% (15%) in the lower (medium) nanowire part. The In-rich region, with up to 20% In content, is located at the topmost part of the QW in correspondence to the m-plane/semipolar plane junction region.

## 2.3 Optical properties

### 2.3.1 Photoluminescence spectroscopy

The optical properties of as-grown nanowire arrays have been probed by photoluminescence (PL). The PL characterization has been performed on nanowire ensembles using a frequency-doubled cw Ar<sup>2+</sup> ion laser ( $\lambda = 244$  nm). The laser was focused on the nanowire array into a spot of  $\sim 5$   $\mu\text{m}$  diameter by means of a 20X UV microscope objective with 0.4 numerical aperture. PL spectra were measured using a HR460 spectrometer with a 600 grooves/mm grating and a CCD camera. The PL spectrum at 77 K of the nanowire ensemble presents three distinct peaks as shown in Figure 2.2(a). The first one is attributed to the GaN near band edge (NBE) emission peaked at 3.467 eV with a full width at half-maximum (FWHM) of 60 meV. The two subbandgap peaks at 2.932 eV (FWHM = 208 meV) referred to as the “blue peak” and at 2.608 eV (FWHM = 95 meV) referred to as the “green peak” are attributed to the emission of the InGaN QW. The existence of two distinct peaks indicates the presence of regions with different In concentration.

### 2.3.2 Cathodoluminescence spectroscopy

The CL spectroscopy was used to probe the emission at different penetration depths and to assess the wire-to-wire fluctuations. The CL experiments have been performed by G. Jacopin at EPFL in an SEM microscope JEOL 7001F. The probe current was set to  $\sim 0.5$  nA. The CL spectra were recorded with a Jobin Yvon Spectrometer HR320 coupled with a CCD camera. Figure 2.2(b) shows the CL spectra acquired over a large region, shown in Figure 2c at  $T = 7$  K. GaN NBE luminescence is peaked at 3.49 eV (full width at half maximum (FWHM) = 62 meV). Similar to the PL, the InGaN cathodoluminescence is composed of two peaks at 2.978 (FWHM = 163 meV) and 2.624 (FWHM = 80 meV). Accounting for the Varshni shift with temperature, the peak energies are in good agreement with the PL observations. The acceleration voltage was varied from 5 kV to 15 kV to increase the excitation depth. For excitation with 5 kV acceleration voltages the two peaks have similar intensities, whereas at 15 kV acceleration voltages the blue peak has a ten times higher intensity than the green

peak. This relative intensity variation with acceleration voltage shows that the green peak arises from a region close to the nanowire top, whereas the blue peak comes from a deeper region. Casino simulations<sup>18</sup> for a 2D GaN layer allow estimating the statistical distribution of the electron penetration depth. The depth for which the statistical distribution of the electron penetration is equal to its maximum value divided by Euler's number  $e$  is equal to 250 nm for 5 kV and 1.3  $\mu\text{m}$  for 15 kV. This depth gives an estimation of the limit depth above which the electron-hole generation can be neglected and provides an estimate of the regions generating CL signal for the corresponding acceleration voltage.

Figures 2.2(d) and (e) show CL maps of a region shown in Figure 2.2(c). The maps were collected fixing the detection wavelength at the blue (420 nm) and green (472 nm) peaks, respectively. It is seen that both peaks are present in each wire and are located at the circumference of the nanowires in correspondence to the InGaN QW. The CL maps show an excellent wire-to-wire compositional homogeneity. Indeed, the wire-to-wire fluctuation of the peak wavelength for the blue peak is only 4 nm. The dispersion is higher for the green peak (8 nm) and the maximal intensity fluctuates from wire to wire and between different sidewalls of the same wire.

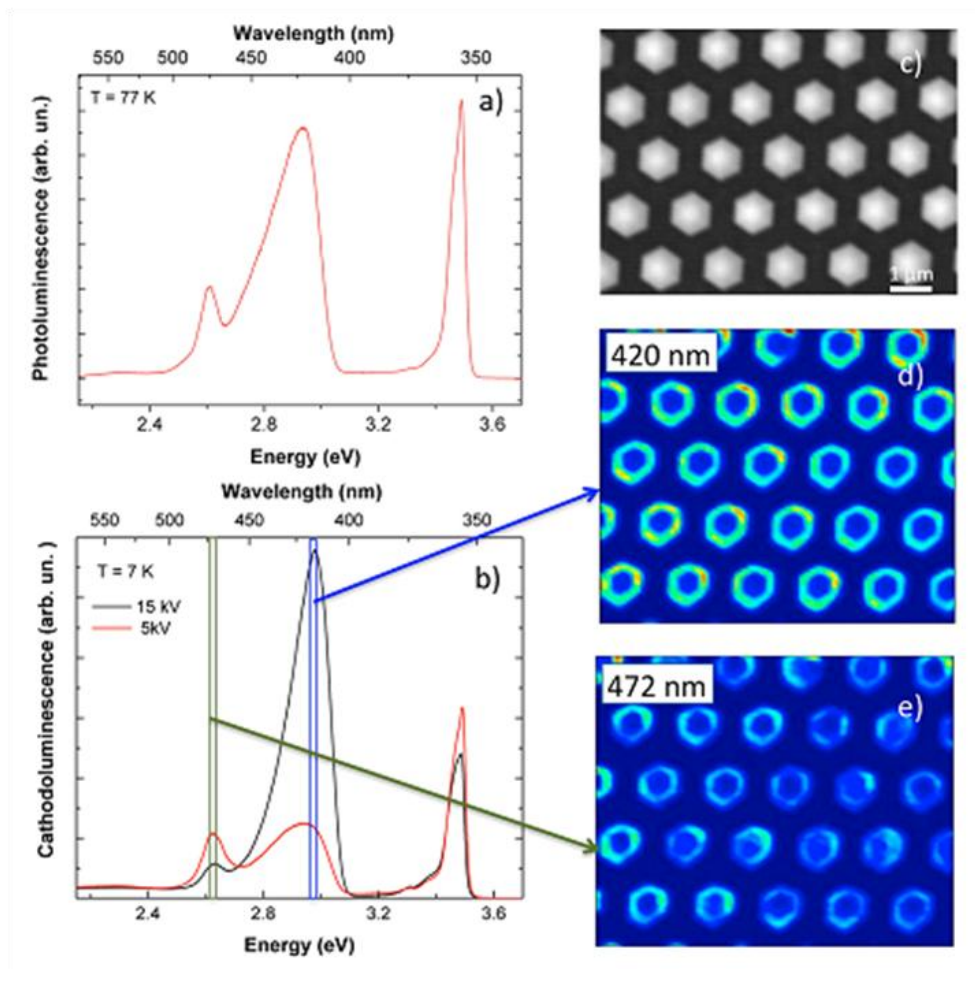


Figure 2.2. (a) PL spectrum of the nanowire array. (b) Low temperature CL spectrum collected at 5 kV and 15 kV acceleration voltage. (c) Top view SEM image of a region studied by CL. (d) and (e) CL maps recorded for a detection wavelength of 420 and 472 nm, respectively.

## 2.4 Device fabrication

To fabricate single nanowire LEDs, the wires were detached from their substrate by ultrasound cutting and dispersed on a Si/SiO<sub>2</sub> template with alignment marks. To provide a support for the contacts to these relatively thick nanowires, the wires were encapsulated in a hydrogen silsesquioxane polymer (HSQ) transformed into SiO<sub>x</sub> under thermal annealing. The excess of HSQ was wet-etched in diluted HF to partly uncover the nanowire lateral facets for contacting. The chosen slow etch rate of 50

nm/min is favorable to reveal foreign inclusions in the HSQ layer and, in particular, it allows to get a trench at the nanowire bottom facet, which gives a possibility to efficiently contact the n-doped core region of the nanowire. To reduce the contact resistance between the p-doped GaN shell and the graphene an ultrathin Ni layer ( $\sim 3$  nm) was deposited onto the sample surface. (The fabrication without Ni underlayer has also been tested; however, it results in a significant increase of the LED light-up voltage.) The graphene one monolayer sheet CVD-grown on copper foil was transferred using a wet transfer method as described in Refs [20][26]. The copper foil was etched using  $(\text{NH}_4)_2\text{S}_2\text{O}_8$  solution. The graphene sheet was structured by electron beam lithography with ma-N 2403 negative resist and  $\text{O}_2$  plasma etching. The Ni layer was then etched in a  $\text{FeCl}_3$  saturated aqueous solution. The graphene sheet with Ni underlayer covers about 60–80% of the nanowire length. A second run of e-beam lithography with positive PMMA resist was performed to define Ti/Al/Ti/Au metal contact to the nanowire bottom facet and to the graphene sheet using a lift-off procedure. The metallization was deposited by ebeam evaporation on a rotating sample tilted by  $45^\circ$  to allow for a good coverage of the nanowire bottom facet and, thus, to maximize the surface of the contact to the n-doped core region. It should be noted that contrary to the fabrication method employed in ref [27], the n-contact also covers about 100 nm of the p-doped GaN shell. However, because of the Schottky barrier formed between Ti/Al/Ti/Au and p-doped GaN, the current flows predominantly into the core region. The processed device is shown in Figure 2.3. The graphene sheet is visible as a dark gray region.

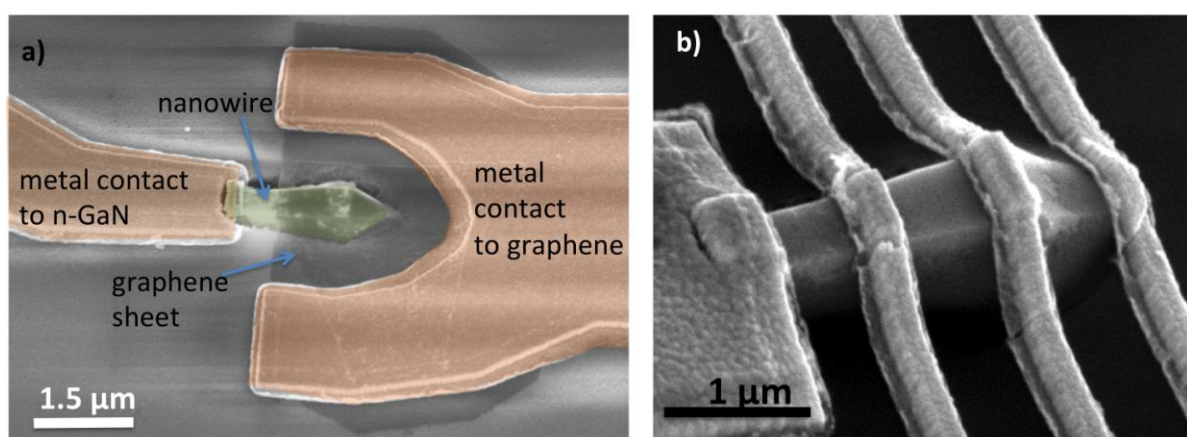


Figure 2.3 a) SEM image in artificial colors of the single wire graphene-contacted LED. The observation axis is tilted by  $30^\circ$  with respect to the top-view observation to enhance the contrast

produced by the graphene layer. b) SEM image of the reference metal-contacted LED.

Two reference samples containing either single nanowires with metal contacts or nanowire arrays have been fabricated. The single nanowire reference LEDs have been processed following the same procedure as described above, except that the graphene contact was replaced with Ni/Au 200 nm wide metal contacts at different places of the p-GaN shell. An SEM image of a single nanowire reference multicontact device is shown in Figure 2.3b). The reference array LEDs were fabricated in the form of square mesas containing more than 42000 parallel connected nanowires. The mesas were defined by optical lithography and inductively coupled plasma dry etching. The top p-type contact was obtained by a conformal deposition of 250 nm of indium tin oxide (ITO) layer onto the nanowires over a surface of  $290 \times 290 \mu\text{m}^2$ . It should be noted that no spin-on glass planarization has been performed, so that the final device has a rough surface. The 2D GaN layer on sapphire was used for bottom n-type contact. Ti/Al/Ti/Au metallization was deposited on the 2D GaN and on the top ITO surface leaving the central part of the mesa open for light extraction.

## **2.5 Device characterization**

### **2.5.1 Electrical characterization**

Figure 2.4 shows the room temperature current-voltage (I-V) characteristics of a single wire LED with a graphene contact. I-V data were recorded using a Keithley 2636 Source-Meter with 150 ms per point integration time. The device exhibits a rectifying behavior typical for an LED. No significant leakage under reverse bias has been observed: the inverse current is only  $3.5 \times 10^{-2} \mu\text{A}$  at -5 V. This low inverse current validates the fabrication procedure confirming that the small overlap of the bottom metal contact with the p-doped GaN shell is not detrimental for the device electrical performance. It also shows that the potential leakage that may arise from the semipolar planes having a narrow p-GaN layer is weak. The LED shows a current increase starting from 4 V direct bias and the electroluminescence appears under 0.16  $\mu\text{A}$  injection current at 6 V.

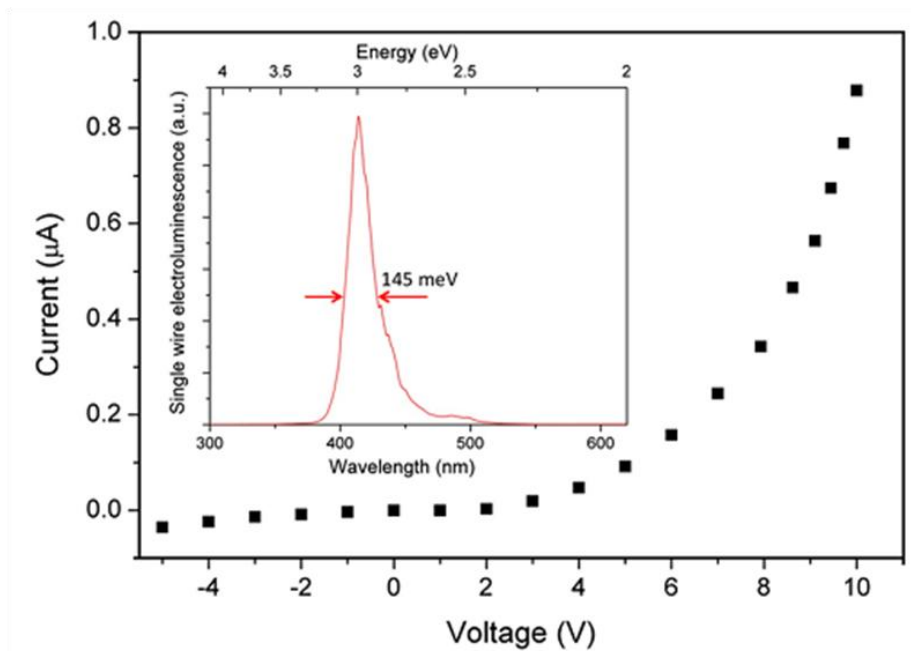


Figure 2.4 Room temperature I–V curve of a single wire LED with graphene p-contact. The inset shows the EL spectrum of single wire graphene LED operated at 10  $\mu\text{A}$  injection current.

## 2.5.2 Electron beam induced current characterization

The electrical behavior of single wire LEDs was further studied by charge collection microscopy. The electron beam induced current (EBIC) maps of the LEDs were measured at room temperature in a Hitachi SU8000 SEM by scanning the device surface with an electron beam at normal incidence. The metallic pads were contacted using micromanipulators connected to a Stanford Research System SR570 low-noise current preamplifier. The electron beam acceleration voltage and the extraction current were set to 20 kV and 10  $\mu\text{A}$ , respectively.

Current mapping allows assessment of the spatial distribution of electrical properties of the nanoscale device. This is achieved by a local generation of excess carriers in the vicinity of the built-in field region, which induces electron-hole pair separation and produces a current signal. Thanks to the good transparency for electrons of the graphene contact, the EBIC technique allows to probe the current generation in the radial p-n junction of the nanowire LEDs and in particular to assess the homogeneity

of carrier collection.

The SEM images and the EBIC maps of two single wire LEDs with a graphene p-contact and a metal p-contact are shown in Figure 2.5(a), (b) and (d), (e), respectively. The maps are collected under reverse bias of -3 V to facilitate the carrier extraction and to increase the generated current. The EBIC signal induced by the p-n junction appears as a bright contrast. The signal variation along the wire axis is shown in the EBIC profiles in Figures 2.5(c) and (f). For the graphene contacted LED, the EBIC signal is homogeneous over the cylindrical nanowire part (under -3 V bias the EBIC signal variation is less than 7%). This means that the carriers generated at any point of the core/ shell region covered by the graphene layer are efficiently collected by the contact. The EBIC signal only decreases in the conical nanowire extremity, which is ascribed to both the reduction of the active material volume and to the narrowing of the p-doped GaN shell on semipolar planes resulting in a shell electrical depletion in the top region. For the metal-contacted LED, the EBIC signal decreases starting from the p-contact toward the wire top (the signal varies by more than a factor of 2 in the cylindrical wire part). This signal decrease shows that many carriers generated far from the contact were not collected. Indeed, for a localized metal contact the generated holes should be transported in the p-doped GaN shell along the wire axis before reaching the contact. Because of its resistivity, the shell is not equipotential, and the transported carriers can be redistributed back into the junction instead of being collected. The carrier collection is, therefore, inhomogeneous for metal contacted LEDs contrary to the case of the graphene-contacted devices, for which the generated carriers are directly collected by the graphene layer without being transported in the p-doped shell.

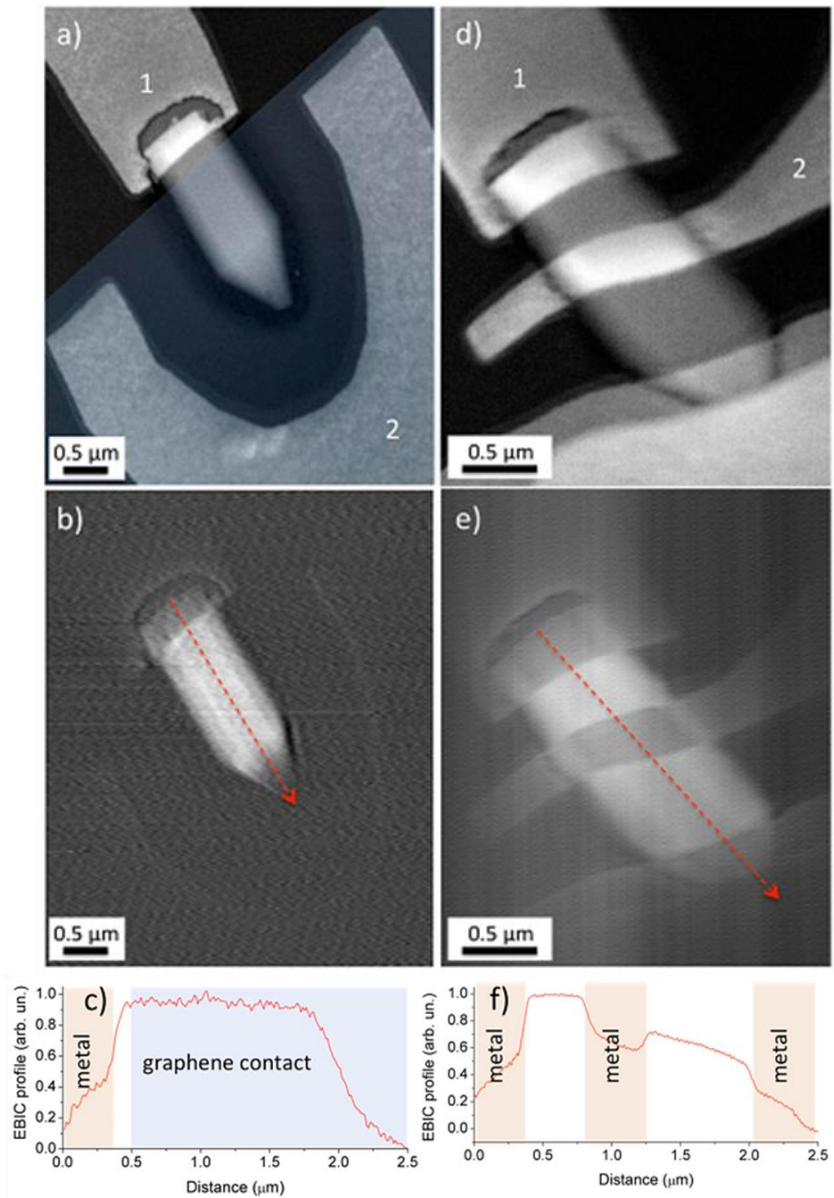


Figure 2.5 Top-view SEM image of (a) a graphene-contacted LED and (d) a metal-contacted LED. Blue colorization in (a) is used to visualize the region covered with the graphene electrode, which does not produce a sufficient contrast under top-view observation. (b) and (e) EBIC maps of the regions shown in (a) and (d). The bright contrast corresponds to the electrical signal generated in the p–n radial junction. The bias is applied between contacts “1” and “2”. (c) and (f) Normalized EBIC profiles along the dashed arrow in (b) and (e).

### 2.5.3 Electroluminescence characterizations

The electroluminescence (EL) spectra of single wire LEDs have been measured at room temperature for different injection current levels using the HR460 spectrometer and the CCD camera. The EL spectra for different injection currents of a single wire graphene LED in logarithmic scale are shown in Figure 6a, and an example of the EL spectrum in linear scale is shown in the inset to Figure 2.4. At low injection, the spectrum is peaked at 2.51 eV (494 nm) with a FWHM of 118 meV. For higher injection currents, a second peak appears at higher energy. The blue peak is growing fast with injection current while the green peak intensity increases slowly above 1  $\mu\text{A}$  injection. At high injection (10  $\mu\text{A}$ ) the EL spectrum is dominated by the blue peak at 2.99 eV (415 nm) with a FWHM of 145 meV. The green peak wavelength is almost constant for increasing injection current. For the blue peak a significant spectral blueshift of  $\sim 100$  meV accompanied by a shape change is observed.

A similar evolution of the EL spectral shape with injection current is observed in the reference array LED (Figure 2.6(b)). The EL at low injection presents a peak at low energy (2.51 eV, FWHM = 228 meV) and a second peak at high energy appears and progressively blue shifts with increasing injection current up to 2.92 eV (FWHM = 258 meV). The comparison with the single wire EL spectra shows a good agreement of the peak emission energies between single wire and array devices. The increased broadening of the EL peaks of the nanowire array LED compared to the single wire LED could be related to long range nanowire fluctuations as well as to some injection inhomogeneities.

Figures 2.6(c) and (d) present the EL spectra for the injection currents from 0.08  $\mu\text{A}$  to 15  $\mu\text{A}$  of a single nanowire reference LED having three metal contacts to the p-GaN shell. For the contact 1 located at the middle of the m-plane facet (panel c), the EL spectra exhibit similar spectral behavior with injection current as the graphene-contacted device: the green EL first appears at 2.54 eV (488 nm), and then a blue peak at 2.96 eV (419 nm) quickly becomes dominant. However, for the contact 2 located close to the junction between the m-plane and the semipolar plane (panel d) the behavior is different: the EL is peaked at 2.54 eV (488 nm) at low injection, and it progressively broadens and slightly blue shifts to 2.66 eV (465 nm) at high injection. No distinct blue peak is observed for contact 2 at high injection. Finally, no EL is observed for the contact 3 located at the nanowire tip, which is indeed expected due to the small thickness of the p-GaN shell in this region.

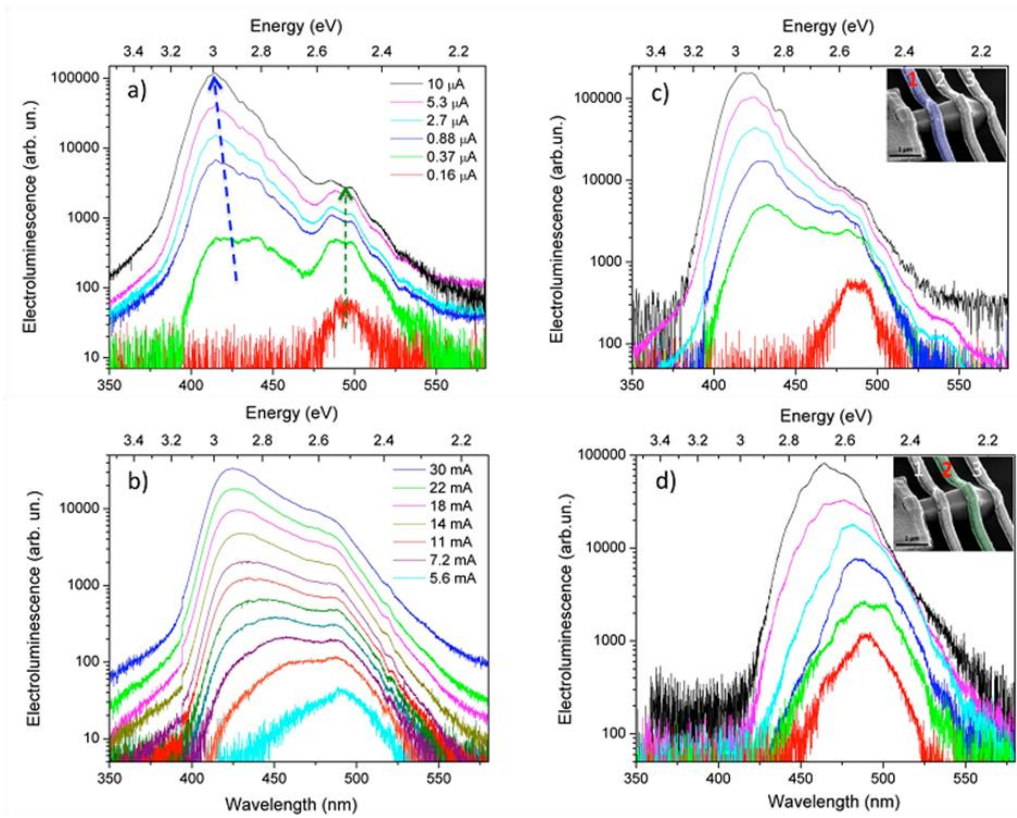


Figure 2.6. Room temperature EL spectra in logarithmic scale for increasing injection current (a) of a single wire LED with graphene contact; (b) of an array LED; (c) of a single wire LED with a metal contact at the middle of the lateral facet; (d) of a single wire LED with a metal contact at the m plane and semipolar plane junction. The inset to figure (c) and (d) shows the SEM image of the multicontact reference LED. The contact used for the hole injection is colored.

## 2.5.5 Cathodoluminescence mapping

To understand this complex spectral behavior and the origin of the two EL peaks, a high resolution CL mapping of single nanowires has been performed. Indeed, CL provides a possibility to spatially map the emission at a given wavelength and, thus, determine its origin. CL maps have been first recorded on single wire LEDs and on non-processed dispersed wires (not shown), indicating that the green peak originates from the nanowire top part, whereas the blue peak is extended on the entire m-plane. To

increase the spatial resolution and to precisely localize the two emissions, the nanowire array was cleaved along an axis perpendicular to the nanowire m-facets. Because of the large nanowire diameter, this procedure allows cleavage of some of the nanowires parallel to the growth axis without breaking them from their substrate. A nanowire cleaved approximately through the middle of two opposite m-plane facets has been carefully selected for the CL experiment. The CL mapping has been performed at  $T = 7$  K on the cross section of the cleaved sample containing the nanowire of interest. In this case, the electron beam excites directly the InGaN QW and a much better spatial resolution is obtained.

Figure 2.7(a) shows an SEM image of the nanowire array containing a cleaved nanowire as well as the low temperature CL maps of the cleaved wire for different detection wavelengths. A low acceleration voltage of 5 kV was employed to get a high spatial resolution. The color map superimposed with the SEM image presents the averaged wavelength of the InGaN emission. It is seen that the average emission wavelength strongly increases in the upper part of the QW. This is further confirmed by the CL maps at different detection wavelengths. The CL emission at 410 nm is localized in the lower part of the QW (cf. Figure 2.7(b)). The signal at 420–430 nm is observed over the entire length of the nanowire m-plane sidewalls. At longer wavelength (440–460 nm) the emission progressively shifts toward the top of the m-planes and at 470–480 nm the emission arises exclusively from a small region of the QW located at the junction between the m-planes and the semipolar planes.

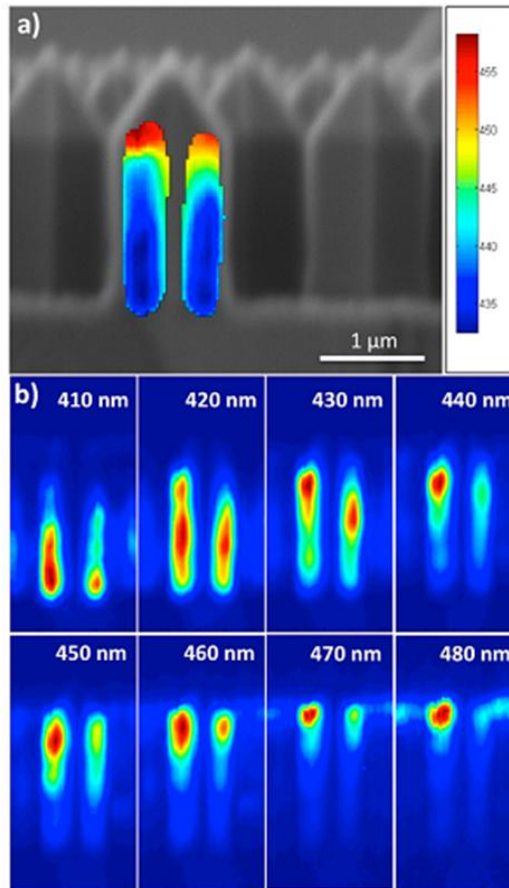


Figure 2.7. (a) Cross-sectional SEM image of the nanowire array containing a cleaved nanowire. The superimposed map shows the average CL wavelength. (b) CL maps collected at 7 K with 5 kV acceleration voltages for fixed detection wavelength from 410 nm to 480 nm.

The cross-sectional CL maps demonstrate the presence of a compositional gradient in the InGa<sub>N</sub> QW. According to the maps, the In content is about 10% (15%) in the lower (medium) part of the m-planes and it increases toward the top of the m-planes. The observation of a localized emission with a lower energy indicates the presence of an In-rich region at the m-plane and semipolar plane junction. According to the CL wavelength<sup>17</sup>, the In content in this region is about 18–20%.

The comparison between the cross-sectional CL maps and the top view CL measurements provides a full picture of the emission localization in the nanowires. The emission peak observed at 420 nm in the top view CL spectrum of Figure 2.7 arises from the QW on the m-planes, while the peak at 472 nm comes from the In-rich region at the m-plane and semipolar plane junction. This assignment is

consistent with the observed dependence of the top-view CL spectra on the acceleration voltage.

The CL maps also elucidate the origin of the green and the blue peaks observed in the EL spectra. The EL green peak well matches the wavelength of the CL signal localized at the m plane and semipolar plane junction (region 1 in the schematic of a graphene-contacted LED of Figure 2.8a). At low injection current, only this In-rich region produces an EL signal. The EL of this region exhibits only a weak spectral blue shift with increasing current, which can be due to the band filling effects. The blue peak of the EL can be ascribed to the emission extended along the m-plane QW.

## 2.6 Electrical model of the nanowire LEDs

The behavior of the EL spectra as a function of the injected current can be understood by analyzing the current injection in the nanowire LEDs. Here, we show that a simple and intuitive electrical model of the nanowire LED is sufficient to explain our experimental observations. The model has been developed by P. Lavenus during his PhD work. The nanowire is discretized along its axis into small segments constituting elementary cells that are represented by an equivalent electrical circuit as illustrated in Figure 2.8(b). The distribution of the electrical current in the obtained electrical network is then calculated. The network is composed of two circuits representing the nanowire portion covered with the graphene electrode (referred to as “upper circuit”, cf. Figure 2.8(b)) and the portion between the graphene electrode and the metallic bottom contact (referred to as “lower circuit”, cf. Figure 2.8(b)). In the upper circuit, an elementary cell consists of two resistances  $R_{core}$  and  $R_{series}^{up}$  that connect a diode.  $R_{core}$  and  $R_{series}^{up}$ , respectively, account for the resistance of the n-GaN core along the wire axis and of the p-GaN shell perpendicular to the wire axis (the contact resistance is also incorporated into  $R_{series}^{up}$ ). In the nanowire part covered with the graphene electrode, the shell resistance along the wire axis has no impact on the transport since the graphene contact is considered to be equipotential. In the lower circuit the elementary cell is different. Here, the current propagates in the shell mainly parallel to the wire axis; therefore,  $R_{shell}$  is introduced to take into account the parallel shell resistance. The shell resistance is assumed to be uniform along the wire axis, that is, any possible p-doping fluctuations are neglected. Close to the graphene contact, the current lines in the outer shell continuously change their orientation from a direction purely perpendicular to the wire axis to a

direction parallel to the wire axis; to take this phenomenon into account, series resistance  $R_{series}^{low}$  that vanishes as the distance from the graphene contact increases are introduced. The diode in elementary cells of both circuits models the radial p-n junction of the corresponding segment and is described by its saturation current  $I_{sat}$  and its ideality factor  $\eta$ .

The nanowire parameters have been estimated by fitting the direct branch of the experimental I-V curve. The fitting is performed by calculating the current–voltage dependence in the electrical network schematized in Figure 2.8(b) composed of 100 elementary cells. The best fit is shown in Figure 2.8(c) and the corresponding parameters are listed in Table 1.

$R_{core}$ ( $\Omega$ )	$R_{shell}$ ( $\Omega$ )	$R_{series}^{up}$ ( $\Omega$ )	$R_{series}^{low}$ ( $\Omega$ )	$I_{sat}$ (A)	$I_{sat,In-rich region}$ ( $\Omega$ )	$\eta$
$8.16 \times 10^3$	$7.71 \times 10^5$	$9.08 \times 10^6$	$6.2 \times 10^5$	$4.27 \times 10^{-16}$	$1.03 \times 10^{-10}$	23

Table 1. Parameters extracted from the I–V curve fit that are used for electrical simulations

To model the presence of an In-rich region at the topmost part of the QW (region 1), the saturation current has been modified in the last elementary cell. (The presence of the In gradient in the QW is neglected for simplicity, so that all other elementary circuits have the same parameters.)

The local increase of In concentration in the QW results in an increase of the saturation current of the corresponding elementary diode. Indeed, assuming that the radiative recombination is the dominant recombination mechanism and that the Shockley assumption is verified (i.e., the quasi-Fermi levels are constant across the active region), the current density flowing inside the LED can be calculated as

$$J = \int_{QW} dz B (n(z)p(z) - n_0 p_0) \quad (2.1)$$

$$= \left( \exp \frac{qU}{k_B T} - 1 \right) \int_{QW} dz (B \times n_i^2) \quad (2.2)$$

where the integration is carried out on the width  $w$  of the QW,  $q$  stands for the elementary charge,  $B$  is the radiative recombination coefficient,  $n(z)$  and  $n_0$  ( $p(z)$  and  $p_0$ ) are the electron (hole) concentrations in the QW under the applied bias  $U$  and under equilibrium, respectively.  $n_i$  stands for the intrinsic carrier concentration in the InGaN; it is given by the expression  $n_i^2 = N_c N_v \exp(-E_g/k_B T)$  with  $N_c$  and

$N_v$  representing the effective density of states at a temperature  $T$ .  $E_g$  is the InGaN band gap and  $k_B$  is the Boltzmann constant. Therefore, the saturation current density is given by

$$J_{sat} = \int_{QW} dz (B \times n_i^2) = wBN_cN_v \exp\left(-\frac{E_g}{k_B T}\right) \quad (2.3)$$

The values of  $B$ ,  $N_c$ , and  $N_v$  only weakly depend on the indium content in the InGaN alloy for the present composition range. However, because of the large bandgap difference between InN and GaN,  $J_{sat}$  strongly depends on the In content via the exponential term. The bandgap difference between the In-rich region and the middle part of the QW is estimated from the CL spectra to be in the range of  $\Delta E \sim 0.2-0.4$  eV. Therefore, the saturation current in the last diode  $I_{sat}$ , In-rich region representing the In-rich region 1 should be increased by a factor  $\sim 10^3-10^8$  with respect to the saturation current  $I_{sat}$  of the middle QW region.

Figure 2.8(d) presents a 3D plot of the calculated normalized current distribution inside elementary diodes of the single wire LED as a function of the position along the nanowire axis and of the applied biases. It is observed that at low bias the injection takes place predominantly in region 1 corresponding to the highest saturation current (marked with a green arrow on Figure 2.8(d)). When the applied bias is increased, a progressive increase of the current in the other regions of the wire (i.e. regions 2-4) is observed. In particular, the bias increase leads to a preferential injection into diodes located at the end of the graphene contact (region 3, marked with a blue arrow), while the injection in the In-rich region 1 progressively reduces.

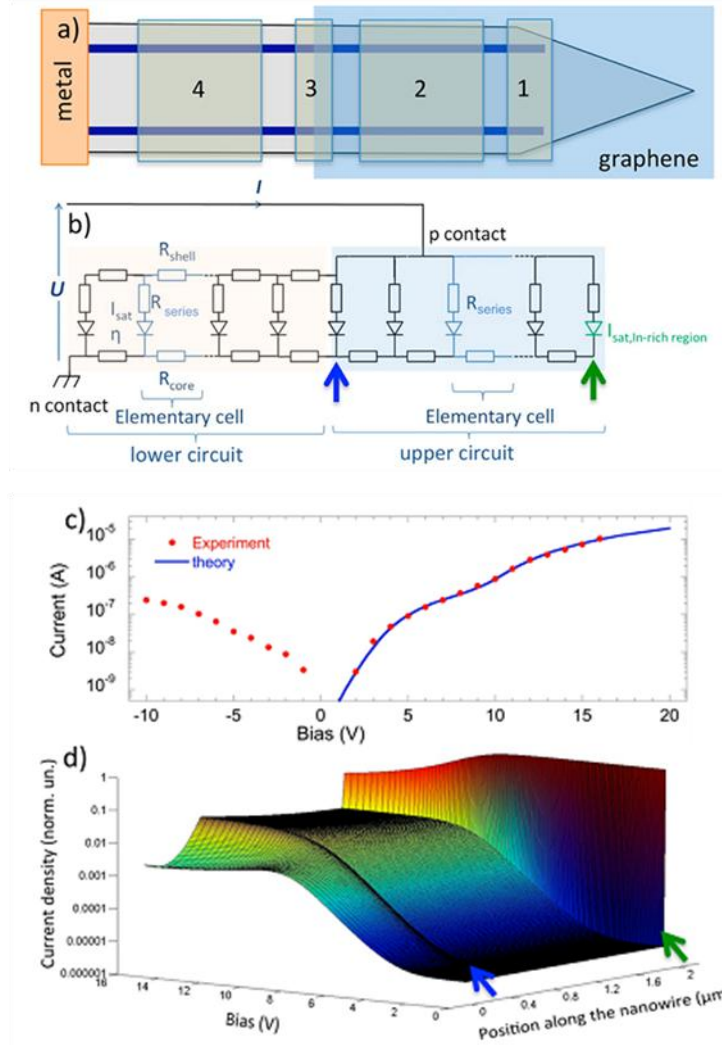


Figure 2.8 (a) Schematic representation of a nanowire LED (not to scale). Labels mark the In-rich region (1), the middle part of the wire (2), the end of the graphene electrode (3), and the bottom part of the wire below the graphene electrode (4). (b) Electrical network representing the LED. (c) LED I–V curve in log scale (asterix) and the fitting curve calculated for the electrical network of panel b. (d) Normalized current distribution in a logarithmic scale as a function of the applied bias and of the position along the nanowire. Green (blue) arrow indicates the position of the In-rich region (the end of the graphene electrode).

This behavior can be easily understood taking into account nonzero shell and core resistances. At low injection, the potential drop across the shell and the core is negligible and the injected current distribution is governed by the elementary diode parameters (i.e., the saturation current). However, as

the current level increases, the series resistance makes unfavorable the inhomogeneous injection concentrated in the In-rich region and leads to a progressive increase of the injection into regions 2-4. Moreover, at high injection, the core is no longer equipotential and the potential drop in the core increases with increasing injection. This means that the potential drop across the elementary radial junctions of the upper circuit is lower in the top nanowire part than in the lower part, which favors the injection in region 3. However, in the lower circuit, the shell resistance comes into play. Because of the lower doping and smaller thickness the shell resistance is significantly higher than the core resistance, so that the carrier transport in the shell induces a large potential drop. Therefore, the carrier injection in region 4 outside the graphene electrode is unfavorable and the simulation predicts current concentration in the vicinity of the lower end of the graphene electrode for high injection conditions. It is interesting to note that the transition from preferential injection in region 1 to region 3 manifests in the I-V curve as a slope change observed for biases between 6 and 11 V.

The reference single wire LEDs with a narrow metal p-contact were modeled following the same approach as for single wire LEDs with an extended graphene p-contact. The upper circuit of the equivalent electrical network of Figure 2.8(b) has been modified to account for a narrow metal contact located either in region 3 or in region 1. The equivalent electrical circuits for two different cases of a metal contact placed at the middle of the m-plane and a metal contact placed at the In-rich region are shown in Figures 2.9(a) and (c). The corresponding 3D plots of the current as a function of applied bias and of the position along the nanowire axis are shown in Figures 2.9(b) and (d). The calculations were performed using the electrical parameters of Table 1 of the paper. For the contact placed in the middle of the m-plane (Figure 2.9(b)) the model predicts a preferential injection into the In-rich region at low bias. At high injection the current becomes concentrated under p-contact and the injection into this region quickly overcomes the injection into In-rich region. This transition from a preferential injection into In rich region 1 to the injection into regions 2 and 3 is similar to the case of an extended graphene contact. For the contact placed at the junction of the m-plane and of the semipolar plane corresponding to the In-rich region (Figure 2.9(d)), the current remains concentrated in the diode with the highest saturation current at any bias. No EL color change is expected in this case.

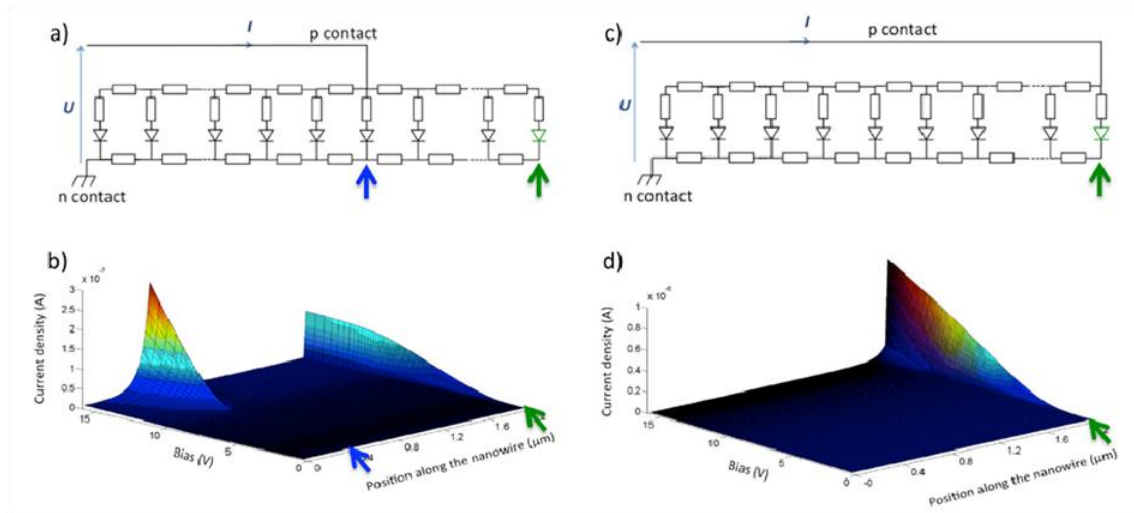


Fig 2.9. (a) Electrical network representing an LED with a metal contact at the middle of the m-plane. (b) Current distribution as a function of the applied bias and of the position along the nanowire for the electrical circuit shown in panel (a). Green and blue arrows indicate the positions of the In-rich region and of the metal p-contact, respectively. (c) Electrical network representing an LED with a metal contact at the m-plane/semipolar plane junction. (d) Current distribution as a function of the applied bias and of the position along the nanowire for the electrical circuit shown in panel (c). Green arrow indicates the position of the In-rich region.

Despite its simplicity, the proposed electrical model explains well the observed experimental trends both for an LED with an extended graphene contact and for an LED with localized metal contacts. At low injection the EL spectra present only the green peak originating from the region characterized with a high saturation current. At high injection, the emission is predicted to concentrate in the region with the lowest serial resistance. This region depends on the contact layout. For extended graphene contact or a localized metal contact on the m-plane, it results in a blue emission, whereas for a localized metal contact located at the In-rich region, a green emission is predicted.

It should, however, be noted that the correct description of the EL should take into account not only the injection current profile described by the present model but also the carrier diffusion in the QW to determine the recombination position. Because of the compositional gradient, the carrier diffusion

from the lower nanowire part to the upper part is expected to be enhanced because of the potential gradient in the QW. Therefore, even under high injection conditions, the carriers diffuse from region 3 toward the nanowire top thus contributing to an additional low-energy broadening of the EL blue peak as observed in Figure 2.6.

## **2.7 Conclusion**

In this chapter, I have presented the fabrication and electro-optical characterization of single nanowire InGaN/GaN LEDs with a transparent graphene contact for hole injection. I have successfully investigated the EL of a single nanowire LED and I have analyzed the impact of the contact layout on the emission properties. In particular, I have shown that the position of the contact determines the spectral evolution with injection current. Namely, for an extended contact and a contact localized on the m-plane, a transition from the green to blue emission is observed whereas for a localized contact on the m-plane/semipolar plane junction the emission remains green. The dependence of the emission color on the contact geometry will be used in the next chapter to control the EL spectra of nanowire array LEDs.

## References

- [1] Li, Shunfeng, and Andreas Waag. "GaN based nanorods for solid state lighting." *Journal of Applied Physics* 111.7 (2012): 071101.
- [2] Kang, M. S.; Lee, C. H.; Park, J. B.; Yoo, H.; Yi, G. C., Gallium nitride nanostructures for lightemitting diode applications, *Nano Energy* 2012, 1 (3), 391–400.
- [3] Hiroto Sekiguchi, Katsumi Kishino, and Akihiko Kikuchi, Emission color control from blue to red with nanocolumn diameter of InGaN/GaN nanocolumn arrays grown on same substrate, *Appl. Phys. Lett.* 96, 231104 (2010);
- [4] K. Kishino, A. Yanagihara, K. Ikeda and K. Yamano, Monolithic integration of four-colour InGaN based nanocolumn LEDs, *El. Lett.* 51 (11), 852–854 (2015).
- [5] Chung, K.; Beak, H.; Tchoe, Y.; Oh, H.; Yoo, H.; Kim, M.; Yi, G.-C., Growth and characterizations of GaN micro-rods on graphene films for flexible light emitting diodes, *Apl Materials* 2014, 2, (9), 092512.
- [6] Xing Dai, Agnes Messanvi, Hezhi Zhang, Christophe Durand, Joël Eymery, Catherine Bougerol, François H Julien, Maria Tchernycheva « Flexible Light-Emitting Diodes Based on Vertical Nitride Nanowires » *Nano letters* 15 (10), 6958-6964 (2015).
- [7] Brubaker, M. D.; Blanchard, P. T.; Schlager, J. B.; Sanders, A. W.; Roshko, A.; Du, S. M.; Gray, J. M.; Bright, V. M.; Sanford, N. A.; Bertness, K. A., On-Chip Optical Interconnects Made with Gallium Nitride Nanowires, *Nano Lett.* 2013, 13, 374–377.
- [8] Tchernycheva M, Lavenus P, Zhang H, Babichev A V, Jacopin G, Shahmohammadi M, Julien F H, Ciechonski R, Vescovi G, Kryliouk O, InGaN/GaN Core/Shell Single Nanowire Light Emitting Diodes with Graphene-Based P-Contact, *Nano Letters* 14, 2456 (2014).
- [9] Gößler C, Bierbrauer C, Moser R, Kunzer M, Holc K, Pletschen W, Köhler K, Wagner J, Schwaerzle M, Ruther P, Paul O, Neef J, Keppeler D, Hoch G, Moser T and Schwarz U T, GaN-based micro-LED arrays on flexible substrates for optical cochlear implants *J. Phys. D: Appl. Phys.* 47 (2014) 205401
- [10] Massoubre D, Xie E, Guilhabert B, Herrnsdorf J, Gu E, Watson I M and Dawson M D 2014 Microstructured light emission from planar InGaN light-emitting diodes *Semicond Sci Tech* 29 15005

- [11]Hwa-Mok Kim, Yong-Hoon Cho, Hosang Lee, Suk Il Kim, Sung Ryong Ryu, Deuk Young Kim, Tae Won Kang, and Kwan Soo Chung, High-Brightness Light Emitting Diodes Using Dislocation-Free Indium Gallium Nitride/Gallium Nitride Multiquantum-Well Nanorod Arrays, *Nano Letters*, 2004, 4 (6), pp 1059–1062
- [12]Akihiko Kikuchi, Mizue Kawai, Makoto Tada and Katsumi Kishino, InGaN/GaN Multiple Quantum Disk Nanocolumn Light-Emitting Diodes Grown on (111) Si Substrate, *Japanese Journal of Applied Physics*, Volume 43, Part 2, Number 12A (2004).
- [13]F. Qian, S. Gradečak, Y. Li, Wen C-Y, Lieber C M, Core/multishell nanowire heterostructures as multicolor, high-efficiency light-emitting diodes, *Nano Lett.* 5 (2005) 2287.
- [14]R. Koester, Jun-Seok Hwang, Damien Salomon, Xiaojun Chen, Catherine Bougerol, Jean-Paul Barnes, Daniel Le Si Dang, Lorenzo Rigutti, Andres de Luna Bugallo, Gwéñol é Jacopin, Maria Tchernycheva, Christophe Durand, and Joël Eymery, M-Plane Core–Shell InGaN/GaN Multiple-Quantum-Wells on GaN Wires for Electroluminescent Devices, *Nano Lett.*, 2011, 11 (11), pp 4839–4845
- [15]G. Jacopin, A. De Luna Bugallo, P. Lavenus, L. Rigutti, F. H. Julien, L. F. Zagonel, M. Kociak, C. Durand, D. Salomon, X. J. Chen, J. Eymery, and M. Tchernycheva, Single-Wire Light-Emitting Diodes Based on GaN Wires Containing Both Polar and Nonpolar InGaN/GaN Quantum Wells, *Appl. Phys. Express*, 5 (2012) 014101.
- [16]Li, S.; Wang, X.; Fundling, S.; Erenburg, M.; Ledig, J.; Wei, J.; Wehmann, H. H.; Waag, A.; Bergbauer, W.; Mandl, M.; Strassburg, M.; Trampert, A.; Jahn, U.; Riechert, H.; Jönen, H.; Hangleiter, A. *Appl. Phys. Lett.* 2012, 101 (3), 032103–032103
- [17] Chen, H. S.; Yao, Y. F.; Liao, C. H.; Tu, C. G.; Su, C. Y.; Chang, W. M.; Kiang, Y. W.; Yang, C. C., Light-emitting device with regularly patterned growth of an InGaN/GaN quantum-well nanorod light-emitting diode array, *Opt. Lett.* 2013, 38 (17), 3370–3373.
- [18]Chang J R, Chang S P, Li Y J, Cheng Y J, Sou K P, Huang J K, Kuo H C and Chang C Y 2012 Fabrication and luminescent properties of core-shell InGaN/GaN multiple quantum wells on GaN nanopillars *Appl Phys Lett* 100 261103
- [19] Hong Y-J, Lee C-H, Yoon A, Kim M, Seong Han-K, Chung H-J, Sone C, Park Y-J, Yi G-C, 2011 Visible-Color-Tunable Light-Emitting Diodes. *Adv. Mater.* 23 3284

- [20] Babichev, A. V.; Zhang, H.; Lavenus, P.; Julien, F. H.; Egorov, A. Yu.; Lin, Y. T.; Tu, L. W.; Tchernycheva, M. *Appl. Phys. Lett.* 2013, 103, 201103.
- [21] Fu, X. W.; Liao, Z. M.; Zhou, Y. B.; Wu, H. C.; Bie, Y. Q.; Xu, J.; Yu, D. P. *Appl. Phys. Lett.* 2012, 100 (22), 223114–223114.
- [22] Li, Z.; Kang, J.; Zhang, Y.; Liu, Z.; Wang, L.; Lee, X.; Li, X.; Yi, H.; Zhu, H.; Wang, G. J. *Appl. Phys.* 2013, 113, 234302.
- [23] Jeon, D. W.; Choi, W. M.; Shin, H. J.; Yoon, S. M.; Choi, J. Y.; Jang, L. W.; Lee, I. H. *J. Mater. Chem.* 2011, 21, 17688.
- [24] Lee, J. M.; Choung, J. W.; Yi, J.; Lee, D. H.; Samal, M.; Yi, D. K.; Lee, C. H.; Yi, G. H.; Paik, U.; Rogers, J. A.; Park, W. I. *Nano Lett.* 2010, 10 (8), 2783–2788.
- [25] Ye, Y.; Gan, L.; Dai, L.; Meng, H.; Wei, F.; Dai, Y.; Shi, Z.; Yu, B.; Quob, X.; Qin G, G. *J. Mater. Chem.* 2011, 21 (32), 11760–11763.
- [26] Zhang, H.; Babichev, A. V.; Jacopin, G.; Lavenus, P.; Julien, F. H.; Egorov, A. Yu.; Zhang, J.; Pauporte, T.; Tchernycheva, M. *J. Appl. Phys.* 2013, 114, 234505.
- [27] Qian, F.; Li, Y.; Gradecak, S.; Wang, D.; Barrelet, C. J.; Lieber, C. M. *Nano Lett.* 2004, 4 (10), 1975–1979.

## Chapter3: Vertical single and array NWs LEDs

### Table of contents

---

3.1 Nanowires growth method .....	56
3.2 Optical properties .....	57
3.2.1 Micro-photoluminescence spectroscopy.....	57
3.2.2 Cathodoluminescence spectroscopy .....	58
3.3 Single nanowire LEDs.....	59
3.3.1 Fabrication of single nanowire LEDs .....	59
3.3.2 Electrical characterization of single nanowire LEDs.....	61
3.3.3 Electroluminescence of single nanowire LEDs .....	62
3.4 Array LED color control by a post-growth treatment.....	65
3.4.1 Processing of array LEDs with different contacting schemes .....	65
3.4.2 Electrical characterization of array LEDs with different contacting schemes .....	67
3.4.3 EBIC characteristics of array LEDs with different contacting schemes .....	68
3.4.4 Electroluminescence of array LEDs with different contacting schemes .....	69
3.5 EBIC signal transient at the core/under layer interface of n-GaN.....	72
3.6 Correlation between EBIC maps and electroluminescence maps .....	78
3.7 Front n-contact LED.....	80
3.8 Conclusions .....	87

---

The NW LED optimization requires the assessment of wire-to-wire dispersion and intra-wire compositional variations. These issues have been addressed in the previous chapter by studying the emission of individual wires using single NWs detached from their substrate and electrically contacted in planar geometry. I have shown that in NWs with intrinsic compositional inhomogeneities the EL depends on the contact layout. Therefore, in order to be representative, single wire experiments should

be performed using the same contacting scheme as the one used for the array device. In the first part of this chapter, I describe the fabrication and characterization of single wire LEDs made out of a vertical NW array with the same contacting scheme (i.e. an electron injection through the substrate and holes injection through a conformal ITO contact) as used for macroscopic LEDs. I demonstrate that the emission of single wire LEDs exhibits the same broadening as the array LED emission, which proves a good inter-wire homogeneity. As in the LED studied in the previous chapter, the EL spectra present two peaks corresponding to the m-plane InGaN QW and to an In-rich region at the m-plane-semipolar plane junction. These fabricated ultra-compact bright light sources can find applications as localized optical stimuli for biological studies or can be integrated into a matrix of micro-pixels.

The above-mentioned dependence of the EL on the contact morphology opens the way to control the LED emission color at the device processing stage. Indeed, if the compositional variation cannot be avoided at the growth stage, the electrical injection in the unwanted regions can be inhibited by a dedicated post-growth treatment. In the second part, I show that for NW LEDs coming from the same growth run the EL color can be controlled by the contacting procedure. In particular, the pure blue emission without a spectral shift with injected current is achieved with NWs initially presenting regions of different InGaN composition. This is realized by locally reducing the conductivity of the p-doped GaN shell using fluorine plasma treatment to inhibit the electrical injection in the In-rich region of the QW.

In the last part of this chapter, I analyze the injection inhomogeneity induced by charge traps at the interface between the nanowire n-GaN core and the radially grown n-GaN layer. The EBIC microscopy indicates the presence of two kinds of signals: the signal having a circular shape localized close to the interface between the NW core and the NW n-GaN underlayer, and the signal having a hexagonal shape coming from the NW radial p-n junction active region. The electrical activity at the core/underlayer interface in certain nanowires is attributed to charged traps. This phenomenon impedes the homogeneous injection and reduces the performance of the nanowire LED array, resulting in a low number of working nanowires (19%). In order to avoid injection through a potential barrier at the core/underlayer interface, I developed a top down contacting scheme with electrons injected directly into n-GaN underlayer, which is called “front contacting” process. The “front contacting” LEDs present an increased yield of the active NWs in the EL maps (65%). The high yield for “front

contacting” LEDs proves that the front electron injection allows to reduce the negative impact of the potential barrier at the core/underlayer interface.

### 3.1 Nanowires growth method

Organized InGaN/GaN core-shell nanowires were grown by MOVPE on n-doped GaN/sapphire substrates covered with an SiN mask with submicrometer openings. The nanowire structure is schematized in the colored scanning electron microscope (SEM) image of a cleaved wire shown in Figure 3.1a). First, an n - doped GaN core with a doping concentration of about  $2 \times 10^{18} \text{ cm}^{-3}$  was formed and laterally overgrown with an n-doped underlayer with a doping concentration of about  $2 \times 10^{19} \text{ cm}^{-3}$ . Then the active region consisting of one InGaN quantum well and an AlGaN electron blocking layer was deposited. Finally, a 150 nm thick p-doped GaN shell was deposited with a Mg concentration of  $\sim 5 \times 10^{19} \text{ cm}^{-3}$ . Figure 1b) presents an SEM image of an as-grown nanowire array. The nanowires exhibit an excellent uniformity with a density of  $4.4 \times 10^7 \text{ nanowire} / \text{cm}^2$ . The nanowire height is  $\sim 2 \mu\text{m}$  and the diameter is  $1.5 \mu\text{m}$ . The nanowires consist of an almost cylindrical base part of about  $1 \mu\text{m}$  and of a pyramidal top part as seen in Figures 3.1a) and 3.1b).

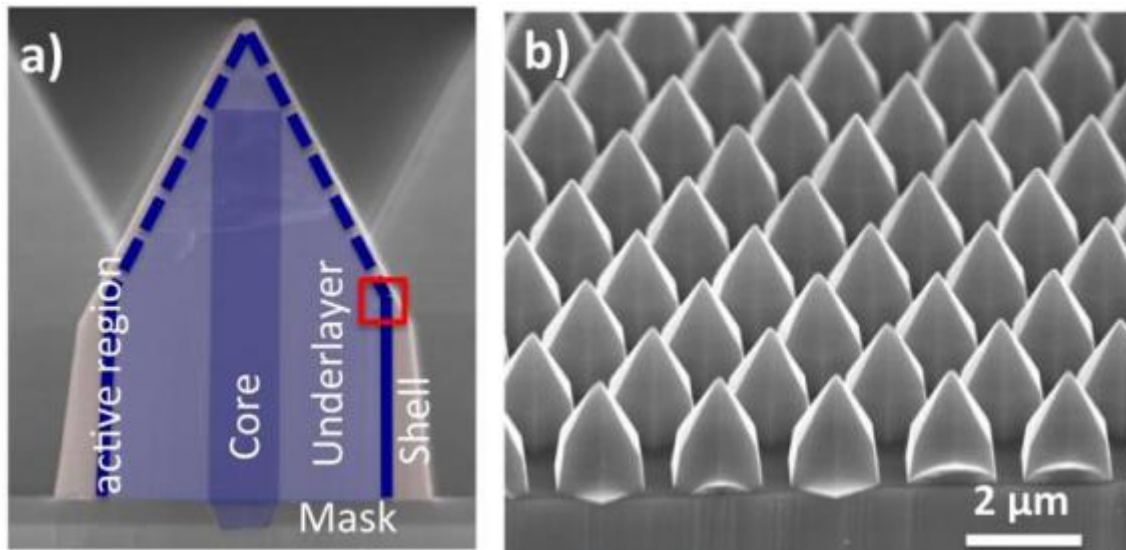


Fig. 3.1 a) SEM image of a cleaved nanowire in artificial colors showing the nanowire internal structure. b) 45 °tilted SEM image of a cleaved nanowire array.

## 3.2 Optical properties

### 3.2.1 Micro-photoluminescence spectroscopy

The optical properties of single nanowires were investigated by micro-photoluminescence ( $\mu$ PL) spectroscopy. In order to avoid excitation of multiple nanowires, the nanowires were cut from their substrate by an ultrasonic bath and dispersed with a low density on a Si substrate. The  $\mu$ PL characterization was carried out at 4 K by exciting single nanowires at 244 nm wavelength by a continuous wave frequency-doubled  $\text{Ar}^{++}$  ion laser. Figure 3.2 shows a typical  $\mu$ PL spectrum of a single nanowire. The spectrum presents four distinct peaks. The high-energy peak centered at 3.46 eV with a FWHM of 128 meV originates from the GaN NBE emission. The second peak at around 3.15 eV (FWHM  $\sim$  206 meV) is close in energy to the donor-acceptor pair (DAP) band and is attributed to the DAP emission of the Mg doped GaN shell. The two subbandgap peaks at lower energy (at 2.78 eV and 2.47 eV, respectively) are attributed to the emission of the InGaN quantum well. In agreement with the above-described EDX compositional analyses, the emission at 2.78 eV (in the following called “blue peak”) with a FWHM of 203 meV arises from the InGaN quantum well on the m-plane. The emission at 2.47 eV (in the following called “green peak”) with a FWHM of 83 meV is attributed to the In-rich region at the m-plane/ semipolar plane junction shown in Figure 3.1 d).

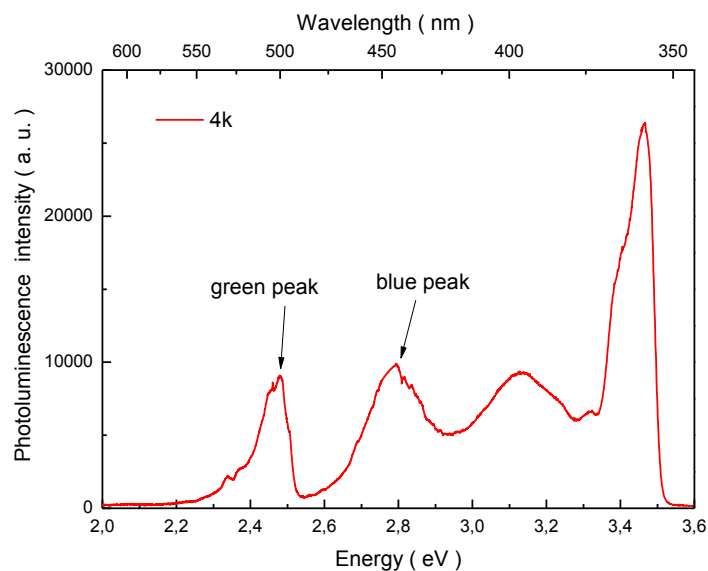


Fig. 3.2 Photoluminescence spectrum of a single nanowire at 4 K.

### 3.2.2 Cathodoluminescence spectroscopy

The nanowires have been further studied by CL spectroscopy by G. Jacopin at EPFL. The nanowires were kept on their growth substrate and excited under an acceleration voltage of  $V_{acc}=5$  kV in top-view configuration. The CL experiments were performed at room temperature in an SEM microscope JEOL 7001F equipped with a Jobin-Yvon Spectrometer HR320 and a CCD camera. Figure 3.3 a) shows a typical CL spectrum of several nanowires (the excitation area is shown in SEM image of Figure 3.3 b)). In agreement with the low-temperature  $\mu$ PL analyses, two spectral contributions are observed below the GaN NBE emission, presenting however a larger broadening. CL maps corresponding to these contributions have been recorded. Figures 3.3 c) and d) display the CL maps spectrally filtered for the detection ranges 440 – 480 nm (blue range) and 500 – 540 nm (green range), respectively. It is seen that the blue emission has a maximum for the excitation close to the nanowire perimeter where the radial InGaN QW is located. At the wire center the CL intensity is reduced by a factor of 30. The green emission is also maximal at the wire perimeter, however it remains strong for excitation positions all over the semipolar planes and drops only by a factor of 6 at the wire center. From the structural analyses it is clear that the ultra-thin InGaN QW on the semipolar planes cannot present an emission in the green range. Indeed, based on effective mass calculations, an  $\text{In}_{0.23}\text{Ga}_{0.77}\text{N}$  QW with a thickness of 0.7-1 nm presents an electron-hole transition close to the GaN NBE with a typical wavelength in 370-380 nm range. The green emission from the semi-polar planes can be understood by taking into account the relaxation of electron-hole pairs towards the potential minimum. The carriers created at different positions of the semi-polar planes diffuse to the In-rich region at the m-plane/semipolar plane junction and radiatively recombine there with an emission wavelength in the 500-540 nm range. It should be noted that the carrier relaxation towards the potential minimum observed in CL mapping should also take place under electrical injection.

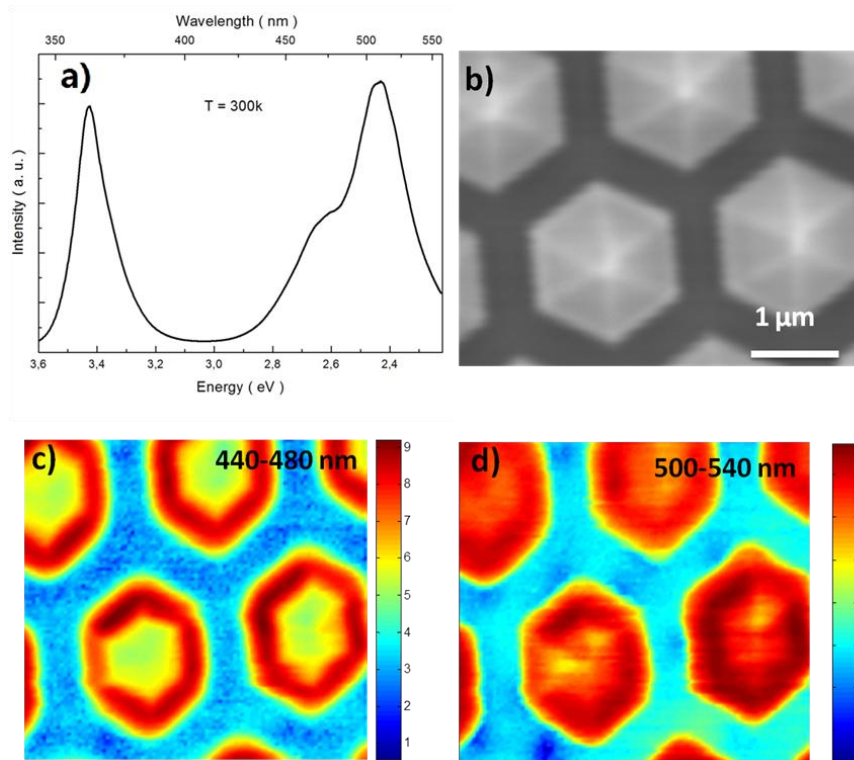


Figure 3.3 a) CL spectrum at room temperature under 5 kV acceleration voltage. b) SEM image of the excited area. c) and d) Spectrally filtered room temperature CL maps for the detection wavelength range of 440 – 480 nm (panel c) and 500 – 540 nm (panel d).

### 3.3 Single nanowire LEDs

#### 3.3.1 Fabrication of single nanowire LEDs

The nanowire samples have been processed in order to contact either single nanowires or a small number of nanowires. The schematic process to fabricate vertical single nanowire and few nanowire LEDs is shown in Figure 3.4. First, a bottom ohmic contact is defined onto the n-doped 2D GaN layer by optical lithography, ICP etching and metallization (Ti (10nm) / Al (30nm) / Ti (10nm)/ Au (150nm)) steps. Then the nanowires are insulated by encapsulation by a HSQ transformed into  $\text{SiO}_x$  by 1 h thermal annealing at 400 °C under  $\text{N}_2$  flux. It should be noted that a thin  $\text{SiO}_2$  layer (~50 nm) is deposited before HSQ encapsulation by PECVD to ensure a good electrical insulation. Micro-openings with aperture sizes ranging from 1  $\mu\text{m}$  to 11  $\mu\text{m}$  are then defined by electron beam

lithography. The exposed HSQ is first dry etched for 2 min using reactive ion etching with  $\text{CF}_4$  chemistry and then wet etched for 10 s by diluted HF (1 %) water solution to uncover the entire nanowires surface. The last wet etch step is implemented to avoid the exposure of the nanowire surface to  $\text{CF}_4$  plasma<sup>[1]</sup> which is known to damage the GaN p-doping<sup>[2][3]</sup>. Importantly, this procedure does not remove the underlying SiN mask. Finally, macroscopic transparent contacts to the exposed nanowires are defined by optical lithography, 300 nm ITO sputtering and thermal annealing at 400 °C for 10 min. Ti (10nm) / Au (150 nm) metallic contacts are evaporated to be used as bonding pads.

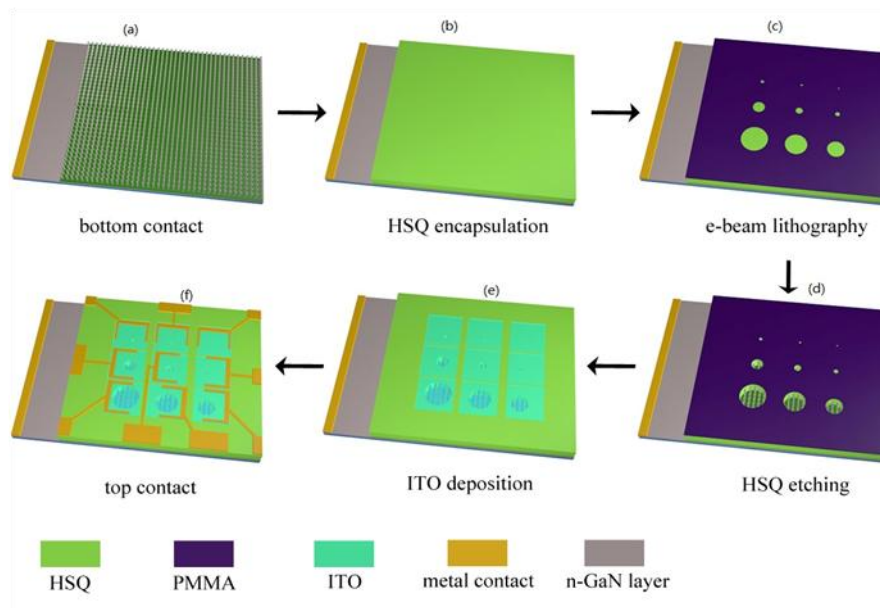


Figure 3.4: Process flow for vertical single nanowire and few nanowire LED fabrication: a) Bottom contact fabrication; b) Nanowire encapsulation into  $\text{SiO}_x$ ; c) Definition of microopenings by e-beam lithography; d) Etching of the  $\text{SiO}_x$  encapsulation; e) Deposition of ITO contacts to micro-openings; f) Final device with metal bonding pads.

Figure 3.5 a) shows an SEM image of micro apertures with diameters of 11, 7, 5, and 2  $\mu\text{m}$  before the ITO deposition. The apertures are well defined with a clear boundary between the encapsulated and the exposed nanowires. It is also seen that the encapsulation was fully etched and that the m-plane nanowire facets are uncovered. Figure 3.5 b) shows the general view of the final device with an ITO transparent layer and metal contacts. The average number of contacted wires is 1, 4, 7, 13 and 24 nanowires for 2  $\mu\text{m}$ , 5  $\mu\text{m}$ , 7  $\mu\text{m}$  and 11  $\mu\text{m}$  apertures, respectively. The smallest 1  $\mu\text{m}$  opening size

corresponds to a nanowire only partly contacted, which has been excluded from consideration.

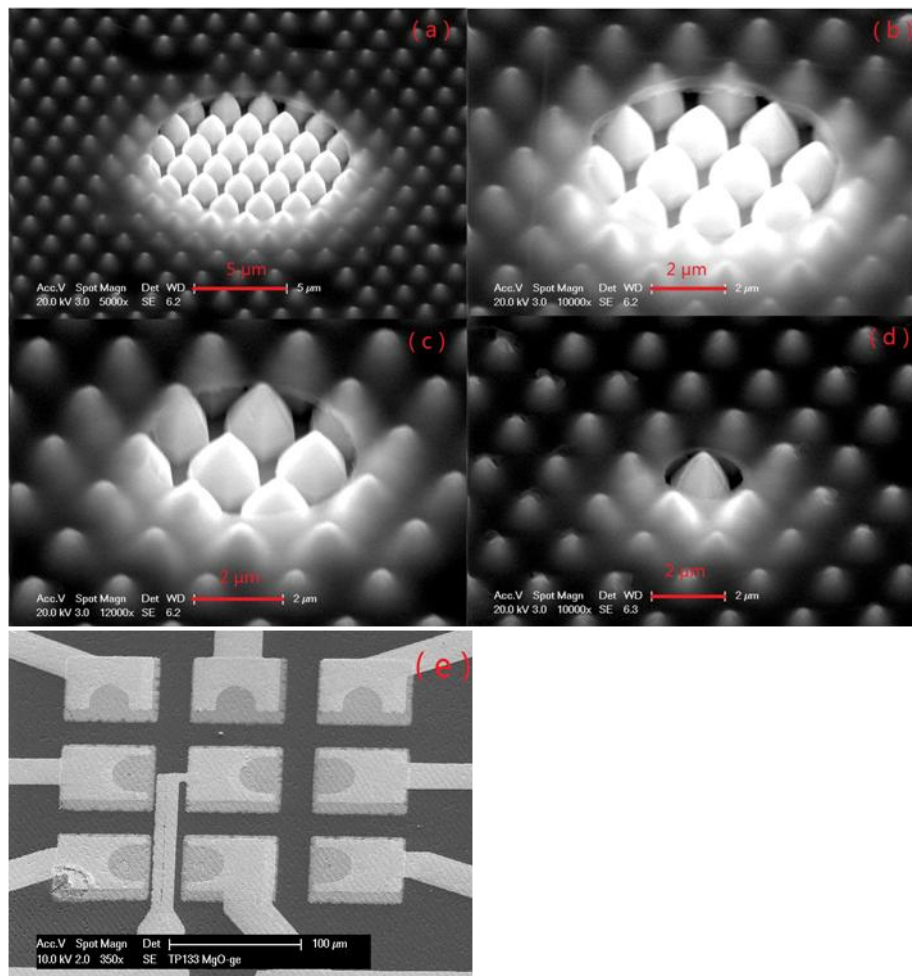


Figure 3.5 a)-d) SEM image of apertures of 2, 5, 7 and 11 μm before ITO deposition, respectively.  
e) SEM image of a fully processed device.

### 3.3.2 Electrical characterization of single nanowire LEDs

First, the electrical properties of single nanowire and few-nanowire LEDs were characterized. For different sizes LEDs the current level increases proportionally to the number of nanowires contacted within the micro-opening. This validates the fabrication procedure by demonstrating that the current flows only through the micro-openings with no parasitic leakage through the encapsulated nanowires beneath the ITO. A typical current density – voltage characteristic is shown in Figure 3.6. It should be noted that the area used for the current density calculation corresponds to the surface of the

micro-opening and not to the total m-plane surface of the NW active region. The LEDs exhibit a rectifying behavior with a diode opening at about 4 V. The leakage in the reverse bias is quite low, which proves that the insulating SiN mask is not damaged during the etching of SiO<sub>x</sub> encapsulation.

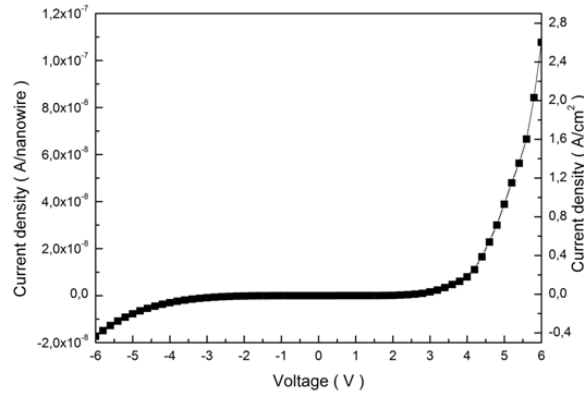


Figure 3.6. Current density – voltage characteristic of a 2 μm micro-opening LED.

### 3.3.3 Electroluminescence of single nanowire LEDs

The electroluminescence (EL) of the single NW and few NW LEDs was measured at room temperature using a UV-objective for efficient light collection, HR460 spectrometer and a CCD camera. Figure 3.7 shows the EL spectra (panel a)) and optical microscopy images (panels b) – d)) of a single nanowire LED (2 μm micro-opening) under operation for increasing injection current. At low injection density (0.67 A/cm<sup>2</sup>) the EL spectrum presents a single peak at 506 nm and the emission color appears as green on the corresponding microscope image (Figure 3.7 b). For higher injection currents the intensity of the green peak increases and a shoulder appears at shorter wavelengths peaked at 468 nm (Figure 3.7 c, injection current density ~2.8 A/cm<sup>2</sup>). Further current increase leads to a rapid growth of the blue peak intensity and a progressive blueshift of the green peak to 500 nm (the corresponding color is cyan). At high injection current density ( ~10.8 A/cm<sup>2</sup>) both peaks have the same intensity and the corresponding emission color is close to blue - cyan (Figure 3.7 d). The same evolution of the spectral shape has been observed for few-nanowire LEDs with micro-opening sizes from 5 to 11 μm (not shown for the sake of place). The following discussion is focused on the ultimate case of single nanowire devices. This evolution with injection current has been reported in chapter 2 in

nanowire LEDs of a similar structure. It is due to the predominant injection in the In-rich region at low excitation conditions, since the In-rich region is characterized by a higher saturation current. At high excitation the current is redistributed over the whole m-plane facet, which corresponds to the appearance of the blue emission.

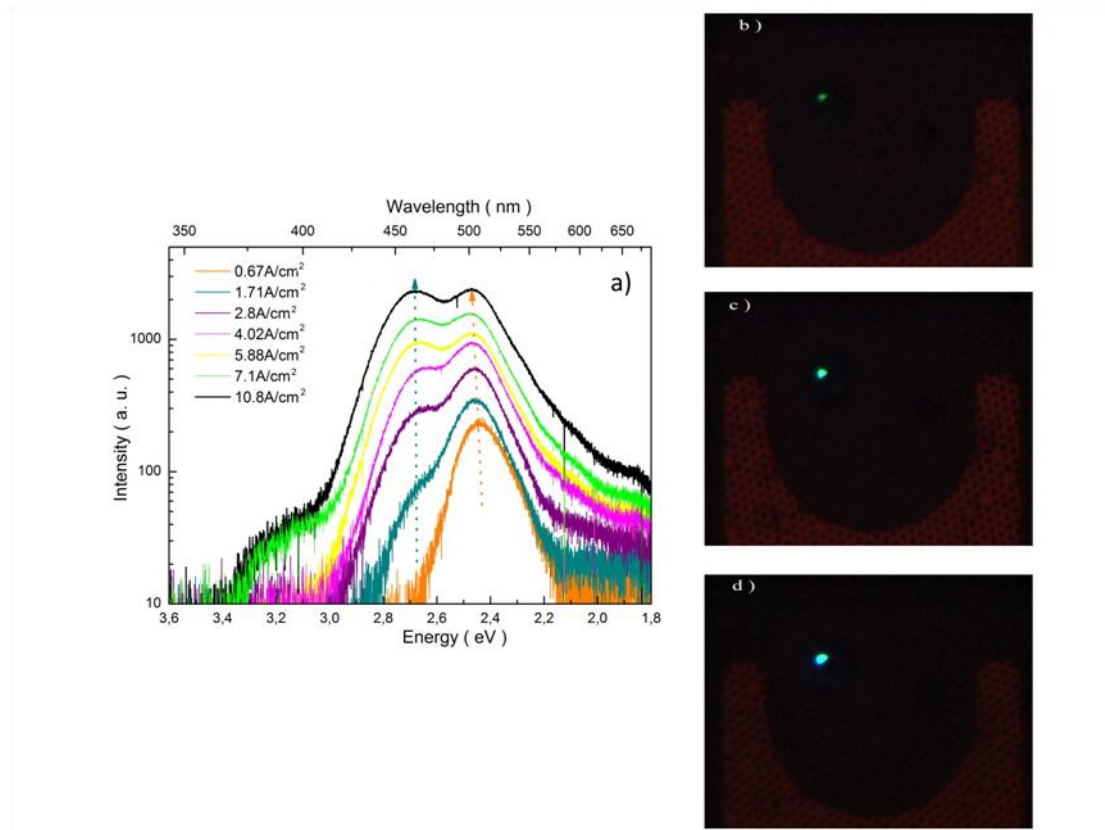


Figure 3.7. a) Single nanowire LED EL spectra from 0.67 A/cm<sup>2</sup> to 10.8 A/cm<sup>2</sup> injection current. b), c) and d) – Microscope images of the LED under operation with 0.67 A/cm<sup>2</sup>, 2.8 A/cm<sup>2</sup> and 10.8 A/cm<sup>2</sup> injection current, respectively.

The evolution of the EL intensity as a function of the driving current has been analyzed. In order to explore high injection currents without damaging the fragile single nanowire device by Joule heating, the measurements were performed at room temperature under pulsed excitation conditions with a duty cycle of 1 % and a current density ranging from 0 to 400 A/cm<sup>2</sup>. The light-current density characteristics and the corresponding normalized external quantum efficiency (EQE) are plotted in Figure 3.8. It is seen that for the chosen pulsed operation the efficiency saturates for injections above

250 A/cm<sup>2</sup>.

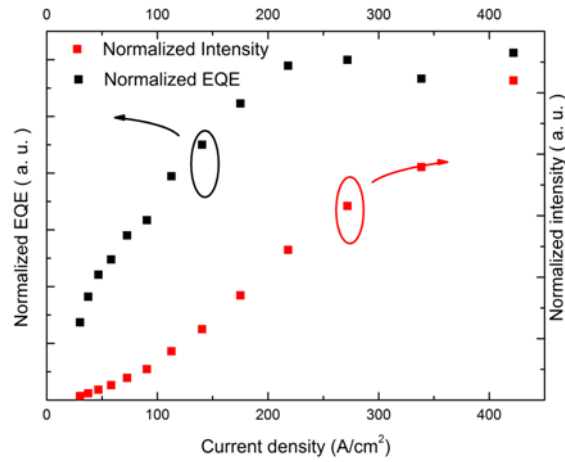


Figure 3.8. Light – current density characteristics (right scale) and normalized EQE (left scale).

The emission of single nanowire LEDs has been compared to the reference array device processed following the first “conformal ITO process” scheme (see definition below in section 3.5.1). Figures 3.9 a) and b) show the comparison between the normalized EL spectra of a single NW LED and of an array LED at low and at high injections. The conditions are chosen so that the current density is the same for both single wire and array devices. It is seen that the spectral shape for the single nanowire emission and for the array emission is very similar. At low current density (1.9 A/cm<sup>2</sup>) both the single wire and the array EL spectra present a dominant green peak at 2.45 eV and a weak shoulder at 2.64 eV. At high current density (10.5 A/cm<sup>2</sup>), the green and blue peaks have almost equal intensity in both devices. The peak positions are 2.46 eV and 2.68 eV with a FWHM = 254 meV and 178 meV, respectively. The FWHM values have been extracted using Gaussian peak fitting procedure. It should be noted that there is no increase of the FWHM in the array LED, which proves a good wire-to-wire homogeneity over the 300×300 μm<sup>2</sup> LED mesa.

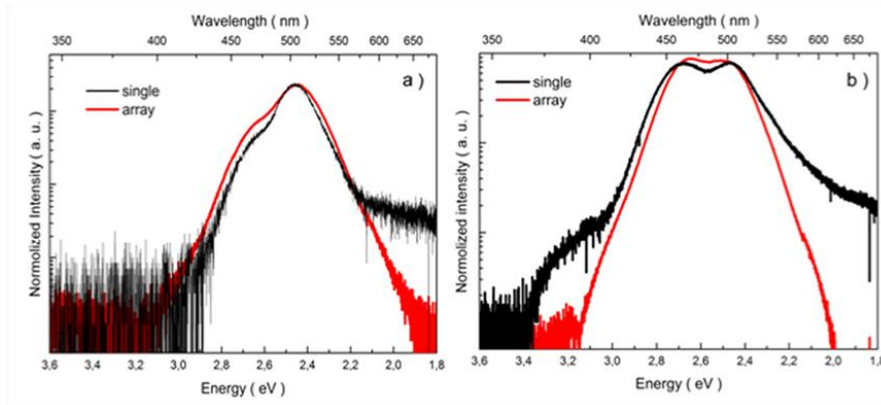


Figure 3.9. Comparison between the normalized EL spectra of a single nanowire LED and of a reference array LED at injected current density of  $1.9 \text{ A/cm}^2$  (panel a) and  $10.5 \text{ A/cm}^2$  (panel b).

### 3.4 Array LED color control by a post-growth treatment

#### 3.4.1 Processing of array LEDs with different contacting schemes

Similarly to single wire LEDs, the fabrication of array LEDs started by the definition of the ohmic contact to the 2D n-doped GaN layer using optical lithography, Inductively Coupled Plasma (ICP) etching and metal deposition. Then the top  $300 \times 300 \text{ }\mu\text{m}^2$  ITO contacts were defined by optical lithography, ITO sputtering (at room temperature at 80 W of applied rf power and 7 mT deposition pressure) and lift-off. The ITO was annealed at  $400 \text{ }^\circ\text{C}$  under  $\text{H}_2/\text{Ar}$  atmosphere for 10 min to improve its conductivity. Figure 3.10 d) shows SEM images of the nanowires covered with a conformal layer of the ITO. Ti (10 nm)/Au (150 nm) metallization was then deposited on the top mesa surface for bonding purposes leaving the central part of the mesa open for light extraction. This first processing scheme, illustrated in Figure 3.10 a), will be referred to as “conformal ITO process”.

After measurements, the processing was continued to remove the ITO from the nanowire top parts. For this purpose the sample surface was spin-coated with a protecting polymer (Shipley photoresist S1805), which covers the nanowire lower part. The excess of the resist on the nanowire tops was dry-etched for 2 min in an  $\text{O}_2$  plasma. Then the sample was immersed into an acid solution with

optimized mixing ratio<sup>[4]</sup> ( $\text{HCl} : \text{HNO}_3 : \text{H}_2\text{O} = 5 : 1 : 5$ ) for 2 min at room temperature in order to remove the unprotected ITO layer on the wire tops. After ITO etching, the sample was exposed to a  $\text{CHF}_3$ -based plasma (the used RIE parameters were 2 min, 30 mTorr, 300 W). The plasma treatment is known to degrade the conductivity of the Mg-doped GaN and to increase the metal-semiconductor barrier energy because of fluorine implantation. In our case, this treatment is used to reduce the conductivity of the unprotected parts of the p-doped GaN shell in order to restrict the electrical injection to the lower part of the m-plane sidewalls. It is important to note that this treatment does not attack the GaN semi-polar planes. After plasma etching, the protecting resist layer was removed in acetone. Figure 3.10 e) and its inset show SEM images of the nanowires after ITO etching and plasma treatment. It is seen that the ITO covers only the nanowire sidewalls, the top semipolar facets are free from ITO. Since the top metal bonding pads were damaged during the ITO etching, the top contact is deposited again by doing optical lithography, Ti/Au evaporation and lift-off. This second processing scheme, illustrated in Fig 3.10 b), will be referred to as “passivation process”.

After measurements, the processing was continued to physically remove the nanowire top parts. ICP treatment with  $\text{Cl}_2$  (25 sccm) /  $\text{BCl}_3$  (10 sccm) plasma was applied (the plasma power was 400 W and the pressure was 1 mTorr). The optimized etching time of 1 min allowed to remove ~150 nm of the nanowire height. Figure 3.10 f) shows an SEM image of the nanowires after ICP etching. It is seen that the roughness of the top semipolar surface increased after the ICP etching, however the major part of the m-plane sidewalls was preserved. The metal bonding part was not damaged by the ICP etching. This third processing scheme, illustrated in Fig 3.10 c), will be referred to as “ICP etch process”.

It is important to note that each processing scheme was first tested on different sample pieces. After optimization all three processing schemes were applied to the sample piece. The position of the measured LEDs on the sample surfaces was recorded and the same LED was characterized after each step to avoid possible long-range inhomogeneities.

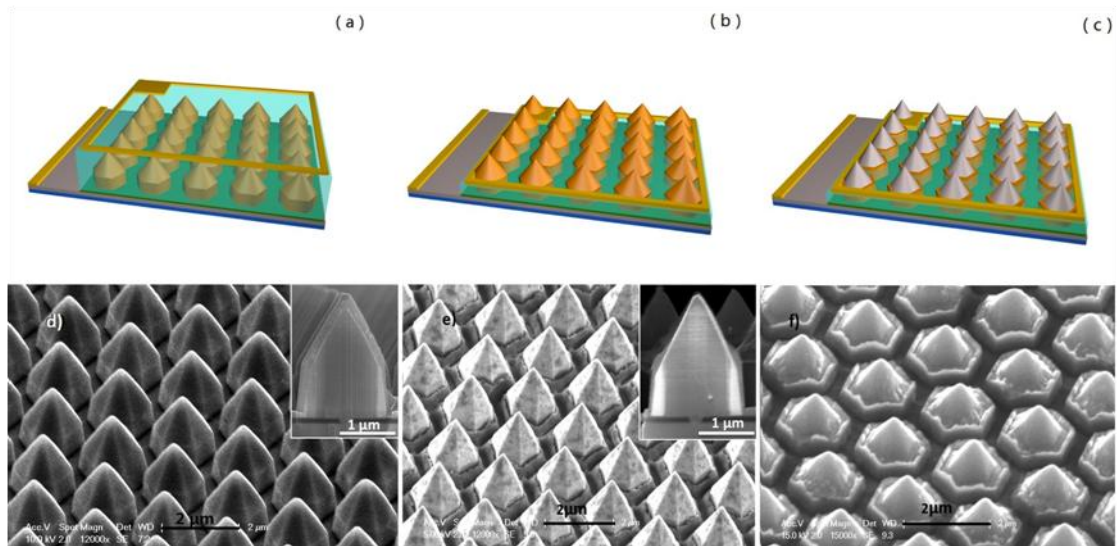


Figure 3.10. Processing schematics for a) – “conformal ITO process”, b) – “passivation process”, c) – “ICP etch process”. SEM images of the nanowire array after d) – ITO sputtering ; e) – ITO etching and  $\text{CHF}_3$  plasma treatment ; f) – ICP etching.

We now characterize the arrays LEDs processed following the three different schemes described above. It is important to note that all the time we characterize the same mesa, which undergoes additional processing steps. Therefore the electrical and optical results for the three processing schemes can be directly compared.

### 3.4.2 Electrical characterization of array LEDs with different contacting schemes

Figure 3.11 shows the I-V characteristics of the same LED with “conformal ITO process”, “passivation process” and “ICP etch process”. In all three cases the LED shows a rectifying behavior with low reverse leakage current and the diode opening voltage in the 2.6 V to 3.4 V range. The modifications are mainly observed in the direct I-V branch. A significant forward current reduction is seen after the ITO etch-back and  $\text{CHF}_3$  treatment (e.g. the current is reduced by a factor of 3 at 6 V). This demonstrates that the injection into the upper nanowire part was successfully inhibited. The forward branch of the I-V curve does not significantly change after the ICP etching, which again proves that the regions that have been physically removed by ICP etching were already inactive at the

previous “passivation process” step. We also note (see inset of Figure 3.11) that the passivation process does not significantly change the reverse current level, which means that this process does not introduce any conducting defects contributing to the leakage. The ICP etch process increases the leakage under reverse bias, which can be attributed to some damage during the etching process.

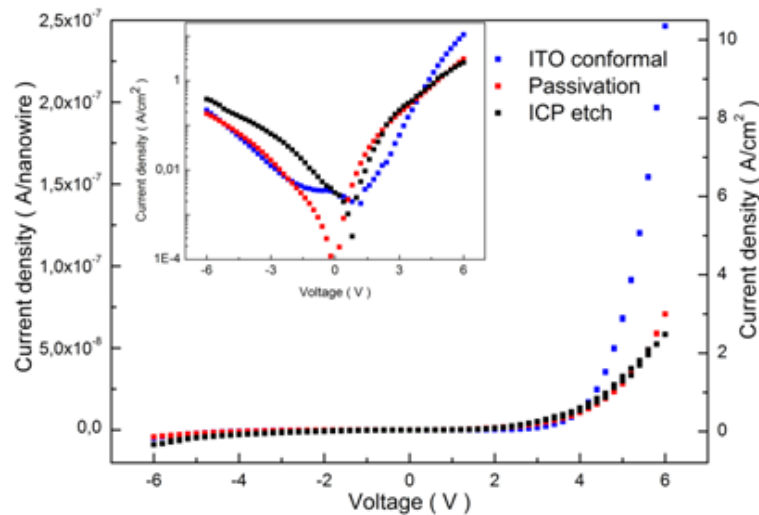


Figure 3.11 Current density-voltage characteristics of the same LED processed following three different schemes “conformal ITO process”, “passivation process” and “ICP etch process”. Inset: same characteristics in logarithmic scale.

### 3.4.3 EBIC characteristics of array LEDs with different contacting schemes

To assess the electrical activity of the semipolar planes at the microscopic level, the sample has been characterized by EBIC mapping. All measurements were performed at zero bias. The beam current arriving at the sample surface measured using a Faraday cup on the sample holder was equal to 0.9 nA with an acceleration voltage of 10 kV. Figure 3.12 shows the SEM cross-sectional image and the corresponding EBIC map of a cleaved LED with conformal ITO coverage (panels a) and b)) and of a cleaved LED after the ITO etch-back and  $\text{CHF}_3$  treatment (panels c) and d)). The induced current due to the electron-hole pair separation by the p-n junction appears as a bright contrast in panels b) and d). The comparison between the EBIC maps of panels b) and d) illustrate the suppression of the electrical signal at semipolar planes after the plasma treatment. Indeed, the electrical signal at the semipolar

planes is clearly seen for conformal ITO coverage. The average signal at the middle of the semipolar facets (marked with blue rectangle) is  $1.2 \times 10^{-7}$  A for “conformal ITO process” sample, whereas it is reduced to  $8 \times 10^{-9}$  A for sample fabricated following “passivation process”. The electrical signal from the semipolar planes has been suppressed by more than one order of magnitude, validating the efficiency of  $\text{CHF}_3$  plasma treatment to inhibit the p-type conductivity.

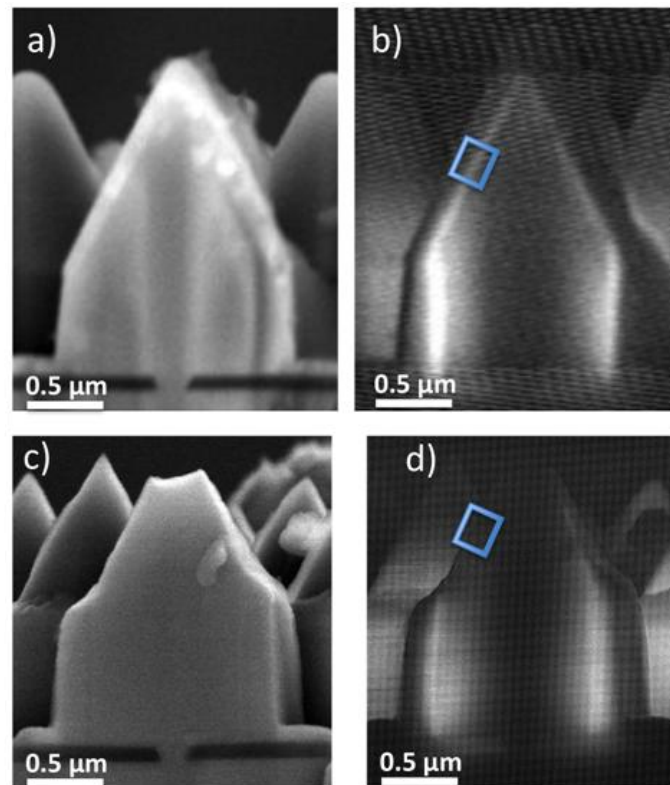


Figure 3.12: a) Cross-sectional SEM image of a nanowire from the LED with “conformal ITO process”; b) EBIC map under acceleration voltage of 10 kV corresponding to panel a); c) Cross-sectional SEM image of a nanowire from the LED with “passivation process”; d) EBIC map under acceleration voltage of 10 kV corresponding to panel c).

### 3.4.4 Electroluminescence of array LEDs with different contacting schemes

Figures 3.13 a), b) and c) present the room-temperature EL spectra for different injection currents for the same LED processed according to the three processing schemes. As previously mentioned, to

obtain quantitatively comparable results, the EL measurements were performed under strictly the same experimental conditions (i.e. same optics, integration time and slit size), while the LED position in the objective focal plane was chosen by maximizing the EL signal.

We first consider the conformal ITO processing scheme (figure 3.13 a) ). The evolution of the EL spectral shape with injection is quite similar to the above-described single nanowire LEDs. First, the green peak at 2.37 eV (FWHM= 216 meV) appears at low injection current of  $0.023 \text{ A/cm}^2$  (corresponding to 2.6 V applied bias). Then the blue peak at 2.61 eV appears for currents above  $0.15 \text{ A/cm}^2$  (bias above 3.4 V) and rapidly grows with increasing current. The intensity of the blue peak surpasses that of the green peak at 4.2 V (current density  $0.7 \text{ A cm}^{-2}$ ).

We stress that the area used for the current density calculations is constant for the three cases and corresponds to the projected surface of the device and not to the total active NW surface, which depends on the processing scheme.

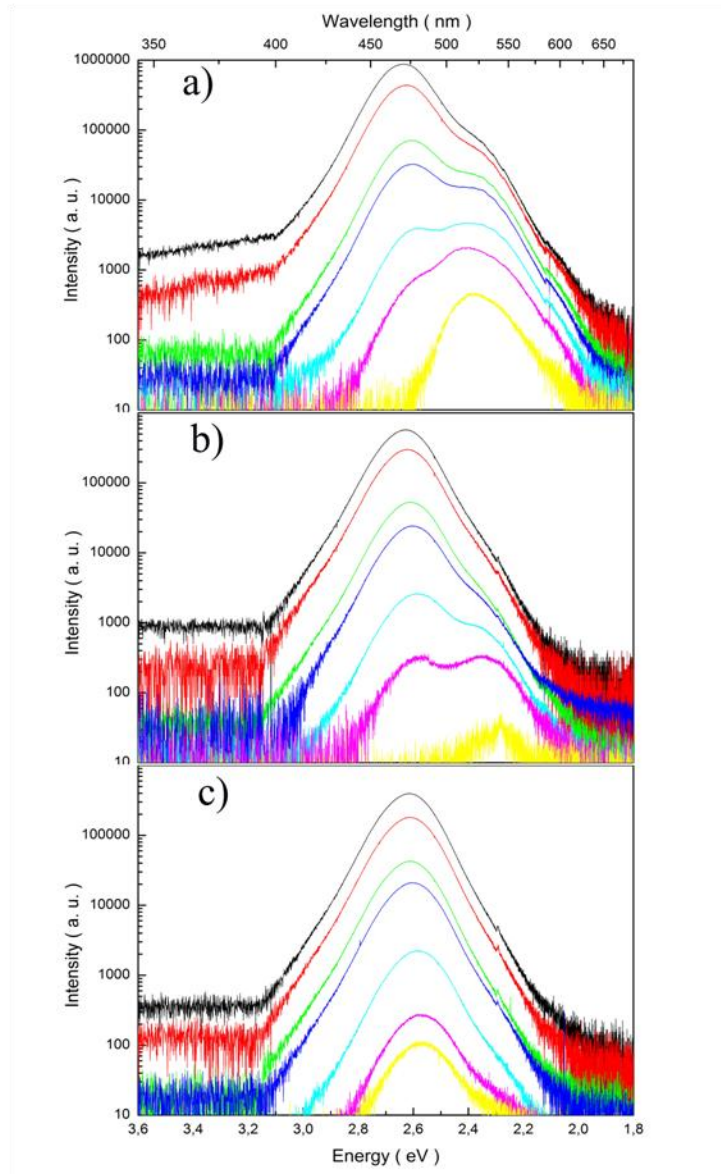


Figure 3.13. EL spectra in logarithmic scale for increasing injection current of the same LED processed following three different schemes “conformal ITO”, “passivation” and “ICP etch”.

Figures 3.14 a) and b) present the EL spectra for three processing schemes for the same voltage of 4.4 V and for the same electrical power of 1.1 mW. The peak intensities can be compared since the measurements were performed under the same conditions. Figure 3.14 clearly demonstrates that the developed passivation process is very efficient to suppress the green emission. For the same driving voltage the green emission is reduced by a factor of 7 in passivated LED and becomes a merely distinguishable shoulder. At the same time, the loss in the intensity of the blue peak is only 10% (based

on the Gaussian peak fitting). If the spectra for the same electrical power are compared, the green peak is suppressed by a factor of 25 and the blue peak intensity is enhanced by the passivation by a factor of 2. This enhancement of the blue emission is a result of the current concentration on the m-planes.

For the ICP-etch processing the green peak is completely suppressed, however a stronger intensity loss of 23% is observed with respect to the conformal ITO processing for the blue emission between the EL spectra collected at the same bias. This loss is 17% between the EL spectra collected at the same electrical power. This may be due to non-radiative defects at the nanowire top introduced by the ICP bombardment.

Based on both electrical and electro-optical results, the ITO etch-back and plasma treatment appears as a technique well suited for the color control, whereas the ICP etching introduces a loss of intensity and a leakage current.

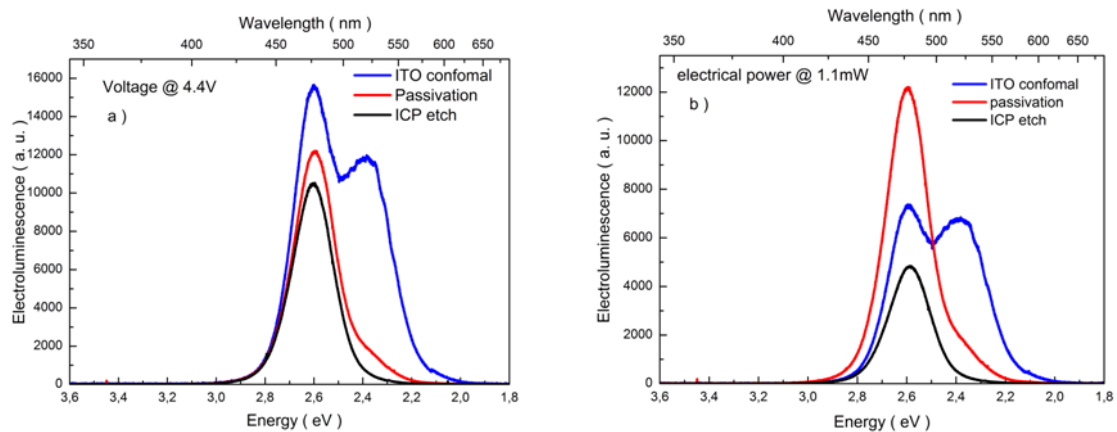


Figure 3.14 EL spectra of the same LED processed following three different schemes “conformal ITO”, “passivation” and “ICP etch” at a) – 4.4 V driving voltage and b) at 1.1 mW electrical power.

### 3.5 EBIC transient signal at the core/under layer interface of n-GaN

During the cross sectional EBIC observations an unusual behavior has been observed. For several wires a weak EBIC signal first appeared at the n-GaN core/n-GaN underlayer junction. This

phenomenon is accompanied by a strong suppression of the regular EBIC signal coming from the p–n junction. Under irradiation of the wire with electron beam for about 10 min the EBIC map was modified: the core/underlayer signal disappeared and transformed into a conventional signal from the p–n junction. Later the EBIC map remains stable and we have not observed other changes. The transitional regime is shown in Figure 3.15 (panels a-e)).

Figures 3.15 a) and b) show the SEM picture and the map of the nanowire EBIC in the beginning of observation while Figure 3.15 c) shows the EBIC map of the same wire after transformation. It should be noted that the signal at the interface core/underlayer of n-GaN layer is well defined as a narrow stripe in the bottom part. When this signal is present, no induced current at the p-n junction position can be detected. This unusual signal disappears under electrons irradiation and the signal of the p-n junction appears. Another wire cleaved perpendicular to its axis presenting the abnormal EBIC signal is shown in panels d) -e).

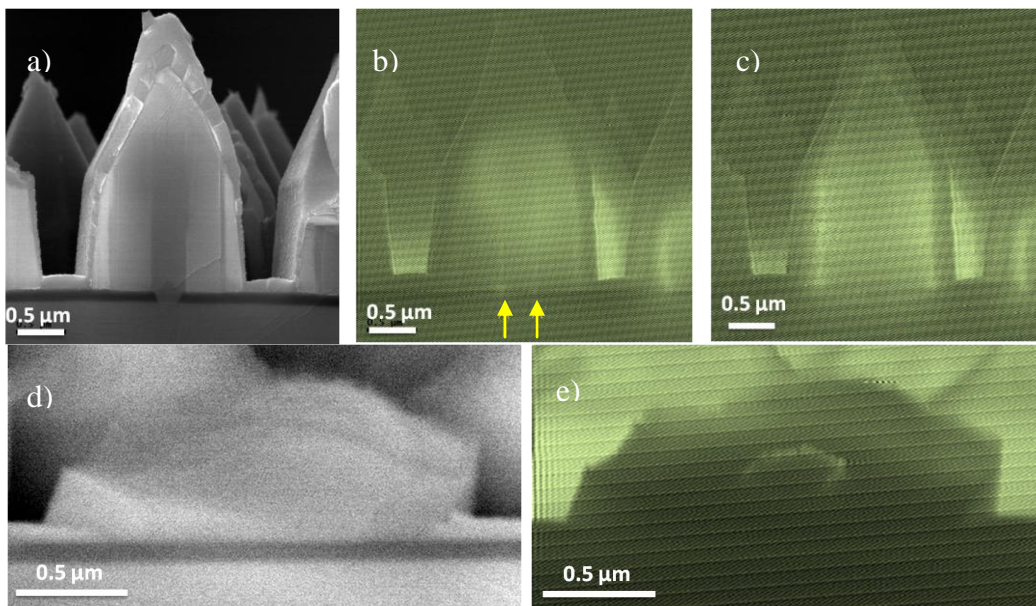


Figure 3.15. a) SEM image at  $V_{acc} = 10$  kV of a nanowire cleaved along its axis. b) corresponding EBIC map before transformation. The yellow arrows show the position of the abnormal signal. c) corresponding EBIC map after transformation. d) SEM image at  $V_{acc} = 15$  kV of a nanowire cleaved perpendicularly to its axis. e) corresponding EBIC map showing the signal at the core / n-GaN underlayer interface.

It may be supposed that a non-zero signal at the core/underlayer interface may arise from a small doping difference between these two layers. However this assumption cannot explain the absence of the EBIC signal at the p–n junction in the initial stage, so this hypothesis can be reflected.

We suppose that the EBIC signal from the core/underlayer interface can be related to the presence of charged traps at this interface. Separate measurements using electron holography technique have evidenced a potential variation at the core/underlayer interface in similar samples<sup>[5]</sup>. The mechanism that we propose to explain the unexpected EBIC signal is illustrated in Figure 3.16(a), which shows the schematized band profile perpendicular to the wire axis. (For simplicity, the electron blocking layer and the quantum well are not represented.) The negatively charged traps at the core/underlayer interface can perturb the band profile and induce separation of generated charges. The proposed mechanism is similar to the case of grain boundaries in Zinc oxide (ZnO) 2D layers<sup>[6]</sup>. At the same time they act as a barrier for electrons generated at the p–n junction preventing their collection by the core. The generated holes can either cross the interface, diffuse toward the p–n junction and be collected or can be trapped at the interface. Hole trapping compensates the negative charge and decreases the potential barrier associated with the interface so that it becomes transparent for electrons as illustrated in Figure 3.16(b). This leads to a reduction of the EBIC signal from the core/underlayer interface and the appearance of the normal EBIC signal from the p–n junction.

Note that a suppression of the EBIC contrast due to a modification of a defect charge state under electron beam irradiation has previously been reported in InGaN/GaN 2D structures. The transformation of the EBIC map in our experiments was persistent, suggesting that irradiation by electrons changes the interface state between the core and the n- GaN underlayer.

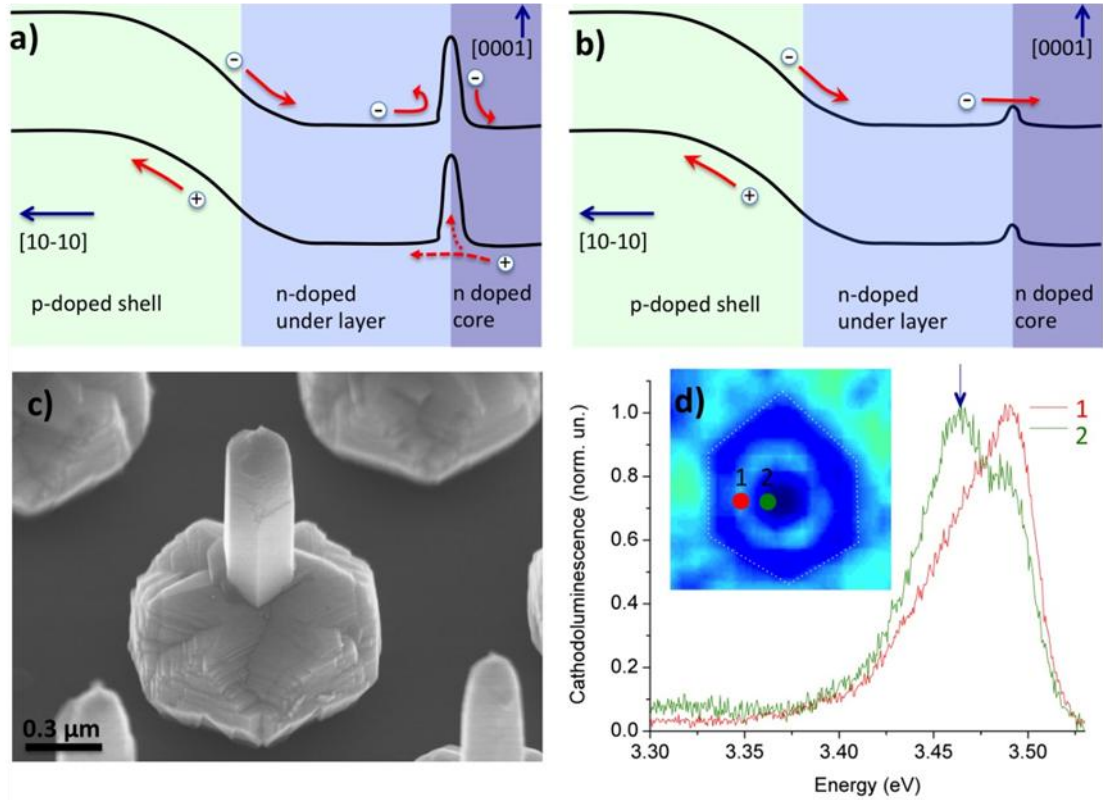


Figure 3.16. Band diagram before (a) and after (b) the transformation. c) SEM image tilted at  $45^\circ$  of the nanowires after KOH etching. d) CL spectra at 7 K with  $V_{acc} = 5$  kV in top view excitation configuration at the interface between core/ n-GaN underlayer (position "2") and in the n-GaN underlayer near the p-n junction (position "1") . The insert shows the integrated CL intensity map for energies between 3.35 eV and 3.55 eV indicating the positions of the excitation points.

We further analyzed the optical behavior of the core/underlayer interface by CL and we investigated the effect of wet etching. Figure 3.16 c) shows the SEM image after KOH etching. It should be noted that the epitaxial layers in the radial direction (i.e. the p-GaN shell, the active region and the n-GaN underlayer) are etched faster than the n-GaN core. In addition, the CL spectra for excitation positions in the n-GaN underlayer near the p-n junction and at the interface between n-GaN core and underlayer show a difference as seen in Figure 3.16 d). For excitation at the interface, a shoulder peak at 3.46 eV was observed in addition to the GaN NBE emission at 3.48 eV. These observations may indicate a polarity change at the interface between the GaN core and the underlayer. Indeed, the inversion domain boundary behaves as shallow traps (30-40 meV below the gap)<sup>[8][9]</sup>, which are optically active

and have shown emissions from 3.45 to 3.46 eV<sup>[10][11]</sup>. Polarity inversion in the MOVPE growth nanowires was reported by several teams<sup>[12][13]</sup>. We have attempted to measure the polarity by convergent beam electron diffraction (CBED). However, the CBED analyses have given controversy results: the measurements performed at GLO showed that the core of the nanowires exhibited Ga polarity (in accordance with the polarity of the GaN template used for the NW growth and the weak reaction of the core to the KOH attack), while the measurements by L. Largeau at the LPN showed a nitrogen polarity (in agreement with the shape of core with a flat top c facet<sup>[14]</sup>). Unfortunately, CBED measurements on entire core-shell structures were not conclusive due to the lamella deformation induced by FIB preparation. In conclusion, the polarity of the underlayer and the n-GaN shell could not be unambiguously determined, however, the pyramidal summit of nanowires defined by the semi-polar facets is in favor of a Ga polarity.

It is possible that the highly Si doped GaN core could be the origin of the abnormal EBIC signal at the core/underlayer interface. For GaN thin films, Si has been identified as an anti-surfactant which can induce a mask effect by forming Si-N<sup>[15]</sup>, or islets of Si<sub>3</sub>N<sub>4</sub><sup>[16]</sup>, or even a monolayer of SiGa<sub>3</sub>N<sub>3</sub><sup>[17]</sup>. This mask effect is used to induce a 3D growth and reduce the dislocation density in 2D GaN layers<sup>[18][19]</sup>. In the case of highly doped nanowires grown by MOVPE, a surface layer of SiN<sub>x</sub> on the side wall has been shown to promote the wire morphology<sup>[20]</sup>. We speculate that this SiN<sub>x</sub> layer is responsible for the formation of a potential barrier at the n-GaN core/underlayer interface leading to the abnormal EBIC signal.

Whatever the nature of the defects at the n-GaN core/underlayer interface, it is clear that the presence of a potential barrier at this interface in some nanowires can have a detrimental effect on the LED performance. Indeed, this barrier increases the access resistance and affects the injection homogeneity from wire to wire. It can be concluded that the quality of the n-GaN core/underlayer interface corresponding to the change of the growth mode from axial to radial is very important for device performance.

To determine the percentage of nanowires with abnormal EBIC signal, the cross-sectional mapping is not suitable. Therefore, I used EBIC maps in top view. In order to increase the spatial resolution of the EBIC signal, two samples were analyzed: the first LED with the ITO etch-back contact on the tops of nanowires (Figures 3.17 a) -d) ) and the second LED with ICP etching process (figures 3.17 e) -f)).

The EBIC map displayed in Figure 3.17 b) shows that some nanowires have a weak EBIC signal which is located close to the center of the wire (they are marked by red arrows). The figure 3.17 d) shows the detail of the image where the two types of nanowires with the "normal" and "abnormal" EBIC signal are present. The abnormal signal can be better defined in the sample where the top of the nanowires was etched by ICP (Figures 3.17 e) -f)) because in this case the semi-polar facets are completely removed. For both samples, there are 7-10% of nanowires with "abnormal" EBIC signal.

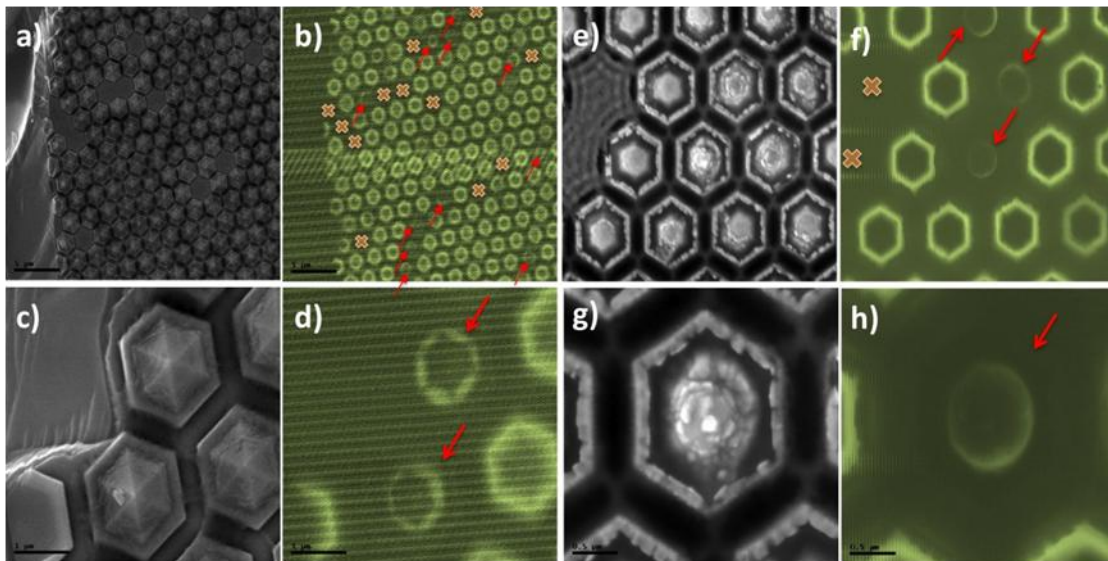


Figure 3.17 a) SEM image and b) its corresponding EBIC map of an LED with the ITO etch-back contact on top of nanowires. The crosses indicate the position of missing wires, the red arrows indicate nanowires with abnormal EBIC signal. c) and d) – the same sample as a) and b) for a higher magnification showing a detail of the abnormal signal. e) SEM image and f) its corresponding EBIC image of LED with ICP etching process. g) and h) – the same sample as e) and f) for higher magnification showing a detail of the abnormal signal. All pictures and maps are acquired at  $V_{acc} = 10$  kV.

I should note that the abnormal EBIC signal in top-view maps for whole nanowire has a larger diameter ( $\sim 700$ - $850$  nm) than that of the nanowire core ( $\sim 250$ - $300$  nm). This is contrary to the case of the nanowires cleaved closed to their base, where the abnormal signal follows the core boundary (e.g.

Figure 3.15 e)). I believed that this is due to the projection effect and the homogeneity of the signal along the axis. Indeed, for the situation shown in Figure 3.15 c), the widening of the signals can arise from the upper part of the nanowire.

### **3.6 Correlation between EBIC maps and electroluminescence maps**

For evaluating the impact of the abnormal EBIC signal on the EL properties of an LED, I recorded the optical microscopy images of the device under operation. I used the sample processed following the ICP etching scheme who gives a better definition of abnormal EBIC signal. The same area was then mapped by the EBIC microscopy.

Figure 3.18 shows EL maps, SEM images and EBIC maps for the same area close to a contact. The figures a) and b) show the EL maps for two applied voltage values of 4 V and 6.2 V, respectively. First of all, there is a strong inhomogeneity of the EL from wire to wire both at low injection and at high injection. The EL intensity is not uniform and some nanowires do not show any emission at all. The percentage of active nanowires (i.e. generating electroluminescence) at low injection is only ~ 20-30%. It increases only slightly at higher injection. The SEM image (panel c)) of the same region does not show abnormal morphology. The EBIC image (panel d)) shows a current generation much more homogeneous than the EL signal with only ~ 10% of nanowires that generate weak or no signal.

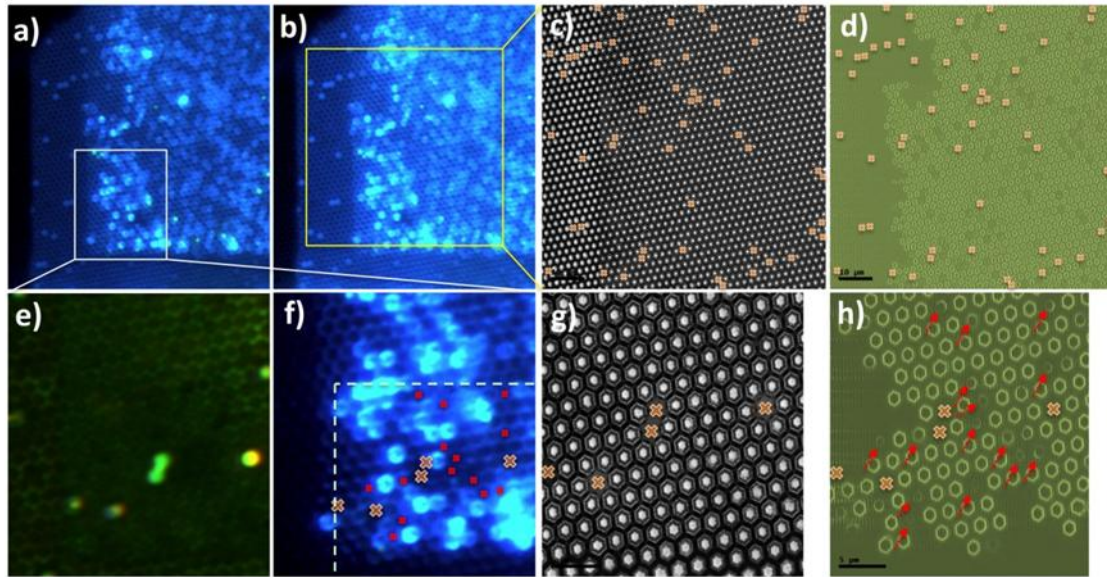


Figure 3.18. EL map of the same area for an applied voltage of a) 4 V and b) 6.2 V. c) SEM image of the region shown with a rectangle in panel b). The pink crosses show missing nanowires. d) EBIC map corresponding to the panel c). e) Optical microscopy image of the region we observed (marked by a rectangle in panel a)) to visualize missing nanowires. f) Image of the same area for an applied voltage of 4 V. The pink crosses indicate the missing nanowires, the little red crosses indicate the position of nanowires producing an abnormal EBIC signal. g) SEM image of the area marked by a rectangle in panel f). pink crosses indicate the missing nanowires. h) EBIC map corresponding to panel g). The red arrows point to the nanowires with abnormal EBIC signal.

The maps at higher magnification (panels e) - h) ) identify the nanowires with abnormal EBIC signal. We can find them on the EL map. It should be noted that each wire with abnormal EBIC signal shows no EL. This has been shown in the panel f), where the nanowires with abnormal EBIC signal are indicated by red crosses. However, the reverse is not true: a wire having a normal EBIC signal does not necessarily show EL. In general, the number of nanowires producing EL ( $\sim 20\%$ ) is well below the number of nanowires having a normal EBIC signal ( $\geq 90\%$ ).

### 3.7 Front n-contact LED

To avoid the impact of the potential barrier at the n-GaN core/underlayer interface, we have developed an alternative method of making n type contact for injecting electrons directly in the n-GaN underlayer.

The fabrication steps are illustrated in Figure 3.19. The fabrication process begins by depositing a 200 nm ITO layer (panel a)) on the entire surface followed by a partial ITO etching from the upper part of the nanowires (panel b)). Then the p-GaN shell is ICP-etched on the semipolar facets and on the upper part of the m-plane facets leaving the exposed n-GaN underlayer (panel c)). The ITO layer forming the contact on the p-GaN shell is metallized on the sample edge to allow subsequently the wire bonding (panel d)). The sample is then encapsulated into a HSQ layer to electrically isolate the contact to p-GaN shells (panel e)). Excess HSQ is etched with RIE. To contact the n-GaN underlayer, 300 nm ITO layer is deposited on top and patterned by lithography and a lift-off. Finally, a metallization Ti / Au and lift-off are used to form the top metal contact for the bonding (panel f)). Panel g) illustrates the final structure of the LED, where the holes are injected through the ITO at lower part of the nanowire while the electron are injected through the top ITO contact directly in the upper n-GaN underlayer (instead of being injected through the core).

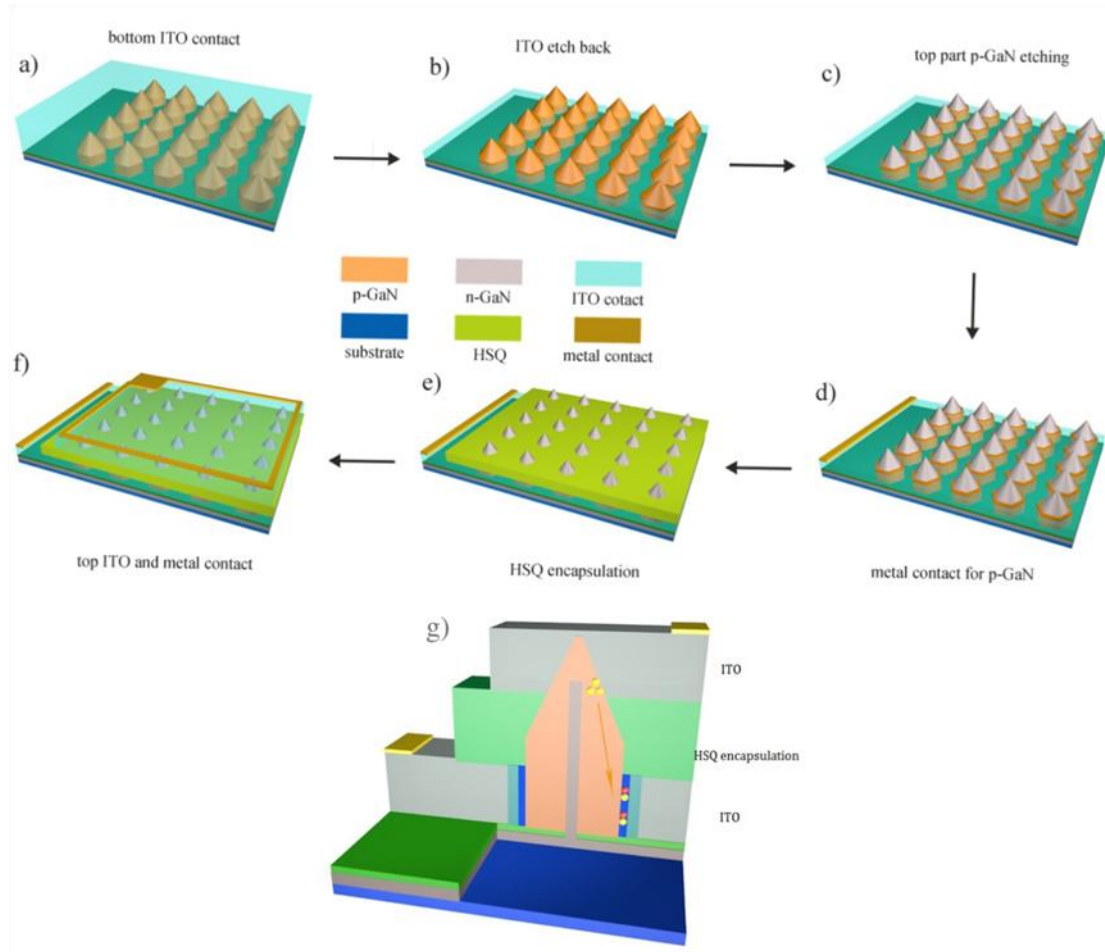


Figure 3.19. LED manufacturing steps before n-contact: a) ITO contact deposition; b) partial etching of ITO; c) ICP etching of the p- GaN shell; d) definition of a metal contact to the ITO layer; e) encapsulation with the HSQ and its partial etching; f) lithography and deposition of ITO and the metal contact for the injection of electrons. d) Schematic of the final device.

First, the electrical properties of the device were tested. The I-V curve is shown in Figure 3.20 a). The characteristic shows a rectifying behavior despite a high level of leakage for inverse voltages above 2 V (e.g. current density is  $75 \text{ A cm}^{-2}$  at 6 V and  $-35 \text{ A/cm}^{-2}$  to -6 V). We note that LEDs contacted through the n-GaN core show current densities ten times lower. It is possible that the leakage problem arises from a parasitic conduction between the first ITO layer and the n-GaN underlayer. Indeed, after the ICP etching of the upper part of the nanowire, the ITO surpasses the edge of the bottom part of p-GaN shell and it is not mechanically supported by the nanowire (Figure 3.10f)). At the time of HSQ

encapsulation, the ITO layer can break and touch the n-GaN layer creating local short circuits. Another hypothesis to explain the high leakage is due to defects in the SiN<sub>x</sub> mask (and especially places with "missing" nanowires where the mask was not fully open). Indeed, compared to the LEDs discussed above, the area of the p-contact deposited directly on the SiN<sub>x</sub> mask is around 1 cm<sup>2</sup> against 900 μm<sup>2</sup> for a standard method. We can therefore expect an increase of the leakage current by a factor of 10<sup>2</sup>.

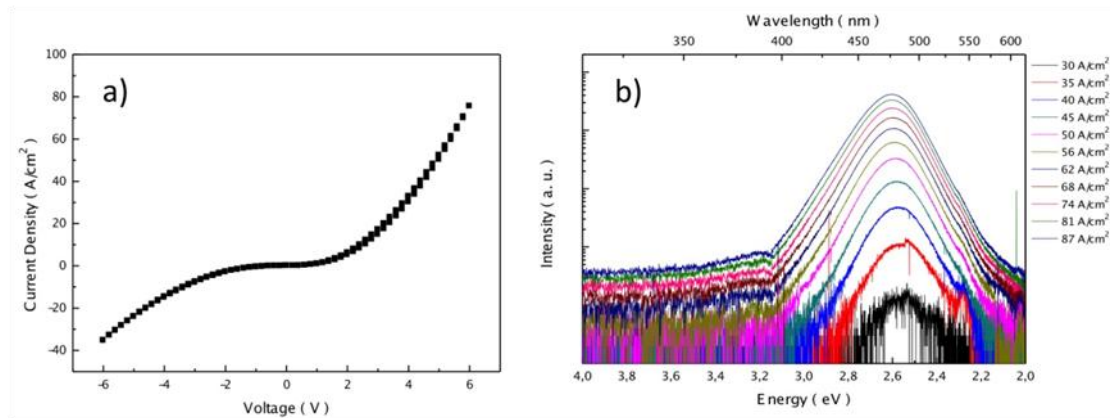


Figure 3.20. a) I-V curve LED with front n-contact. b) EL spectra with the increasing current density.

Despite the high leakage current, the LED with front n contact shows the EL from an applied voltage of 3.3 V. This number is the same as for LEDs with the electron injection through the n-GaN core. The EL spectra for an increasing current injection are shown in Figure 3.20 b). The emission shows the peak at 2.58 eV (484 nm). The peak energy remained stable for the entire current range.

Now, I evaluate the improvement that we can expect concerning the percentage of active nanowires through direct injection of electrons in the n-GaN underlayer without passing through the potential barrier at the n-GaN core/underlayer interface. I did a simple statistics between (i) a standard LED with conformal ITO contact and electrons injected through the core, (ii) an LED fabricated following the ICP etching process and the injection of electrons from the core and (iii) an LED with front n-contact. Figure 3.21 a) - c) shows examples of the EL maps for these three cases, respectively. In the case (i), there is 19% of active nanowires, in the case (ii) the number is 22%. It is found that the ICP etching, although it introduces defects as discussed above, does not decrease the percentage of active

nanowires. For the LED with front n-contact, the percentage of active nanowires reached 65%. An intermediate magnification EL map is shown in panel d). The comparison with the map for the case (ii) (e.g. shown in Figure 3.17 b)) shows an improvement of emission uniformity. It is possible that the EL performance may be further improved by optimizing the fabrication processes. Indeed, the map of panel d) shows that most of the inactive nanowires are gathered at a connected geometric fields, which may indicate process problems in these regions.

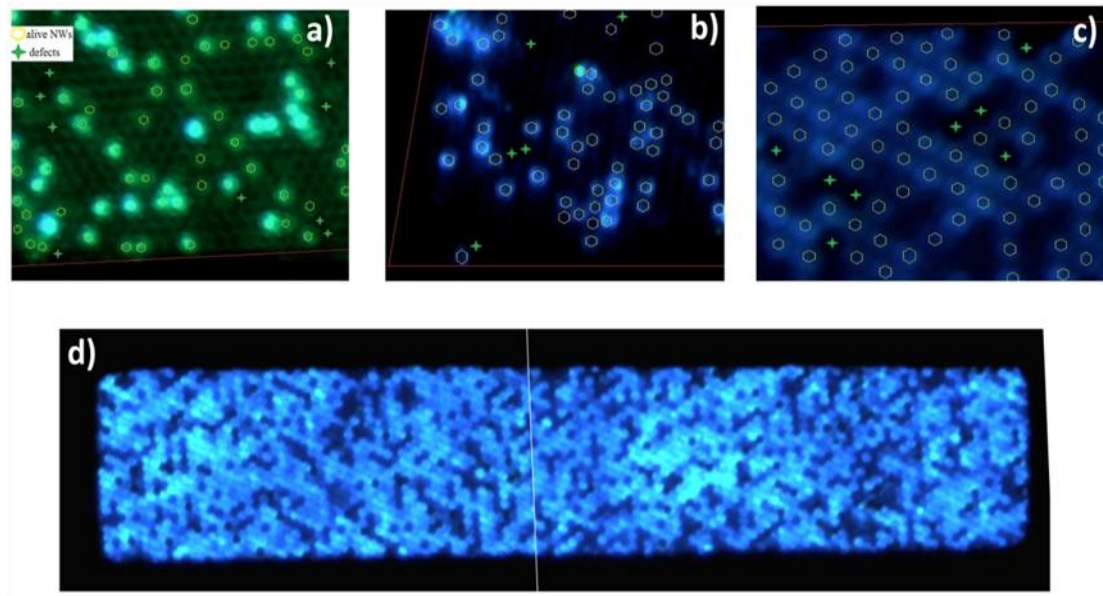


Figure 3.21. EL maps for LED processes with a) injection of electrons through the core and a conformal top ITO contact; b) injection of electrons through the core and the upper part of nanowires etched by ICP ; c) front n-contact LED and electrons injected directly in the n-GaN underlayer. d) Intermediate magnification of EL map showing emission fluctuations over a large area.

The temperature dependent EL spectra of “front contacted” LEDs have been measured for different injection current density level at 100 K, 150 K, 200 K and 250 K. At 100 K, the EL (figure 3.22 (a)) appears at 5.3 V and shows a single peak (2.71 eV) at low current density ( $36 \text{ A/cm}^2$ ). The quite high turn on voltage is due to a low percentage of activated Mg acceptors at low temperature. With the increase of the current density, the low energy peak grows fast and a second peak starts to appear at higher energy (3.05 eV) with a slow intensity increase. At higher current density ( $87 \text{ A/cm}^2$ ), the low

energy peak becomes dominant while the high energy peak turns into a shoulder peak. The appearance of high energy peak can be explained by the current overflowing into Mg-doped p-GaN due to the ineffective current blocking by the electron blocking layer. No energy shift can be observed for two peaks. The EL spectrum at 150 K in figure 3.22 (b) shows a different evolution with injection current: the peak energy shows a 90 meV blue shift from 2.59 eV to 2.68 eV with increasing current density. This energy shift becomes even stronger when the temperature goes to 200 K as shown in figure 3.22 (c). At low current density of 20 A/cm<sup>2</sup>, the low energy peak is at 2.54 eV, while this peak shifts to 2.66 eV at current density of 87 A/cm<sup>2</sup>. The shoulder high-energy peak almost disappears at this temperature. At high temperature range, nevertheless, the energy shift becomes weaker showing a 70 meV shift (in figure 3.22 (d)) for 250 K, while at room temperature no shift is observed.

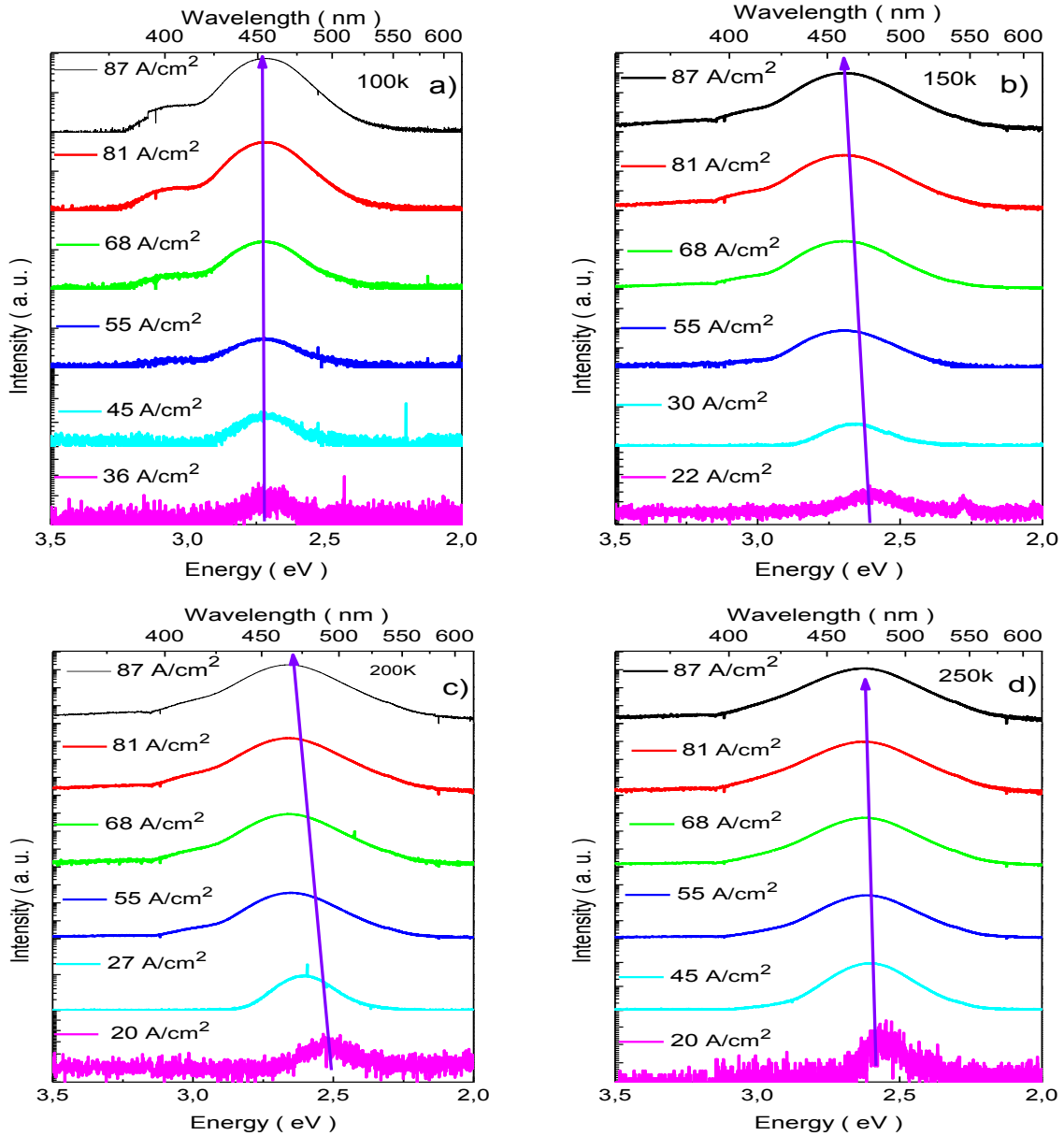


Figure 3.22: a) the EL spectrum at 100 K. b) at 150 K. c) at 200 K. d) at 250 K.

To further analyse the emission energies observed for different temperatures, the average values are extracted at 20 A/cm<sup>2</sup>, 55 A/cm<sup>2</sup> and 87 A/cm<sup>2</sup> current density and plotted in figure 3.23. At high current density above 55 A/cm<sup>2</sup>, a continuous of reduction of emission energy, which decreases from 2.71 eV (100 K) to 2.59 eV (300 K), is attribute to the temperature dependent decras of the bandgap follow a Varshni law. At low current density, blue shift can be observed at 150 K, 200 K and 250 K due to indium composition variation in the quantum

wells. Indeed, under certain thermal activation, the electron-hole pairs delocalize into the high indium composition region and produce emission at higher energy.

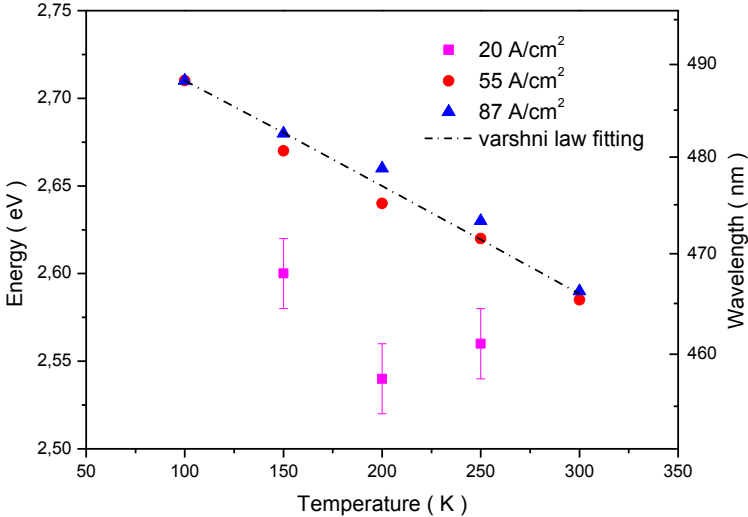


Figure 3.23: Emission energy for different temperatures.

### 3.8 Conclusions

In this chapter, core/shell InGaN/GaN nanowire LEDs were fabricated following different processing schemes and extensively characterized. Single-nanowire vertical LEDs with the same contact layout as the array devices were investigated, showing that the single-nanowire electroluminescence presents the same spectral features and the same broadening as the array LED emission. Modification of the contact layout and a post-growth  $\text{CHF}_3$  plasma treatment allows suppression of the unwanted green contribution at medium and high injection without losing the electroluminescence intensity in the blue spectral range. EBIC microscopy on the LED cross-section confirms the inhibition of the electrical activity in the parts exposed to plasma treatment. ICP etching of the In-rich region allows suppression of the green emission for all injection currents, but a loss of intensity in the blue spectral range is observed. The selective contacting of the m-plane and the plasma treatment of the nanowire top appear as a promising solution for controlling the color of core/shell nanowire LEDs with inhomogeneous internal composition. Furthermore, I analyzed the injection inhomogeneity induced by charge traps at the interface between the nanowire n-GaN core and the radially grown n-GaN layer. The EBIC microscopy indicates the presence of two kinds of signals. This phenomenon impedes the homogeneous injection and reduces the efficiency of the nanowire LED array. In order to avoid injection through a potential barrier at the core/underlayer interface, I fabricated the “front contacted” LEDs realizing electrons injection directly into n-GaN underlayer. The “front contacted” LEDs present an increased yield of the active NWs in the EL maps from 19% to 65%. The high yield for “front contacted” LEDs proves that the front electron injection allows to reduce the negative impact of the potential barrier at the core/underlayer interface.

## References

- [1] Chu R, et al. “Impact of CF<sub>4</sub> plasma treatment on GaN” IEEE Electron Device Lett. (2007) 9781
- [2] Massoubre D, et al. “Micro-structured light emission from planar InGaN light-emitting diodes” Semicond. Sci. Technol. 29 (2014) 15005
- [3] Polyakov A Y, et al. “Proton implantation effects on electrical and luminescent properties of p-GaN” J. Appl. Phys. 94 (2003) 3069
- [4] Je-Hsiung L and Kanicki J “Patterning of transparent conducting oxide thin films by wet etching for a-Si:H TFTLCDs” J. Electron. Mater. 12 (1996) 1806
- [5] Tchernycheva, M, et al. “Core-shell InGaN/GaN nanowire light emitting diodes analyzed by electron beam induced current microscopy and cathodoluminescence mapping.” *Nanoscale* 7.27 (2015): 11692-11701.
- [6] C. Leach, “Crystal plane influence of the EBIC contrast in zinc oxide varistors”, J. Eur. Ceram. Soc., 21 (2001), 2127.
- [7] P. S. Vergeles and E. B. Yakimov, “EBIC investigation of InGaN/GaN multiple quantum well structures irradiated with low energy electrons”, J. Phys., 281 (1) (2011), 012013.
- [8] W.-C. Yang, et al. Photoelectron emission microscopy observation of inversion domain boundaries of GaN-based lateral polarity heterostructures, J. Appl. Phys. 94, (2003), 5720.
- [9] Vincenzo Fiorentini, Origin of the efficient light emission from inversion domain boundaries in GaN, Applied Physics Letters 82, 1182 (2003)
- [10] P. J. Schuck, et al. Spatially resolved photoluminescence of inversion domain boundaries in GaN-based lateral polarity heterostructures, Appl. Phys. Lett. 79, 952 (2001);
- [11] Ronny Kirste, et al. Temperature dependent photoluminescence of lateral polarity junctions of metal organic chemical vapor deposition grown GaN, J. Appl. Phys. 110 (2011), 093503
- [12] X. J. Chen, et al., Homoepitaxial growth of catalyst-free GaN wires on N-polar substrates, Appl. Phys. Lett. 97 (2010), 151909
- [13] Xue Wang, et al. Polarity Control in 3D GaN Structures Grown by Selective Area MOVPE, Cryst. Growth Des., 12 (2012), 2552–2556
- [14] X. J. Chen, et al. «Catalyst-free growth of high-optical quality GaN nanowires by metal-organic

vapor phase epitaxy, Appl. Phys. Lett. 99 (2011), 251910

[15] S. Tanaka, et al. Anti-Surfactant in III-Nitride Epitaxy –Quantum Dot Formation and Dislocation Termination, Jpn. J. Appl. Phys. 39 (2000), L831.

[16] A.L. Rosa, et al. "Adsorption and incorporation of silicon at GaN(0001) surfaces", Appl. Phys. Lett. 80 (2002), 2008

[17] T. Markurt, et al. Blocking Growth by an Electrically Active Subsurface Layer: The Effect of Si as an Antisurfactant in the Growth of GaN, PRL 110 (2013), 036103.

[18] H. Lahreche, et al. Growth of high-quality GaN by low-pressure metal-organic vapour phase epitaxy (LP-MOVPE) from 3D islands and lateral overgrowth, J. Cryst. Growth 205 (1999), 245.

[19] O. Contreras, et al. Dislocation annihilation by silicon delta-doping in GaN epitaxy on Si, Appl. Phys. Lett. 81 (2002), 4712.

[20] J. Eymery, et al. Process for Catalyst-Free Selective Growth on a Semiconductor Structure. Patent WO2012136665, 2012.

# Chapter 4: Nitride single nanowire and nanowire array photodetectors

## Table of content

---

4.1 GaN NW array ultraviolet photodetectors with a graphene transparent contact .....	91
4.1.1 NWs synthesis .....	93
4.1.2 Device fabrication.....	94
4.1.3 Device characterization.....	96
4.1.4 Conclusion .....	98
4.2 single InGaN/GaN core-shell NW photodetectors .....	99
4.2.1 InGaN/GaN core/shell NWs growth method.....	100
4.2.2 Optical properties.....	101
4.2.3 Fabrication process of single InGaN/GaN core/shell NW photodetectors .....	102
4.2.4 Characterization of photodetectors with a localized metal contact.....	104
4.2.5 Characterization of photodetectors with ITO conformal contact.....	108
4.2.6 Conclusion .....	117
4.3 Flexible vertical InGaN/GaN core-shell NW photodiodes.....	118
4.3.1 Fabrication of the flexible photodetectors .....	118
4.3.2 Device characterization.....	119
4.3.3 Conclusion .....	125

---

Two-dimensional (2D) photodetectors based on III-nitride compounds (Al, In, Ga)N have been intensively studied during the last decade for a large number of applications in astronomy, flame detection, solar monitoring and biophotonics. By varying the Al and In composition, the detection cut-off wavelength can be tuned from UV to visible region. Nevertheless, the performance of 2D photodetectors is degraded by a large number of threading dislocations in the layers. For heterostructure-based devices a strong internal polarization field in c-oriented layers complicates the

device design and shifts the cut-off wavelengths to lower energies. In this context, GaN nanowire (NW) photodetectors have attracted significant interest based on their several advantages such as: absence of threading dislocations, light trapping in NW arrays allowing to increase the light absorption, large surface to volume ratio enhancing the responsivity of the photodetector, and, in addition, absence of internal polarization field for heterostructures grown on the non-polar m-plane facets.

This chapter is dedicated to the study of nitride NW photodetectors. In the first part, I will describe the fabrication and characterization of a GaN ultraviolet photodetector based on a NW array with a graphene transparent top contact. In the second part, I will describe the fabrication of single NW InGaN/GaN detectors operating in the visible to ultraviolet spectral range. The influence of the contact morphology will be investigated by comparing two types of contacts, namely a localized metal contact and an ITO conformal contact, respectively. In the last part, I present a novel technique for fabricating flexible photodetectors based on vertical NW arrays and I will discuss their performances.

## **4.1 GaN NW array ultraviolet photodetectors with a graphene transparent contact**

NWs of wide bandgap materials and in particular GaN NWs have demonstrated a great promise for highly sensitive UV detection. Single GaN NW photodetectors have been studied intensively by many groups<sup>[1-4]</sup>. The mechanism leading to the high sensitivity can be explained by the Fermi-level pinning at the surface inducing a band deformation. Indeed, the electronic bands (conduction band ( $E_C$ ) and valence band ( $E_V$ )) are bent upward at the surface of the NW as shown schematically in Figure 4.1. Under UV illumination, the photogenerated carriers are dissociated by the lateral band bending. The electrons stay in the inner part of the NW, whereas the holes tend to move to the surface. Therefore, under applied bias, the electrons can go around the detection circuit a large number of times staying in the inner NW part before recombining with a hole localized at the wire surface. Calarco et al.<sup>[4]</sup> have found that the NW photodetector responsivity depends on the NW diameter. They showed that the photocurrent remains high for NW diameters exceeding the critical value around 80 to 100 nm (see Figure 4.1 right). Below this critical diameter the NW is completely depleted and the surface barriers

are diminished. In this case, the photocurrent is reduced due to enhanced surface recombination (this case is illustrated in Figure 4.1 left).

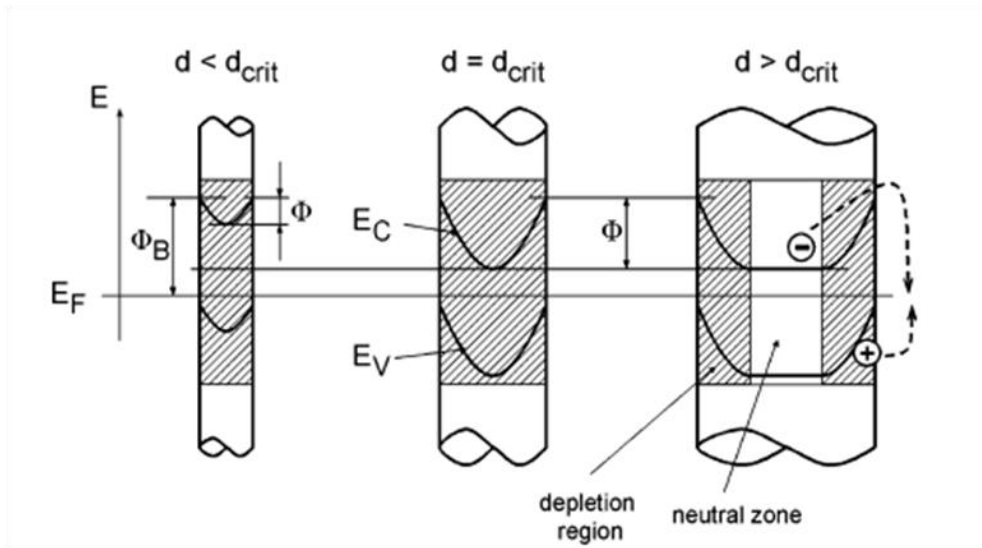


Figure 4.1 Dependence of depletion region (shaded), shape of conduction ( $E_C$ ) and valence band edges ( $E_V$ ), and recombination barrier  $\Phi$  on the nanowire diameter  $d$ . The relative energetic locations of  $E_C$ ,  $E_V$ , and  $E_F$  are not on scale. The detail on the right shows the surface recombination mechanism of the photoexcited carriers. (Reproduce from Ref<sup>[4]</sup>)

The integration of graphene with one dimensional semiconductor nanostructures has recently attracted a strong interest. Graphene has been used as a growth substrate for NWs<sup>[5]</sup> as well as an electrode material<sup>[6]</sup>. The graphene/NW hybrid materials have demonstrated their promise for a broad range of applications, in particular for energy harvesting and storage devices such as solar cells<sup>[7]</sup>, piezogenerators<sup>[8]</sup> or supercapacitor electrodes<sup>[9]</sup>, for light emitting diode<sup>[10]</sup> as well as for gas sensing devices<sup>[11]</sup>. Several NW/graphene photodetectors have been recently reported based on CdS<sup>[12]</sup> and ZnO NWs<sup>[13]</sup>.

The main benefits of a graphene contact are its enhanced transparency and high conductivity. These properties are of particular importance at short wavelengths, since there is a lack of transparent conductive materials in the UV spectral domain. Wide band-gap GaN NWs have demonstrated their capability to produce highly sensitive UV photodetectors in the form of single NW devices<sup>[14]</sup> or NW ensemble detectors using an ITO top contact<sup>[15]</sup>. However, the significant absorption of the ITO top

electrode limits their responsivity in the deep UV range. In this context, it is desirable to replace the ITO by a graphene contact having a better UV transparency. However, no nitride NW/graphene photodetectors have yet been demonstrated in the literature before my PhD work. In this first part of chapter 4, I have focused on the integration of a few-layered graphene contact on the GaN NW ensemble and on the fabrication of UV photodetectors.

### 4.1.1 NWs synthesis

The GaN NWs were grown on a  $n^+$ -doped Si (111) substrate by plasma-assisted molecular beam epitaxy (PAMBE). Ga and Si were evaporated using conventional effusion cells, and active nitrogen was generated with a radio frequency plasma source. Prior to the PAMBE growth, the Si substrate was cleaned by acetone, isopropanol and de-ionized water with ultrasonic bath for 5 min each to remove residual organic contaminations on the surface. In addition, HF:H<sub>2</sub>O = 1:10 solution was used for 5 min to remove the native oxide. The MBE growth began with thermal cleaning of the Si substrate at 850°C. NWs were grown at a substrate temperature of 780°C under nitrogen rich conditions for 1.5 h. Si doping was introduced during the NW growth at a nominal concentration of  $1-5 \times 10^{17} \text{ cm}^{-3}$  (as estimated from calibrations on 2D layers). This procedure results in a dense ensemble of NWs with an average length of about  $1 \pm 0.2 \text{ }\mu\text{m}$  and a diameter of  $100 \pm 50 \text{ nm}$ . Because of the high density, some NWs coalesce during the growth, forming irregular structures with diameters going up to 400 nm. An SEM image illustrating the NW morphology is shown in the inset of figure 4.2.

I have first studied the optical properties of the as-grown NWs by PL spectroscopy. The PL spectrum of the NW ensemble is shown in figure 4.2. The spectrum is peaked at 3.415 eV with a FWHM of 128 meV. The slight asymmetry on the low energy side may be attributed to transitions related to donor impurities or defects resulting from the NW coalescence.

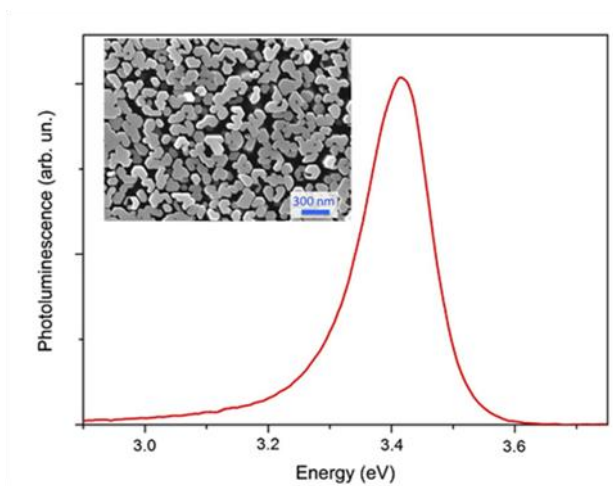


Figure 4.2 Room temperature PL spectrum of GaN NWs. Inset Top-view SEM image of the as-grown NWs.

#### 4.1.2 Device fabrication

Prior to the graphene transfer, the NW bottom part was first encapsulated into a thin layer (nominal thickness of 50 nm on a flat surface) of HSQ flowable oxide, which was transformed into  $\text{SiO}_x$  by thermal annealing. The excess of HSQ was etched from the NW tops using RIE with a  $\text{CF}_3$  chemistry. The NW ensemble was cleaned in an oxygen plasma to remove any organic residues, then the surface oxide was removed by wet etching in  $\text{HCl} : \text{H}_2\text{O}$  (1:3) for 60 s and the sample was rinsed in deionized water. The graphene transfer was performed immediately after this cleaning procedure.

Graphene sheets containing up to 4 monolayers were grown by CVD method on  $\text{Si}/\text{SiO}_2/\text{Ni}$  substrates (commercially available layers from “Graphene Supermarket” were used). The Ni layer was wet-etched by  $\text{FeCl}_3$  saturated aqueous solution, the floating graphene sheet was transferred to a clean deionized water and then deposited on top of the NW ensemble. The size of the graphene sheet was  $1 \text{ cm}^2$ . Transfer tests using a different transfer medium (isopropyl alcohol instead of deionized water) have also been performed, however no significant difference in graphene adhesion and in final morphology has been observed. Different procedures to remove water residue from the graphene/NW interface have been tested. Drying under vacuum as well as drying in nitrogen atmosphere under an external pressure resulted in graphene fracturing. Natural drying of the NW/graphene samples in the

ambient atmosphere resulted in the best quality from the viewpoint of the interface morphology and graphene adhesion. SEM images of the graphene film on the NW ensemble are shown in figure 4.3. A continuous graphene film was achieved except for some localized defects marked with white arrows in figure 4.3 (a). As shown in figure 4.3, these defects correspond to the tearing of the graphene layer by certain NWs with a length exceeding by more than 100 nm the average NW length. However, these defects were rarely observed. A more frequent situation corresponds to the graphene suspension as illustrated in figures 4.3 (b) and 4.3 (d). It should be noted that defect-free graphene film can potentially be achieved if the NW height is homogeneous as in the case of etched GaN nanopillars.

The NW ensemble with a top graphene film was further used to fabricate a photodetector. Ti/Al/Ti/Au open contacts were defined on the graphene sheet by optical lithography, e-beam metal evaporation, and lift-off. SEM observations after processing demonstrate that these technological steps preserve the graphene integrity. I removed the graphene layer between the metal contacts using optical lithography and RIE etching in oxygen plasma for 3 min. A second Ti/Al/Ti/Au surrounding contact was deposited directly on the NW tops. The final device is composed of  $300 \times 300 \mu\text{m}^2$  graphene squares with two open metal contacts: one on top and another outside the graphene sheet, as schematically illustrated in the inset of figure 4.4.

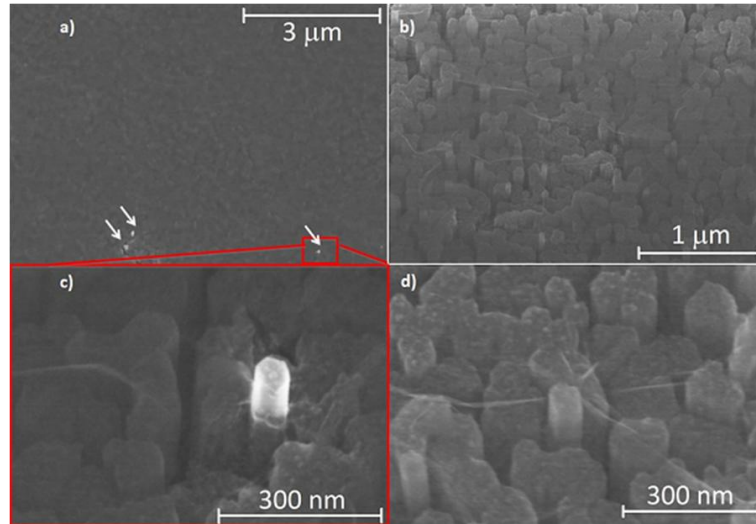


Figure 4.3 SEM images of the graphene film on the NW ensemble (the observation axis is tilted by 30 ° with respect to the top-view observation) (a) Large area image showing several defects marked by white arrows; (b) image at higher magnification showing graphene ripples; (c) zoom on a defect region; (d) high magnification image illustrating a graphene suspended blister. Image (a) and images (b)–(d) were collected at 5 kV and 30 kV acceleration voltage, respectively.

### 4.1.3 Device characterization

To probe the electrical connection between the graphene layer and the NWs, the I-V characteristics were measured between the central contact and the surrounding contact of the micro-detector under study. For this configuration, the current flows through the graphene/NW contact, the NWs, the  $n^+$ -doped Si substrate, then again through the NWs and the NW/metal contact. The resulting I-V curve shown in figure 4.4 exhibits a non-linear behavior with a current of  $4.3 \times 10^{-5}$  A at 1 V. I-V curve measured between the surrounding contacts of two neighboring micro-detectors (not shown) exhibits an almost ohmic behavior and an order of magnitude higher current. Therefore, we assume that the increase in resistance and the observed non-linear behavior are mainly due to the graphene-to-NW contact. In the 2D case, graphene on lightly Si-doped GaN ( $10^{16}$  cm<sup>3</sup>) was reported to form a Schottky contact<sup>[16]</sup>, whereas a low resistivity contact was reported for highly n-doped GaN layers<sup>[17]</sup>. The intermediate doping level of the presently studied GaN NWs may explain the observed non-linear

behavior.

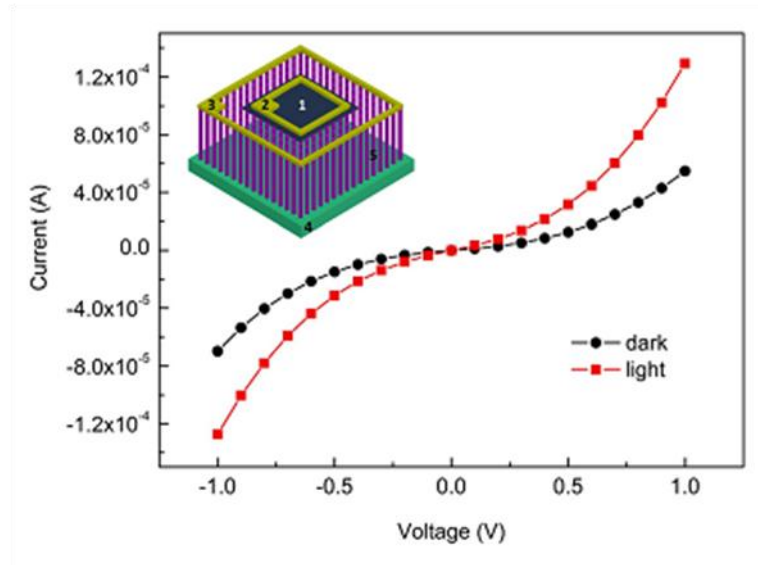


Figure 4.4. Current-voltage characteristics of the device in the dark and under UV illumination. Inset shows a device schematic with the following notations: 1–graphene sheet, 2 and 3–metal contacts, 4– $n^+$ -doped Si (111) substrate, 5–GaN NWs.

To further elucidate the photocurrent origin, the spectral response of the detector was measured at room temperature using a tunable visible-UV light source, consisting of a Xe lamp coupled with a Jobin Yvon Triax 180 spectrometer. The light was mechanically chopped at 4 Hz and the signal was demodulated using a lock-in detector. A typical photocurrent spectrum is displayed in the inset of figure 4.5. The spectrum is normalized by the optical system response. The signal rapidly increases at energies higher than 3.2 eV and exhibits a peak at 3.42 eV close to the GaN band-gap, demonstrating that the main contribution to the photocurrent originates from the GaN NWs. A weak sub-band-gap signal is observed down to 2.7 eV, which is likely to arise from defects in the GaN NWs. Above the GaN band-gap the photocurrent does not show any high-energy cut-off. The high signal in the UV range demonstrates that the top graphene electrode has a good transparency at least up to 4.15 eV contrary to ITO, which presents a pronounced absorption at energies larger than 3.88 eV.

The power dependence of the responsivity has been studied by varying the incident power by more

than four orders of magnitude (Figure 4.5). The detector responsivity is defined as :

$$R = \frac{I_{ph}}{P_{opt}} \quad (4.2)$$

where  $I_{ph}$  is the photocurrent and  $P_{opt}$  is the incident optical power. At low excitation the photocurrent scales linearly with the incident power density corresponding to a constant responsivity of about 25 A/W at 1 V bias. However, at high excitation the responsivity drastically decreases. It should be noted that a sub-linear power dependence of the photocurrent has been reported in single GaN NW photoconductors. It is inherent to the photoconduction mechanism in GaN NWs, which implies hole trapping on the NW surface and screening of the radial band bending.

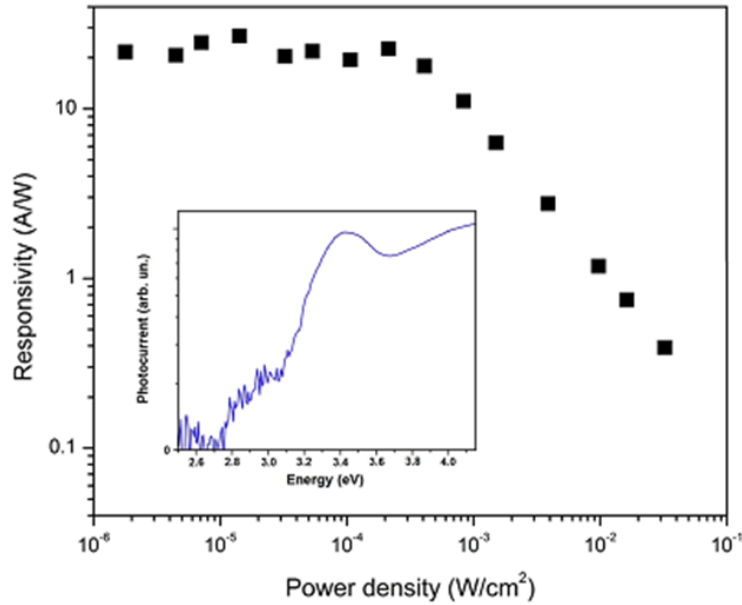


Figure 4.5 Dependence of the room-temperature responsivity at 1 V bias on the incident power density. The inset shows the photocurrent spectrum of the detector in logarithmic scale.

#### 4.1.4 Conclusion

In conclusion, an ultraviolet photodetector using graphene as a top transparent contact is demonstrated. The detector presents a responsivity of 25 A/W at 1 V bias at 357 nm at low excitation power. The

photocurrent spectrum shows that the detector response is mainly related to GaN nanowire photoconductivity and attests the good transparency of the graphene electrode at least up to 4.15 eV, i.e., in the spectral region where ITO already presents a strong absorption.

## 4.2 Single InGaN/GaN core-shell NW photodetectors

InGaN/GaN two-dimensional quantum well (QW) superlattices have been intensively studied as materials for visible and ultraviolet light emission and detection<sup>[18][19]</sup>. They have also been investigated in view of photovoltaic conversion applications. Previously, our group has reported single InGaN/GaN core-shell NWs photodetectors. For example, in 2011, n-i-n single-wire photodetector based on InGaN/GaN radial QWs has been investigated by A. Bugallo de Luna (see figure 4.6 (a))<sup>[20]</sup>. The results show that the photoconductive gain is as high as  $2 \times 10^3$  and confirm that the device operates as a radial n-i-n junction. In 2014, InGaN/GaN p-n junction core-shell NWs have been used in a photonic platform (see figure 4.6 (b))<sup>[21]</sup>. The photodiode detects the LED on/off switching and shows a reasonably short transition time ( $< 0.5$  s) between the on and off states. Despite these investigations, the detection properties of single core/shell p-n InGaN/GaN NW photodiodes remain today poorly explored.

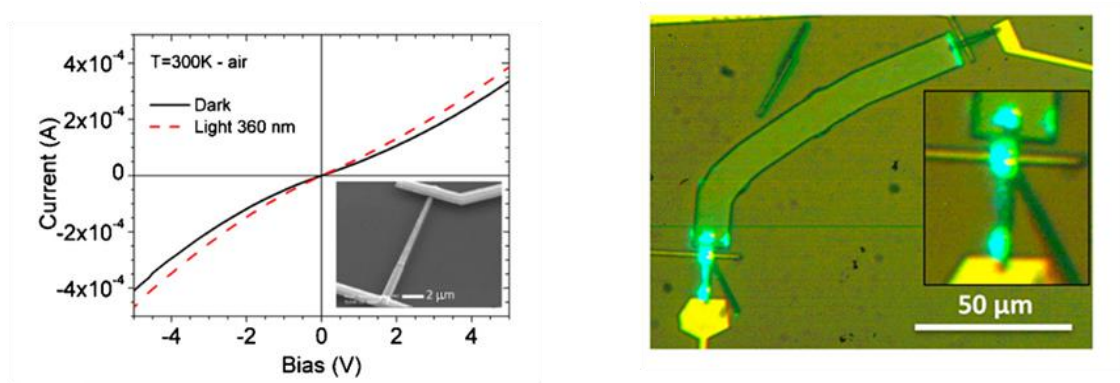


Figure 4.6: (a) n-i-n single-wire photodetector based on InGaN/GaN radial QWs<sup>[20]</sup>, ( b ) InGaN/GaN p-n junction core-shell NWs photonic platform<sup>[21]</sup>.

In this part, I fabricate single InGaN/GaN core-shell NW photodetectors with two different p type contacts, which are namely a localized metal contact (named photodetector I) and a conformal ITO

contact (named photdetector II). The impact of the contact morphology is investigated.

#### 4.2.1 InGaN/GaN core/shell NWs growth method

The growth of InGaN/GaN NWs was performed by A. Messanvi under supervision of J. Eymery and C. Durand at CEA/INAC. The N-polar GaN wires were grown by MOVPE on a c-sapphire substrate using in-situ  $\text{SiN}_x$  thin film pre-deposition<sup>[22]</sup>. The bottom wire part ( $\sim 10 \mu\text{m}$  long) was heavily  $n^+$ -doped. Then a non-intentionally doped GaN segment ( $\sim 10\text{-}15 \mu\text{m}$  long, residual  $n$ -doping  $\sim 10^{18} \text{cm}^{-3}$ ) was deposited. The upper part of the wires was coated with 30 InGaN/GaN radial QWs (6 nm/24 nm) along the nonpolar  $m$ -plane facets and then overgrown with a  $p$ -doped GaN shell as reported in<sup>[23]</sup>. The targeted indium composition in the QWs is  $\sim 18\%$ . I note that the QWs cover both the lateral  $m$ -plane facets and the top  $c$ -plane facet forming families with different optical properties. The NW morphology is illustrated in Figure 4.7 (a). The average wire length is  $20\text{-}25 \mu\text{m}$  and the diameter is  $1\text{-}2 \mu\text{m}$ . A cross-section schematic is shown in Figure 4.7 (b). The four different colors (red, blue, grey, and brown) represent four different regions, i.e. the  $p$ -type GaN, the 30-period InGaN/GaN QWs, the non-intentionally  $n$ -doped GaN, and the heavily  $n^+$ -doped GaN, respectively.

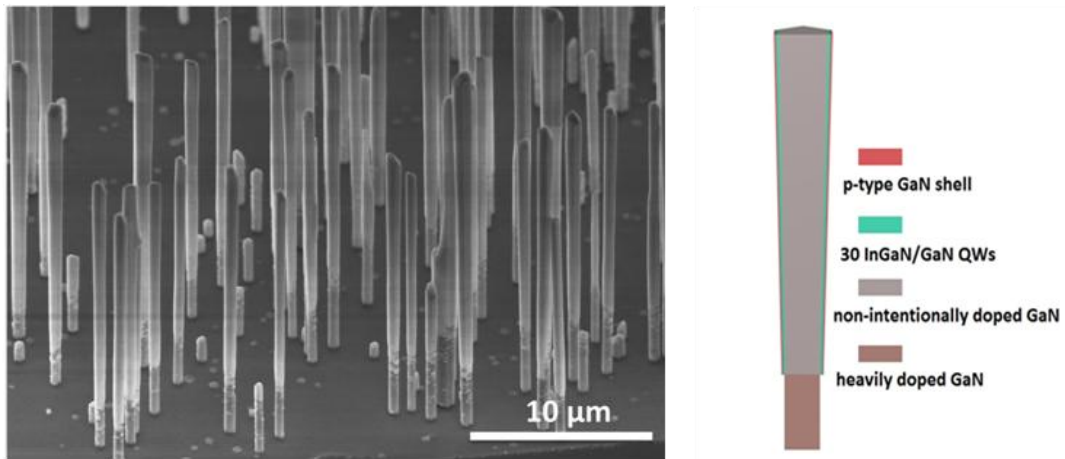


Figure 4.7: (a)  $45^\circ$  tilted SEM image of self-assembled InGaN/GaN NWs. (b) cross-section schematic of a single NW.

## 4.2.2 Optical properties

I have investigated the optical properties of the NWs by  $\mu$ PL spectroscopy. The  $\mu$ PL measurement procedure is the same as I have described in the previous chapters. Figure 4.8 shows a typical  $\mu$ PL spectrum of a single NW. The spectrum presents two distinct peaks. The main peak at 3.07 eV (403 nm) is attributed to the radial QWs on the m-plane facets as described in detail in <sup>[24]</sup>. The shoulder observed at around 2.8 eV (443 nm) corresponds to the photoluminescence of the axial QWs at the top part of the NW. This peak is red-shifted with respect to the radial QWs because of the internal electric field on the c-plane, but also because of a higher In content in the axial QW.

The inset presents the band profile of GaN p-n junction with 30 MQWs. Zero of the energy scale corresponds to the Fermi level. The built-in field of the p-n junction is homogeneously distributed in the QWs. The first QW at the n-side is below the Fermi level and is therefore filled with electrons. Other QWs are empty without external illumination.

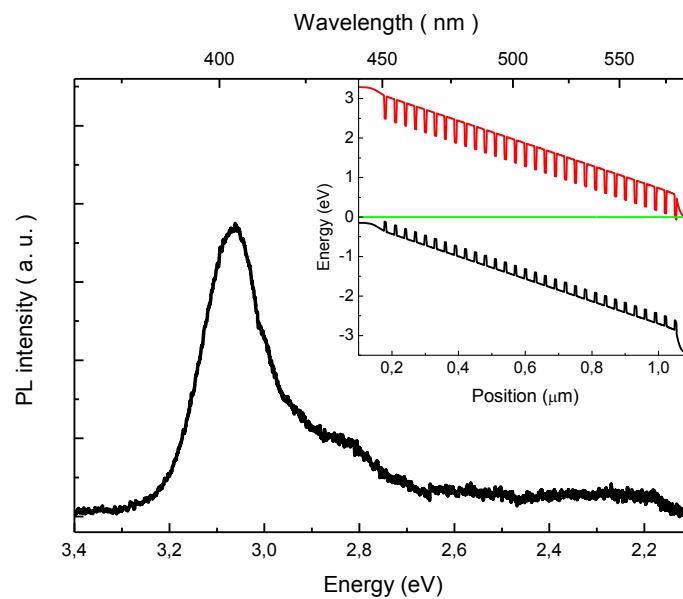


Figure 4.8: typical PL spectrum of a single NW. The band profile of 30 InGaN/GaN MQWs on the m-plane is shown in the inset.

To further evaluate the bandgap of the InGaN QWs and test the electrical behavior of the NW, the EL

spectrum of a contacted NW at 4 V is presented in the figure 4.9. The main luminescence peak is centered at 3.14 eV (394 nm) with a FWHM of 0.17 eV. The blue shift compared with the PL spectrum is due to the In content fluctuation from wire to wire. The shoulder peak is observed at 2.6 eV. Similar to the PL experiments, it is ascribed to the axial QWs, which contain more In and exhibit QCSE.

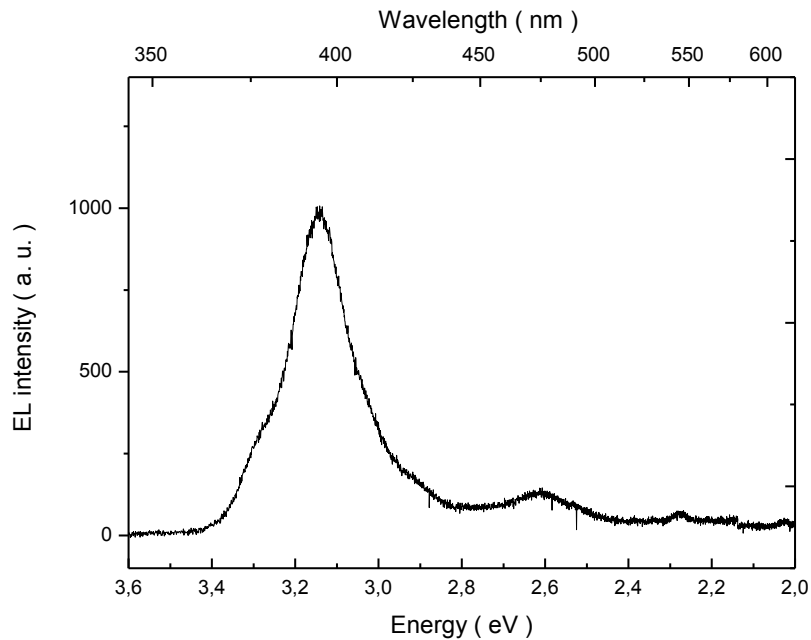


Figure 4.9: single nanowire EL spectrum at 4 V.

### 4.2.3 Fabrication process of single InGaN/GaN core/shell NW photodetectors

To fabricate single wire photodetectors, I have detached the NWs from their native substrate by ultra-sonic cutting and dispersed them on a SiO<sub>2</sub>/Si substrate. To provide mechanical support for the contacts, the NWs were then encapsulated in HSQ transformed into SiO<sub>x</sub> after thermal annealing for 1 hour at 400 °C. The excess of HSQ was etched in a diluted HF solution (HF:H<sub>2</sub>O = 1:200 volume) to expose the lateral NW facets for contacting. The contact fabrication process for single NW photodetectors followed different schemes. For the photodetector with a localized contact (type D), metal pad on the p-GaN shell was defined by optical lithography. A Ni /Au (10 nm / 150 nm) layer

was deposited followed by an annealing at 500 °C in ambient atmosphere for 5 min to favor the formation of an ohmic contact on p-type GaN. The second contact on the n+-type GaN core was also defined by optical lithography followed by a Ti/Al/Ti/Au (10/20/10/200 nm) metallization. Figure 4.10 (a) shows an SEM image of a photodetector of type I. The conformal contact (type II) was achieved by depositing an ITO layer after e-beam lithography. To improve the contact conductivity, ITO was annealed in a furnace at 400 °C for 10 min. A second e-beam lithography was performed to define the metal contact on the n+-type GaN core. A Ti/Al/Ti/Au (10/20/10/200 nm) metal contact was deposited by e-beam evaporation at a tilted angle of 45 ° for a good coverage of the NW facets. Figure 4.10 (b) presents SEM image of a photodetector of type II.

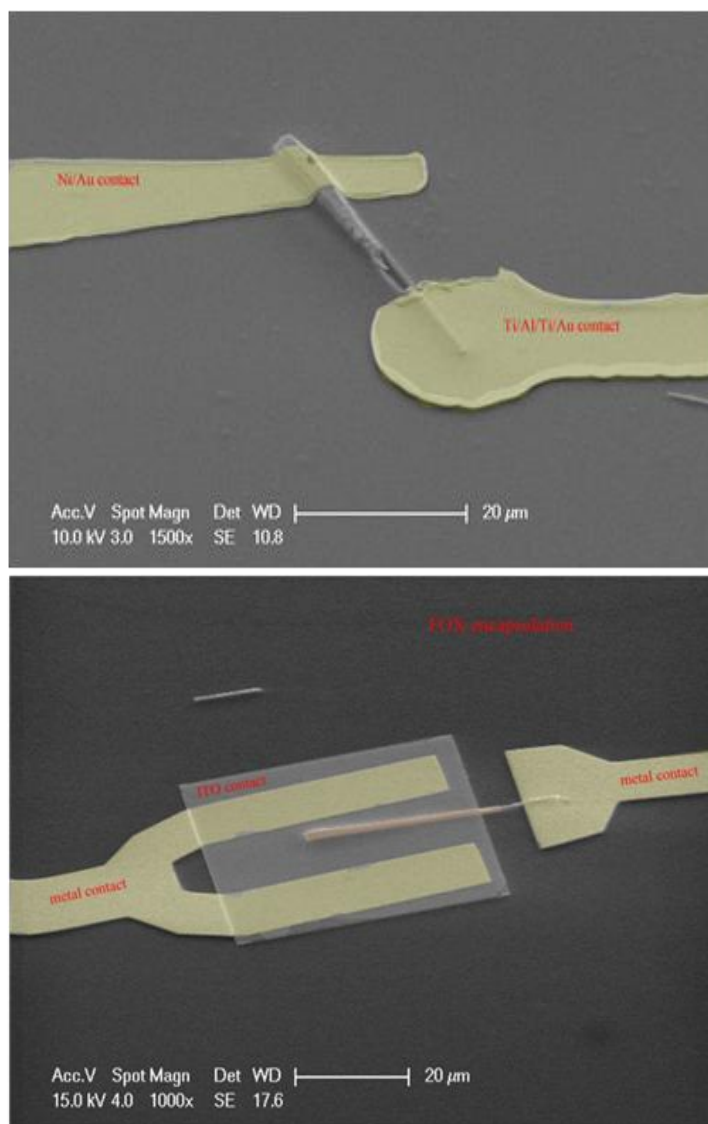


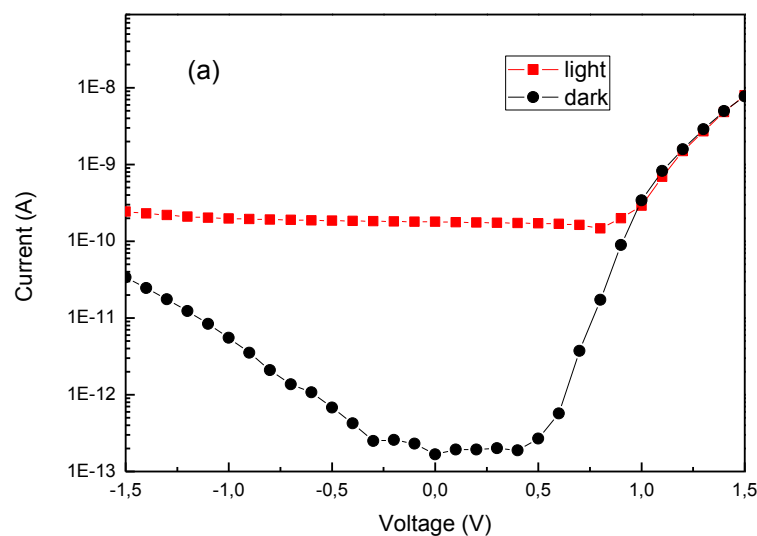
Figure 4.10 (a) SEM picture of a processed photodetector of type I and (b) SEM image of a photodetector of type II.

#### 4.2.4 Characterization of photodetectors with a localized metal contact

Figure 4.11 (a) presents the I-V characteristics (in logarithmic scale) of a photodetector of type I in the dark and under illumination at  $\lambda=370$  nm by a tunable light source composed of a Xenon lamp coupled with a monochromator. In the dark, the I-V curve shows a typical rectifying behavior with no significant current leakage under reverse bias (the dark current is below  $10^{-11}$  A at -1 V bias). The

non-zero dark current at zero bias (below 1 pA) is an artifact due to the noise limit of our electrical detection system. Under illumination at  $\lambda=370$  nm, the photodetector exhibits a strong photocurrent. The induced current under zero bias reaches  $\sim 0.2$  nA. As expected for a p-i-n junction photodiode, the current signal does not significantly change under reverse bias. Indeed, for biases from 0 to -1.5 V the current only slightly increases between 0.2 and 0.24 nA. Under forward bias, the current under illumination first slightly decreases, changes sign and then increases following the dark current behavior of a p-i-n junction under forward bias.

The I-V characteristics for higher forward current levels (up to 50 nA) are shown in Figure 4.11 (b) (in linear scale) under illumination and in the dark. It is seen that for forward biases above 1.5 V the slope of the I-V curve under illumination is slightly steeper than that in the dark. One likely explanation is that the access resistance of the p-GaN shell changes under illumination. It should be noted that NW photodetectors are often characterized by strong photoconductive effects as a consequence of the surface Fermi level pinning, thus leading to a very large photocurrent gain<sup>31</sup>. NW photoconductors can even present persistent photoconductivity. However, as seen in figure 4.11 (b), in the presently-investigated case of a radial p-n junction these negative effects are minimized thanks to the core-shell geometry. Indeed, the dark and illuminated I-V curves under forward bias are almost identical, whereas a strong current increase is expected for a NW photoconductor.



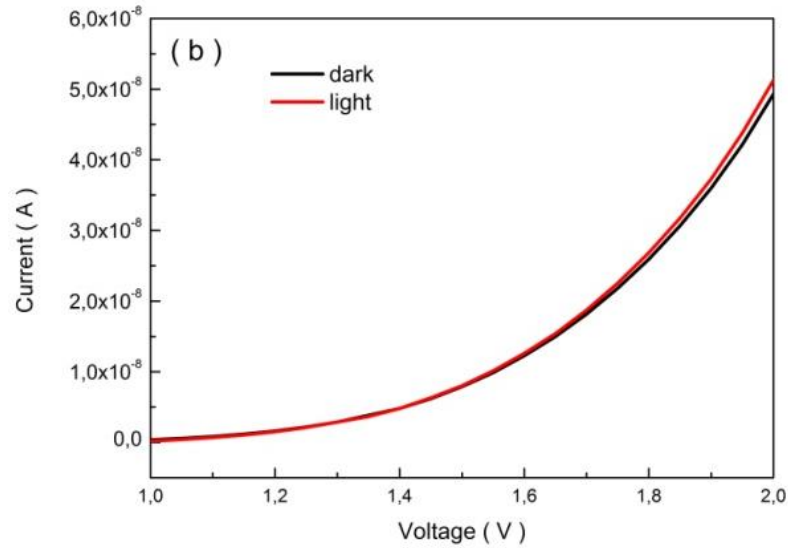


Figure 4.11 (a) I-V curve of photodetector of type I in the dark and under illumination. (b) I-V curve for larger forward biases showing only a weak current modification under illumination.

In order to investigate the operation speed of the photodetector of type I, the time dependent photocurrent transient measurements were performed under zero bias. The NW detector was illuminated with square light pulses with different wavelengths using Xe lamp coupled with a monochromator. As shown in figure 4.12, the photodetector presents a response to wavelengths shorter than 430 nm (photocurrent = 4.7 pA), i.e. below GaN bandgap, corresponding to the absorption in the InGaN/GaN radial QWs. The response increases at shorter wavelengths. The rise and decay switching times for all illumination wavelengths are below the time resolution of our measurement system (~0.1 sec). We note that this behavior is different with respect to NW photoconductors for which very slow signal transients are observed<sup>[22]</sup>.

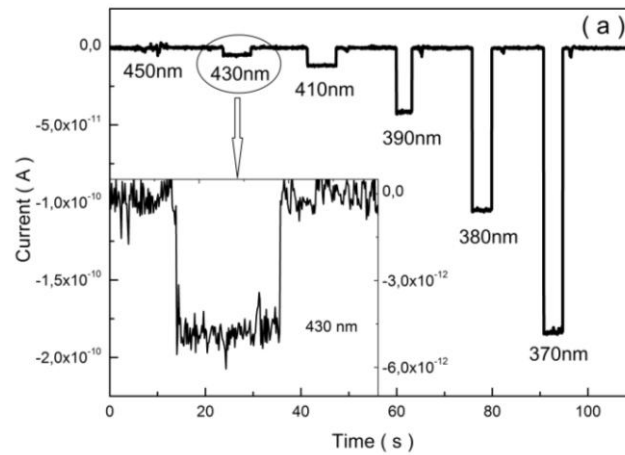


Figure 4.12 Time-dependent photocurrent for on/off illumination cycles at different wavelengths from 450 to 370 nm. The inset shows a close-up on one cycle under illumination at  $\lambda = 430$  nm corresponding to the QW absorption.

To better analyze the spectral dependence of the detector response, photocurrent spectra of a single NW device were measured at room temperature using the same wavelength tunable Xenon light source described previously. The photocurrent spectrum under zero bias of a typical device in the visible-to-UV spectral range is reported in figure 4.13 (in a logarithmic scale). The calibration of the light source output intensity was done using a commercial calibrated photodiode sensor and the detector spectrum was normalized by the set-up spectral response. As seen in figure 4.13, the photoresponse appears at energies around 2.85 eV (435 nm), i.e. below the GaN bandgap. This response is attributed to the absorption in the QWs and the subsequent extraction of the electron-hole pairs from the QWs by the electric field of the radial p-i-n junction. However, the responsivity in the visible range is rather weak ( $\sim 0.015$  A/W at  $\lambda=442$  nm). Between 2.85 eV and 3.36 eV (370 nm), the photocurrent rapidly increases and reaches its maximum of 0.17 A/W at 3.36 eV ( $\sim 370$  nm). This increase can be understood as a consequence of the inhomogeneous In composition in the QWs. Indeed, the regions with a lower In content contribute to the photocurrent at shorter wavelengths. In addition, the carrier extraction from the shallow In poor QW regions is more efficient than that from the deep In-rich QW parts. The signal remains almost constant until 3.54 eV (350 nm) and then

decreases by 35-40% toward the UV range (300 nm). This decrease for wavelengths shorter than the GaN band-gap is due to the loss of photoexcited carriers absorbed in the p-GaN shell region. Indeed, these carriers can recombine on surface states instead of diffusing to the p-n junction field region and thus they do not contribute to the photocurrent.

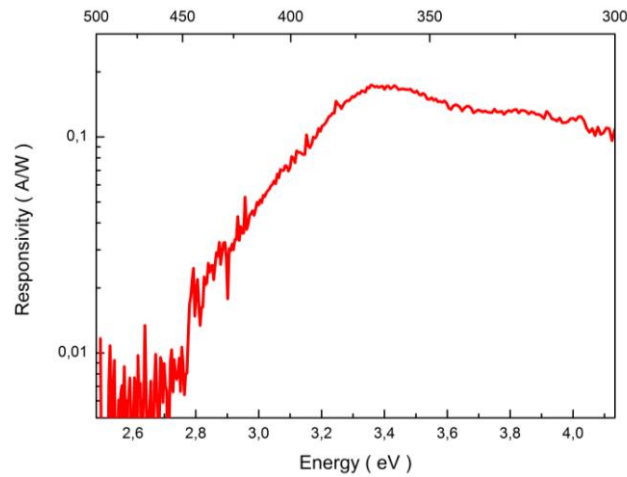


Figure 4.13: Room temperature photocurrent spectrum of the photodetector of type I.

#### 4.2.5 Characterization of photodetectors with AN ITO conformal contact

In the previous section, we have focused on InGaN/GaN core/shell NWs with a localized metal contact on the p GaN shell. I now focus on single NW photodiodes having the same internal structure as in the previous section, but having a conformal ITO contact covering almost the entire core/shell active region and discuss the influence of the contact morphology.

I have measured the I-V characteristics of a photodetector of type II in the dark and under illumination. The I-V characteristics of the photodetector in logarithmic scale are presented in figure 4.14 (a). The corresponding I-V curve in linear scale is shown in figure 4.14 (b). Similar to the previously-described detectors with a partial metal contact, the device in the dark shows a typical rectifying behavior with a very small reverse leakage current, which is below  $10^{-11}$  A at -1 V bias (as already mentioned, 1 pA corresponds to the sensitivity limit of our experimental set-up). The current rapidly increases for the forward bias. The dark current reaches 4 nA at 2.5 V. Under illumination with  $\lambda=370$  nm, the

photocurrent increases significantly at zero bias, and the short circuit current reaches around 0.2 nA. Under reverse bias, the photocurrent does not significantly change from 0 to -1.5 V. The current remains between 0.2 and 0.28 nA. After -1.5 V, the photocurrent increases to 0.58 nA. It should be mentioned that the I-V behavior follows a similar trend in comparison with the partial metal contact NW photodetector. Under forward bias, the NW photodetector with conformal contact shows a different behavior. The current under illumination initially decreases (due to the current induced by the p-i-n junction), but then rapidly increases and surpasses the dark current. The cross of the dark and illuminated I-V curves is noticed at 0.7 V. Beyond 0.7 V, the current under illuminating grows much faster than the dark current. At 2.5 V, the photocurrent reaches 22 nA which is five times larger than the dark current (4 nA).

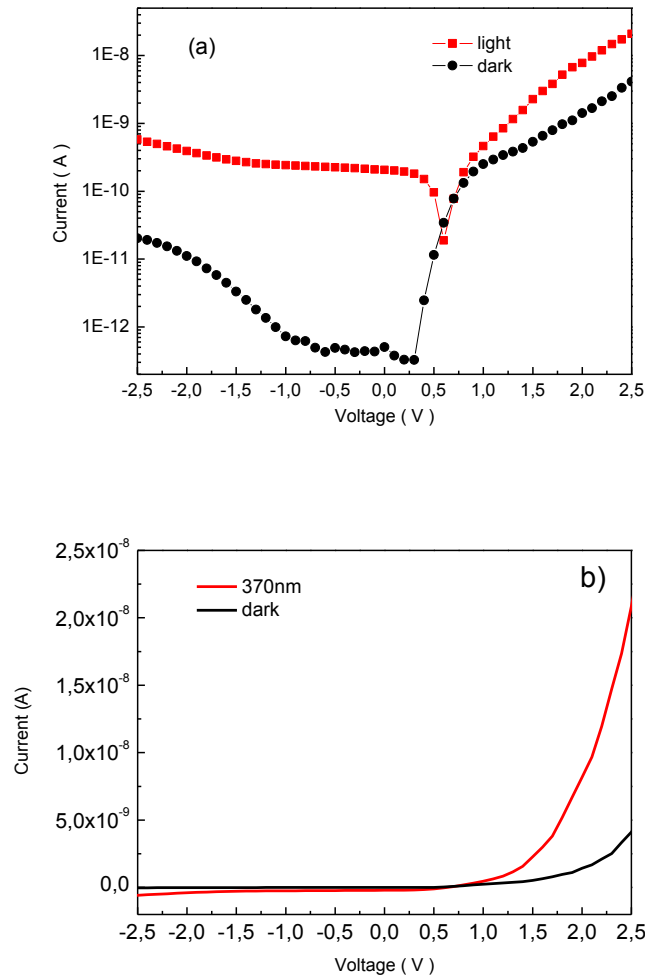


Figure 4.14: I-V characteristics in the dark and under illumination in logarithmic scale a) and in linear

scale b).

Photocurrent spectra of photodetector of type II were measured at room temperature in short-circuit conditions. The measurement and calibrations equipments are the same as I have described in the previous section. The RT photocurrent spectrum in log scale is shown in figure 4.15. The photoresponse appears at wavelengths shorter than 2.95 eV (420 nm). As for the detector of type I, the photocurrent response below the GaN bandgap is attributed to the absorption of the InGaN QWs. The photocurrent signal increases rapidly above 3 eV indicating that photo induced electron-hole pairs are generated in the QWs and separated by the radial p-n junction. The photo responsivity reaches its maximum value of 0.14 A/W at 3.35 eV (which is similar to the value 0.17 A/W for detector of type I). Beyond 3.4 eV, the decrease of the photocurrent (0.063 A/W at 4.1 eV) is due to the recombination on the surface states of the p-GaN shell and possible to UV absorption of the ITO. The photocurrent at -1 V follows a similar evolution. Thanks to the increase of the internal electrical field by the externally applied bias, the photocurrent rises faster and a higher photo responsivity of 0.157 A/W at the peak position is reached under reverse bias.

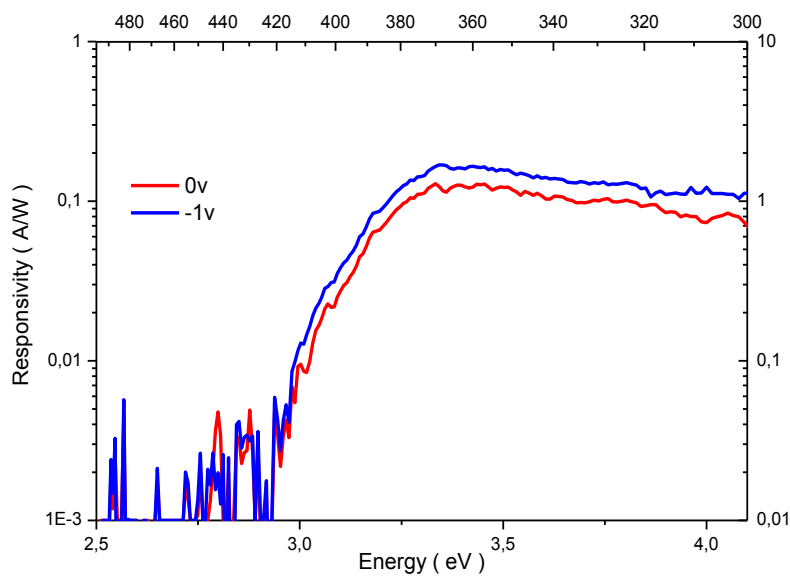


Figure 4.15: photocurrent spectra at 0 V and -1 V, respectively.

The photodetector response to square light pulses (370 nm) under zero bias is shown in Fig 4.16. The photocurrent increases rapidly to 0.2 nA. The switching time is below 0.1 s.

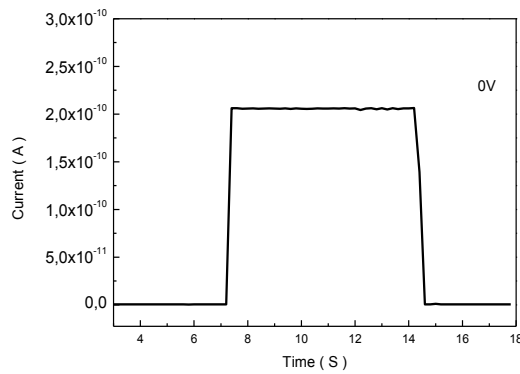


Figure 4.16 photoresponse under a single light square pulse without bias.

The response to single square light pulses (370 nm) is further studied under the reverse and forward biases. At -1 V, the photocurrent increases from 0.2 nA to 0.25 nA as shown in figure 4.17 (a). The intensity reproduces the pulse shape which is constant (no slow phenomena are observed). The signal increase under bias is attributed to the improved extraction from the QWs due to the broadening of the space-charge region in the p-n junction. In figure 4.17 (b) showing the current transient under -2 V applied bias, the shape is different. A rapid increase to 0.39 nA is first observed and then a slow signal evolution reaching 0.42 nA after 10 s is seen under illumination. This slow evolution becomes even stronger varying from 0.8 nA to 9.3 nA at -3 V as shown in figure 4.17 (c). The existence of fast and slow response components indicates that two carrier transportation mechanisms are present in the device: the fast component can be understood as originating from photo carrier separation by the internal electrical field and the slow component is attributed to the slow carrier trapping/detrapping on the surface states.

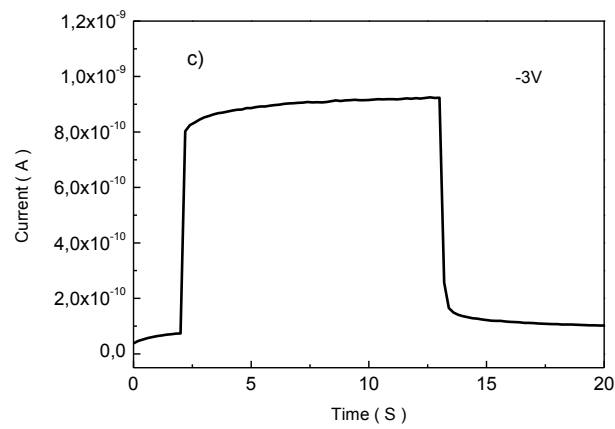
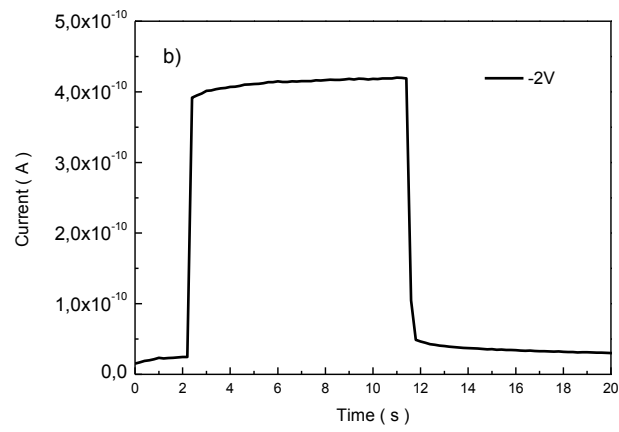
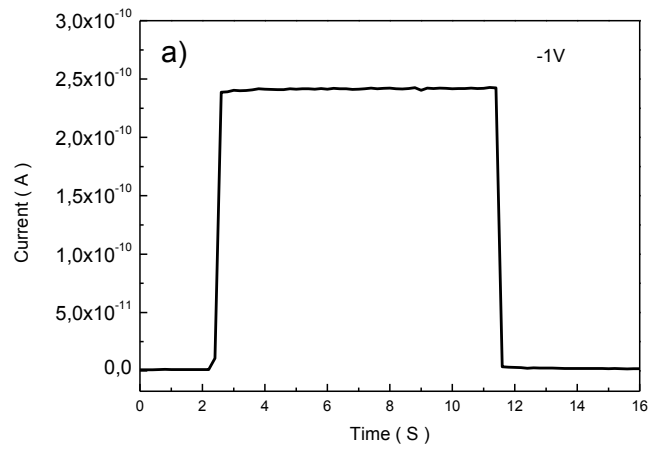
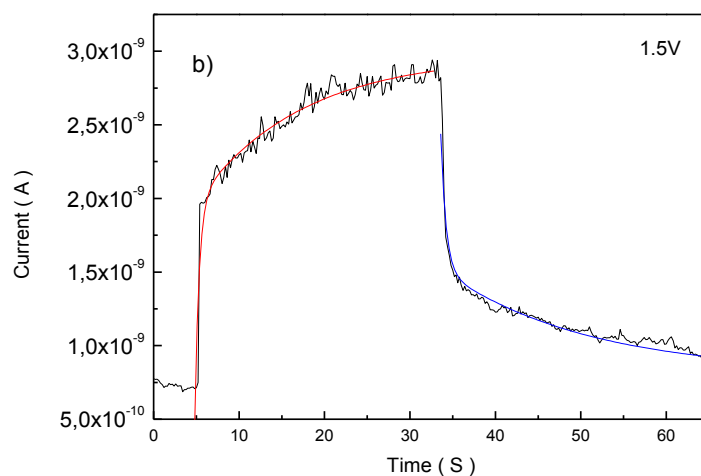
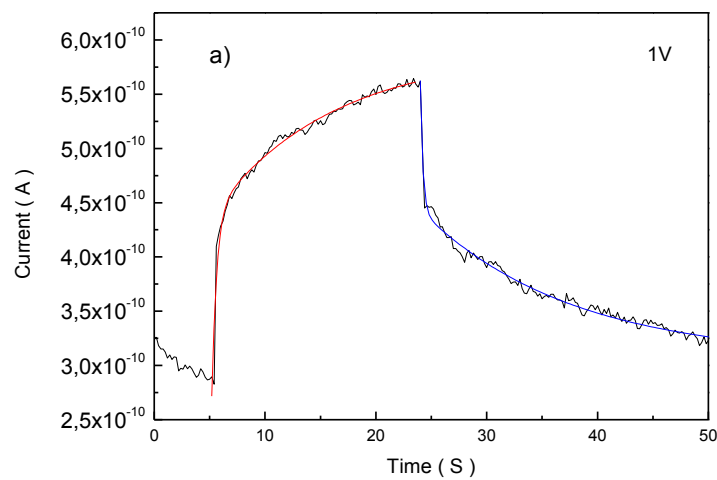


Figure 4.17: (a), (b) and (c) show the current transients under a single light pulse at -1 V, -2 V and -3 V, respectively.

When the bias is switched to the forward one, the photocurrent rise and decay time constants are much

longer compared to the reverse biased devices, indicating that the carrier trapping on surface states becomes dominant. Time dependent photocurrent transients at 1 V, 1.5 V and 2 V are presented in Figure 4.18 (a), (b) and (c), respectively. The build-up time as well as the relaxation time of all these traces follows a bi-exponential law, with fitting parameters extracted and shown in table 4.1 and table 4.2. As for the build-up time, constant  $t_1$  does not show a significant change (it lies between 0.43 s and 0.5 s) with increasing voltage, while  $t_2$  grows steadily from 10.8 s (1 V) to 14.9 s (2 V). Regarding the relaxation time, the constants  $t_1$  and  $t_2$  show a remarkable change together with voltage variation: at 1 V,  $t_1$  and  $t_2$  are 0.23 s and 13.4 s, respectively, and these constants raise to 1.17 s and 20.5 s, respectively, at 2 V.



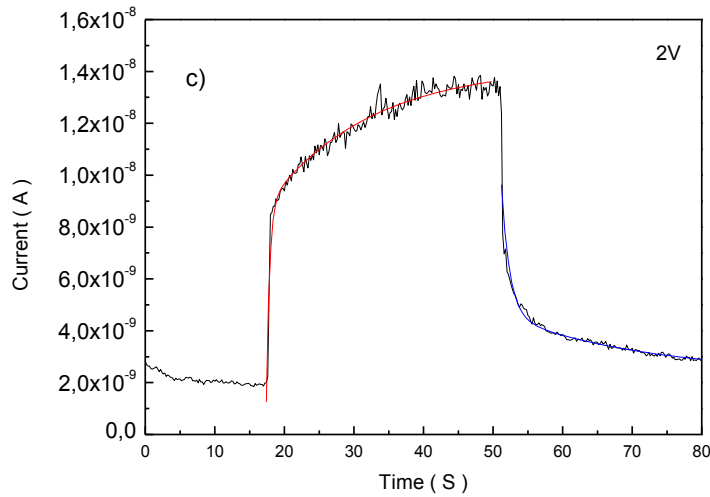


Figure 4.18: (a), (b) and (c) show the current trace in response to a single light pulse at 1 V, 1.5 V and 2 V, respectively.

Build-up time	1 V	1.5 V	2 V
T1	0.43 s	0.5 s	0.46 s
T2	10.8 s	12.3 s	14.9 s

Table 4.1: the build-up time for a single NW photodetector at 1 V, 1.5 V and 2 V, respectively

Relaxation time	1 V	1.5 V	2 V
T1	0.23 s	0.6 s	1.17 s
T2	13.4 s	16.9 s	20.5 s

Table 4.2 the relaxation time for a single NW photodetector at 1 V, 1.5 V and 2 V, respectively

To further investigate the time response of the detector, a wavelength tunable incident light source with 4 Hz and 10 Hz chopping frequency is applied on the photodetector with a conformal ITO contact, meanwhile the time dependent photocurrent is recorded at zero bias and a 1 V bias. Three wavelengths were used which are 370 nm, 390 nm, and 410 nm. At zero bias, as shown in figure 4.19 (a) and (b), the time response stays fast and repetitive with on/off cycles at 4 Hz as well as at 10 Hz with the

variation of wavelength. The photocurrent intensity is still detectable at 410 nm (20 pA which is 2 orders of magnitude larger than the dark current). At 1 V, however, the response becomes slower (signal decrease is observed from 4 Hz to 10 Hz as shown in figure 4.19 (c) and (d)). The photocurrent is hardly detectable at 410 nm. The details of the photoresponse at 370 nm are shown in the inset of figure 4.19 (c) and figure 4.19 (d). The comparison of the chopped signal under 0 V and 1 V confirms the different carrier transportation paths in NW.

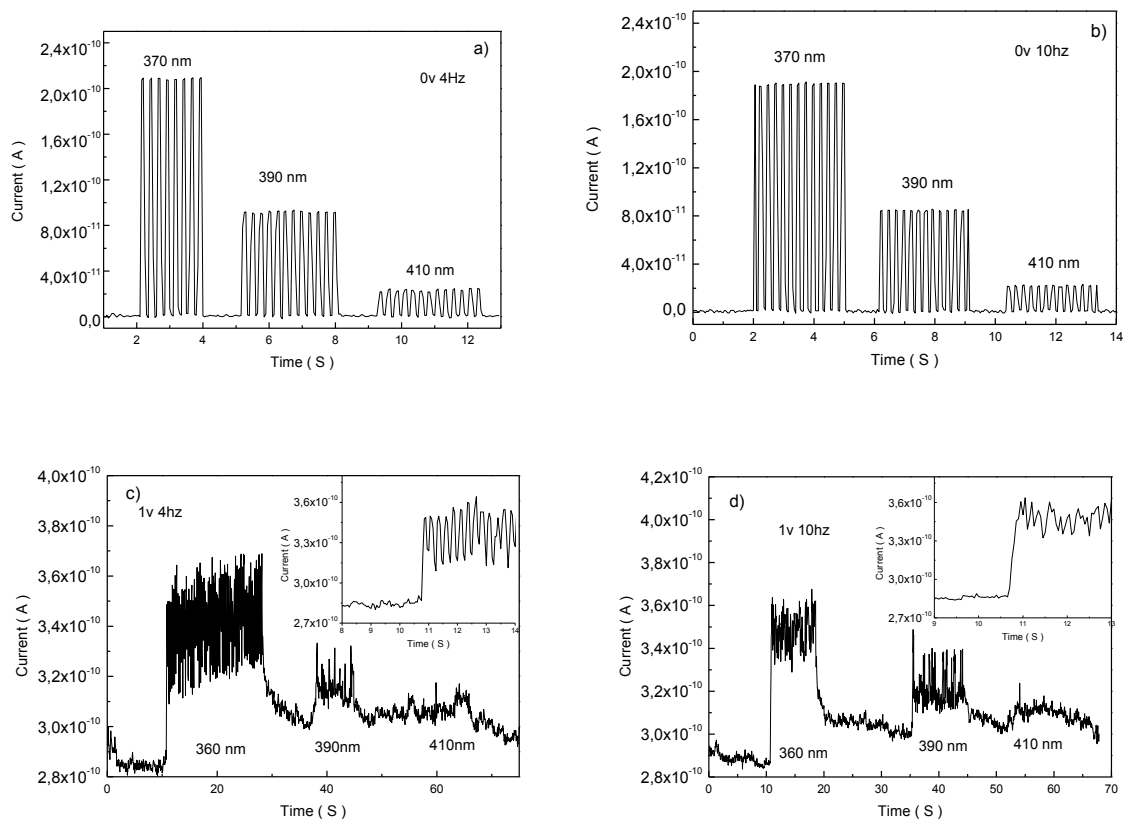


Figure 4.19: time response under illumination chopped at 4 Hz (a) and at 10 Hz (b) for wavelengths of 370 nm, 390 nm and 410 nm. Panels (c) and (d) show the response under 1 V at 4 Hz and 10 Hz. The detail of the photoresponse at 370 nm are shown in the inset of figure 4.19 (c) and figure 4.19 (d)

The results presented above suggest that the contact morphology may influence the NW photodetector behaviour. The local metal contact only collects current [25]. In this case the detector does not show any variation of the I-V slope under positive bias. The conformal contact collects the current from the entire NW surface. In this case, we observe an increase of the I-V

slope for forward bias under illumination, which is attributed to photoconductive phenomena in the p-GaN shell.

For conformal ITO contact, the difference in the photocurrent behavior can be explained by a large amount of surface states at the interface between the p-GaN and the ITO, resulting in a strong surface band bending. Under the illumination energy above the band gap of GaN, the electron-hole pairs are produced not only in the QWs but also in the core and the shell. The bended surface captures holes, whereas it repulses the electrons which remain in the inner part of the wire. When the bias is applied, the electrons can overcome the surface barrier, move inside the intrinsic region and are extracted by electrodes. As shown in figure 18, the photocurrent is generated from the MQWs lying in the field region: the electron-hole pairs in MQWs are separated by the strong internal electric field, leading to a current flow in the external circuit. This separation mechanism explains the signal under zero bias and negative bias, which gives a fast response speed. Under a forward applied voltage, less electron-hole pairs from MQWs can be collected by the electrode due to the reduction of the electric field of MQWs, while the photocurrent induced by the surface band bending becomes dominant. In this case, the mechanism is slow resulting in a longer build-up and relaxation times and a wavelength sensitivity limited to the near UV range. Finally, under a strong reverse bias (above -2 V), due to the device leakage the carrier generation in the p-GaN shell is important and the surface states play a role adding a slow contribution to the current transients.

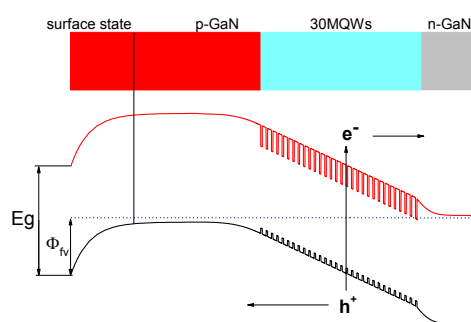


Figure 4.20: bandgap structure without bias illustrating the band bending at the NW surface.

## 4.2.6 Conclusion

In this section, I have fabricated and analyzed InGaN/GaN photodetectors with two different contact architectures, namely a localized metal contact and an ITO conformal contact. Without external bias, the two photodetector architectures show similar performance that is a fast light response (rise and decay time  $< 0.1$  s) and similar photo responsivity (around  $0.1$  A/W). The influence of contact morphology manifests itself when a bias is applied. Under forward bias, the type II photodetector presents a photocurrent gain and the photocurrent rise and decay time constant become longer, whereas this phenomenon is negligible for the type I photodetector. This can be explained by the fact that the local metal contact collects current only from a small area close to the contact, whereas, the conformal contact collects the current from the entire NW surface. Thus, the different photocurrent behavior is observed.

## 4.3 Flexible vertical InGaN/GaN core-shell NW photodiodes

In this section, I discuss the fabrication and characterization of flexible NW ensemble photodetectors based on core-shell InGaN/GaN QWs in a p-n junction. As stated in the previous section, the motivation of using radial NW structure is to take benefit of the absence of QCSE in non-polar QWs and of the large area of the active region with respect to axial NW p-n junctions for the same device footprint. For flexible array detectors, I have used the same NWs as in the previous section, which were grown by catalyst-free MOVPE on sapphire substrates by A. Messanvi at CEA/INAC. The internal structure of these wires has been described above.

### 4.3.1 Fabrication of the flexible photodetectors

I have started the fabrication of the flexible photodetectors by forming an ohmic contact on the p-GaN shell. Before the metal deposition, a photoresist layer was spin-coated to protect the n-GaN base part from metal deposition. A 3 nm/3 nm Ni/Au metallic layer was deposited on the sample surface (covering the unprotected p-GaN shells) by e-beam evaporation followed by a lift-off and a 10 min annealing in air at 400 ° C. The NWs were then encapsulated into a polydimethylsiloxane polymer (PDMS) with an average thickness of 25  $\mu\text{m}$ . The PDMS layer containing the encapsulated NWs was peeled off from the substrate and flipped upside down in order to metalize the bottom part of the NWs by Ti/Al/Ti/Au (10 nm/30 nm/10 nm/200 nm). Finally, the device was transferred on an arbitrary flexible substrate (copper tape). Silver NWs were dispersed on top of the nitride NWs in order to realize a current spreading layer. The fabrication procedure is illustrated in figure 4.21 (a). The SEM image in figure 4.21 (b) shows the top view of our flexible photodetector. The distribution of the silver NWs is uniform and the GaN NWs are well connected by the silver NWs. The density of protruding NWs is approximately  $4.2 \times 10^5/\text{cm}^2$ . A schematic image of the flexible photodetector is shown in figure 4.21 (c). The inset illustrates the flexibility of the NW photodetector.

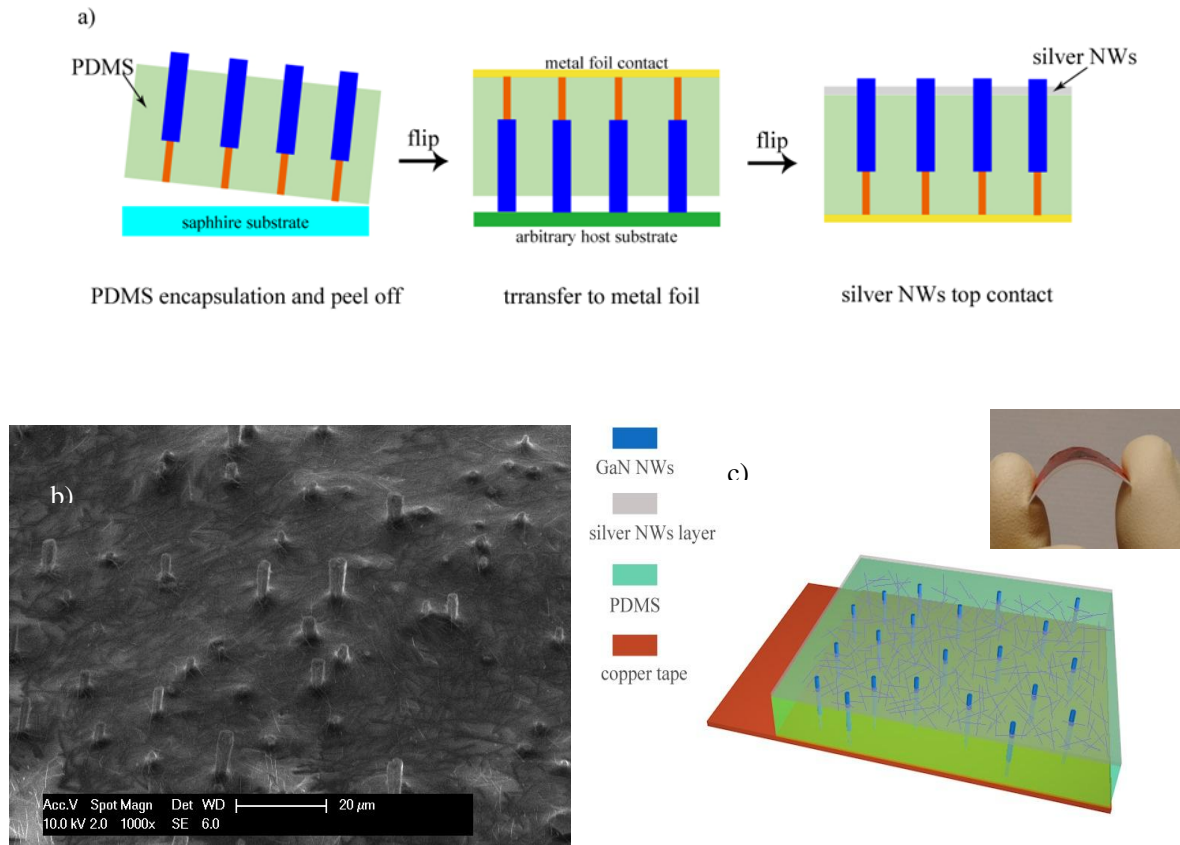


Figure 4.21: a) fabrication procedure of the flexible photodetectors. b) top view SEM image of the final flexible device. c) schematic image of the flexible photodetector. The inset shows a photo of the final device illustrating its flexibility.

### 4.3.2 Device characterization

I have first investigated the properties of flexible photodetectors by I-V measurements. I-V characteristics from 3 V to -3 V of the flexible photodetector displayed in figure 4.22 (a) (in linear scale) show a typical rectifying behavior. Under forward bias, the diode opening voltage is around 2V and the current increases steeply reaching 90 mA at 3 V. Under reverse bias, no leakage current can be observed until -3 V, which is illustrative of a good PDMS encapsulation and the absence of short circuit between the top and the bottom contacts. The I-V characteristics under illumination at a wavelength of 370 nm and in the dark are shown in the inset of figure 4.22 (a) in a semi-logarithmic

scale. Under the excitation at 370 nm and at zero bias, the current is increased by three orders of magnitude from the noise level ( $1.3 \times 10^{-12}$ ) up to  $1.2 \times 10^{-9}$  A. The photocurrent, i.e. the difference between the current under illumination and in the dark, is presented in figure 4.22 (b).

c

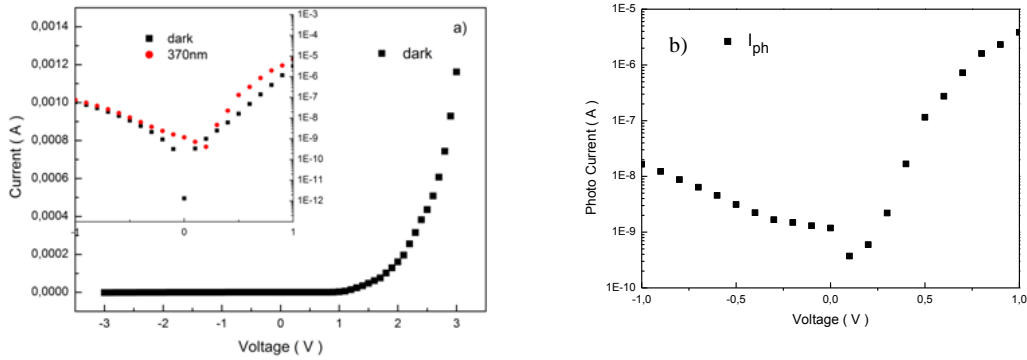


Figure 4.22: a) I-V characteristics (linear scale) in the dark of the flexible photodetector. The inset shows the I-V characteristics with and without illumination in logarithmic scale. b) Absolute value of the photocurrent versus applied bias.

To better understand the spectral dependence of the detector response, photocurrent spectrum is measured. Figure 4.23 shows the RT photocurrent spectrum in logarithmic scale under zero bias and  $-0.4$  V bias, respectively. Similar to single wire photodetectors, the onset of photocurrent occurs below the GaN bandgap at around  $2.8$  eV ( $440$  nm). The slope of the signal is less steep than in single wire detectors, which can be explained by In content inhomogeneities from wire to wire. The photocurrent signal increases rapidly above  $2.95$  eV. The photo responsivity reaches a maximum value of  $0.1$  A/W at  $3.34$  eV. This value is calibrated by the beam surface area ( $3014.5 \mu\text{m}^2$ ) (see the schematic of figure 4.24. The beam surface is represented by a violet area in the figure.). As we mentioned, the density of protruding GaN NWs is approximately  $1.2 \times 10^6/\text{cm}^2$ , which means the effective absorption area in beam surface is approximately  $115 \mu\text{m}^2$ , which means that for a higher density NW ensemble the responsivity can potentially reach  $2.6$  A/W if 100% surface coverage is assumed. At energies above  $3.4$  eV, the decrease of the photocurrent ( $0.06$  A/W at  $4.1$  eV) is likely to be related to the same effects

as in the single NW case discussed in section 4.2.3, namely the reduced absorption length in the UV and the recombination of photocarriers on the surface states of the p-GaN shell. The photocurrent at -0.5 V follows a similar spectral evolution and, thanks to the broadening of the internal electrical field region and a better carrier extraction, the photocurrent is larger giving a higher peak responsivity of 0.16 A/W.

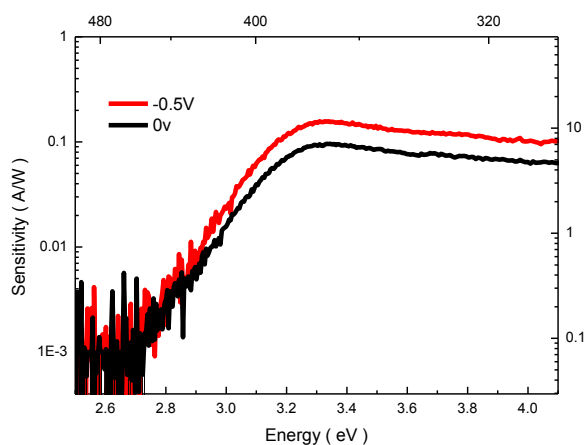


Figure 4.23: RT photocurrent spectrum in log scale under zero bias and -0.5 V, respectively.

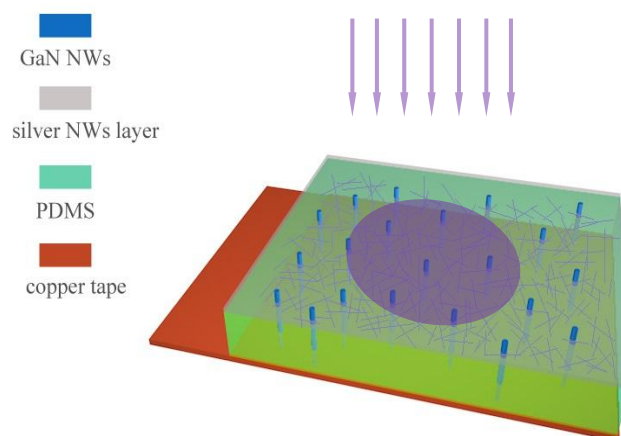


Figure 4.24 schematic showing the photodetector and the beam surface.

The inset of figure 4.25 shows the photodetector temporal response for a single light pulse at 370 nm wavelength measured under zero voltage. The rise and decay times are below 0.1 sec, i.e. below the time resolution of our measurement system. For forward biases the detector exhibits a slow response similar to

the single nanowire case. Figure 4.25 presents the power dependence of the photocurrent under  $\lambda=370$  nm illumination. I have varied the incident power density by almost four orders of magnitude from  $5 \times 10^{-6}$  W/cm<sup>2</sup> to  $1.1 \times 10^{-2}$  W/cm<sup>2</sup>. At weak and medium excitation, the photocurrent exhibits a linear increase with power up to  $1.5 \times 10^{-9}$  A for  $9.5 \times 10^{-4}$  W/cm<sup>2</sup>. At larger intensities the dependence becomes sub-linear and the photocurrent saturates at around  $5 \times 10^{-9}$  A. We attribute the sublinear power behavior to the presence of surface states at the NW surface, which at low power contribute to the photoresponse by changing the band bending and thus the access resistance, but at high power become saturated.

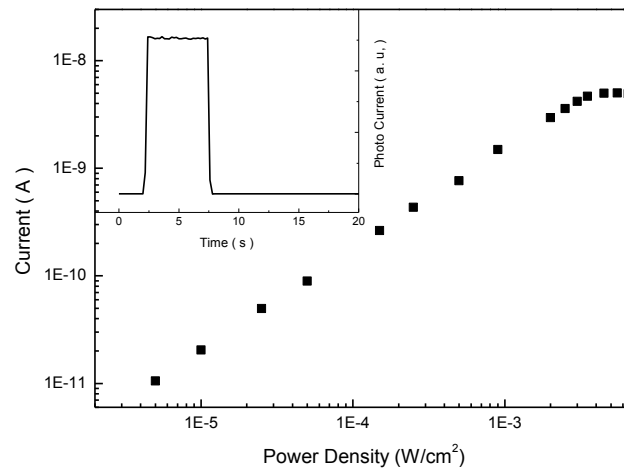


Figure 4.25: photocurrent versus power density under zero applied voltage. The inset shows the photocurrent under illumination by a single light pulse at 370 nm wavelength.

I have also investigated the influence of the illumination angle onto the photodetector. The flexible photodetector was excited by a frequency doubled Ar<sup>2+</sup> ion laser at  $\lambda=244$ nm. The photocurrent is collected for the incident angle  $90-\theta$  at  $\theta = 0^\circ$  (normal incidence),  $10^\circ$ ,  $20^\circ$  and  $45^\circ$ , respectively. The photocurrent signal versus  $\theta$  is shown in figure 4.26 (a) for different incident powers. The photocurrent for illumination at normal incidence onto the detector increases when the incident power density is varied from  $2$  mW/cm<sup>2</sup> to  $16$  mW/cm<sup>2</sup>. As the sample is rotated, the photocurrent for each power density increases with the incident angle. For example, at  $16$  mW/cm<sup>2</sup>, the photocurrent is around  $5$  nA when the laser is perpendicular to the sample surface and is  $14$  nA, i.e. almost three times higher, when the sample is tilted by  $45$  degrees. This phenomenon can be explained by the enhanced light harvesting

when the sample is rotated. Indeed, the density of contacted NWs is low, they cover only 3.82% of the total surface. At normal incidence, only a small part of the NW surface (mainly their top surface) absorbs light, as illustrated in figure 4.26 (b). The effects of light concentration reported for NW solar cells do not play important role for the wire diameters in the 1-2  $\mu\text{m}$  that I'm using in this study. When the photodetector is tilted as shown in figure 4.26 (c), the light is not only absorbed by the top surface but also by the NW side walls, which increases the portion of the absorbed light and induces a stronger photocurrent from NWs. This increase of the photocurrent takes place for all measured illumination powers. The signal evolution with power is always sublinear as discussed above in Fig. 4.26 a).

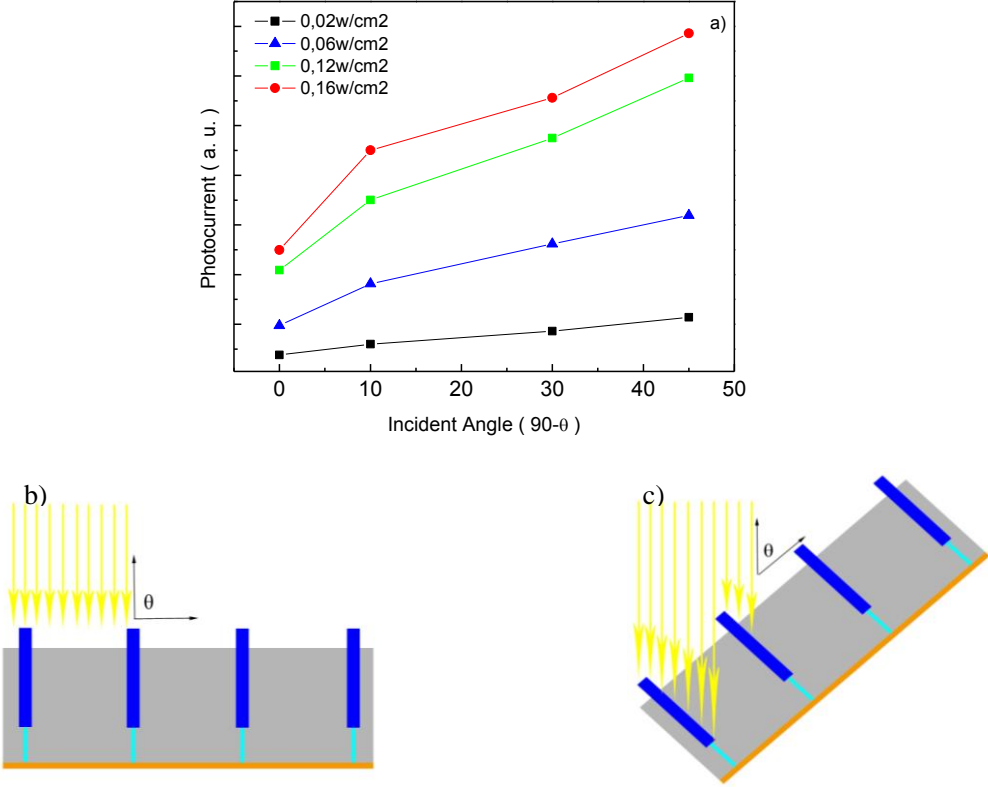


Figure 4.26: (a) photocurrent versus illumination angle for different power densities. Schematic of the photodetector illuminated (b) at normal incidence and (c) at a tilted angle (c)

The use of silver NWs as the top flexible and transparent contact plays an important role in current collection. To prove the wire to wire connection by the silver NWs on a long range, a piece of the flexible photodetector with 7 cm  $\times$  5 cm size was characterized by EBIC microscopy. Figure 4.27 (a)

presents an overall SEM image of the flexible device and the area used for EBIC measurements is shown by a yellow square. The efficiency of the current spreading in the silver NWs can be assessed by comparing the structural image and the corresponding EBIC map. At zero voltage, when the electron beam is incident onto the NW surface with an acceleration voltage of 20 kV, the electron-hole pairs are separated by the internal electrical field, transported by the silver NW network and finally collected by the electrode. A higher magnification SEM image and the corresponding EBIC map are shown in figure 4.27 (b) and 4.27 (c), respectively. The total number of NWs counted in the right-up rectangle is 13. As shown in figure 4.27 (c), the EBIC map reveals that there are 11 out of 13 NWs which produce an EBIC signal (bright contrast). This very good yield proves that most of the NWs protruding from the PDMS layer are connected by the silver NWs. However, I should note that a non-negligible part of NW having a length shorter than 25  $\mu\text{m}$  are buried in the PDMS layer. This problem can be solved in the future by using homogeneous NWs grown by selective area epitaxy.

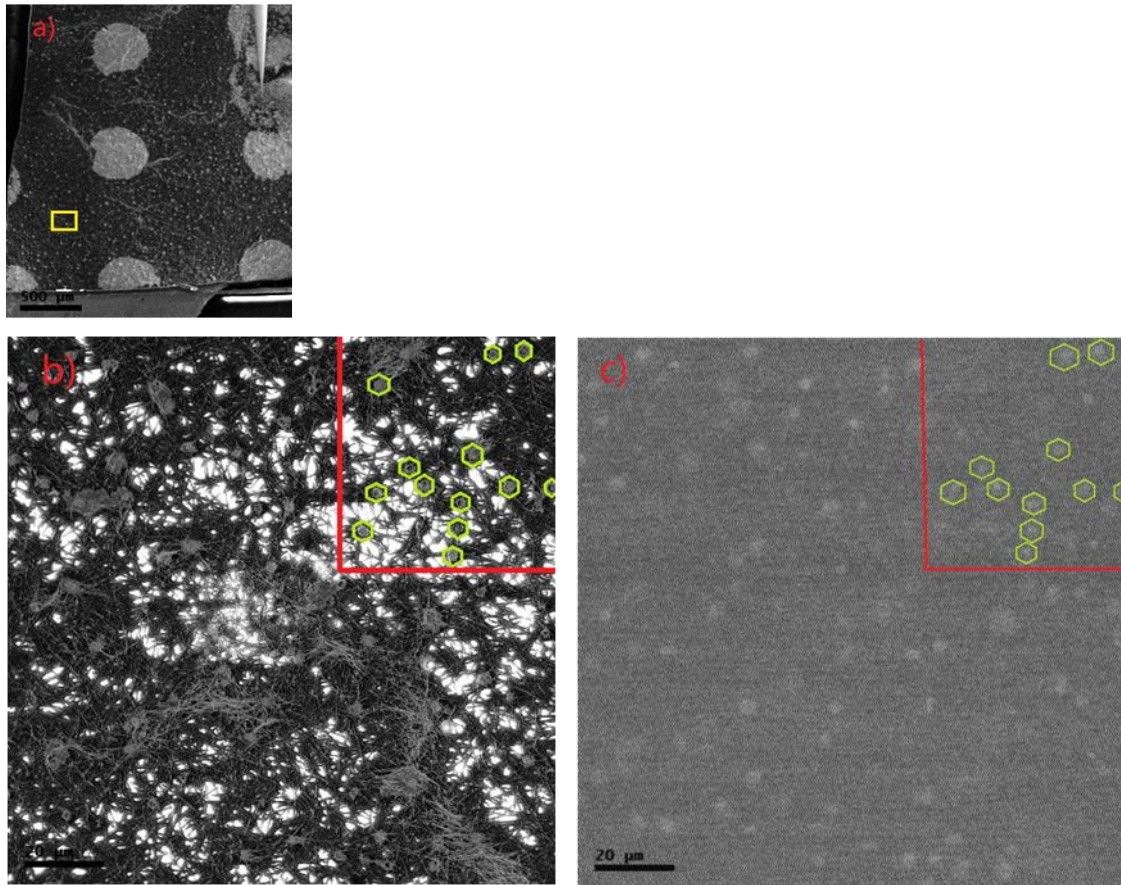


Figure 4.27: (a) SEM image of the flexible photodetector surface. (b) SEM image of the selected area indicated by the yellow rectangle in (a). (c) corresponding EBIC map for the same selected area. The active NWs giving rise to an EBIC signal are shown by green hexagons.

### 4.3.3 Conclusion

In this section, I have fabricated and characterized flexible InGaN/GaN NW array photodetectors. Flexible photodetector presents a response in the visible to UV spectral range starting from 2.8 eV. The peak responsivity is around 0.1 A/W (2.6 A/W if normalizing by the NW surface ) at 3.36 eV at zero bias. The on-off switching time under square light pulses is found to be below 0.1 sec under zero bias. The angle dependent measurements prove that the NW density is too low to collect all the incident light, so that tilting of the sample leads to the increase of the detector responsivity. Finally, the EBIC microscopy validates the current collection by the flexible contact based on a silver nanowire network.

## References

- [1] Sanford, N. A., et al. "Steady-state and transient photoconductivity in c-axis GaN nanowires grown by nitrogen-plasma-assisted molecular beam epitaxy." *Journal of Applied Physics* 107.3 (2010): 034318.
- [2] Chen, Reui-San, et al. "Ultrahigh photocurrent gain in m-axial GaN nanowires." *Applied Physics Letters* 91.22 (2007): 223106-223106.
- [3] González-Posada, F., et al. "Room-temperature photodetection dynamics of single GaN nanowires." *Nano letters* 12.1 (2011): 172-176.
- [4] Calarco, Raffaella, et al. "Size-dependent photoconductivity in MBE-grown GaN-nanowires." *Nano letters* 5.5 (2005): 981-984.
- [5] Hong, Young Joon, et al. "van der Waals epitaxy of InAs nanowires vertically aligned on single-layer graphene." *Nano letters* 12.3 (2012): 1431-1436.
- [6] Xie, Chao, et al. "Monolayer graphene film/silicon nanowire array Schottky junction solar cells." *Applied Physics Letters* 99.13 (2011): 133113.
- [7] Hyesung Park, et al., "Graphene Cathode-Based ZnO Nanowire Hybrid Solar Cells," *Nano Lett* **13** (1) (2013), 233-239.
- [8] Dukhyun Choi, et al., "Fully Rollable Transparent Nanogenerators Based on Graphene Electrodes," *Adv Mater* **22** (19) (2010), 2187-2192.
- [9] Eon Lee, Sang, and Jong Hyeok Park. "Highly robust silicon nanowire/graphene core-shell electrodes without polymeric binders." *Nanoscale* 5.19 (2013): 8986-8991.
- [10] Yu Ye, Lin Gan and Lun Dai et al., "Multicolor graphene nanoribbon/semiconductor nanowire heterojunction light-emitting diodes," *J Mater Chem* **21** (32) (2011), 11760.
- [11] Haixin Chang, et al., "A highly sensitive ultraviolet sensor based on a facile in situ solution-grown ZnO nanorod/graphene heterostructure," *Nanoscale* **3** (1) (2011), 258-264.
- [12] Hyungwoo Lee, et al., "Graphene-nanowire hybrid structures for high-performance photoconductive devices," *J Mater Chem* **22** (17) (2012), 8372.
- [13] Xue-Wen Fu, et al., "Graphene/ZnO nanowire/graphene vertical structure based fast-response ultraviolet photodetector," *Appl Phys Lett* **100** (22) (2012), 223114.

- [14] F. González-Posada, et al., "Room-Temperature Photodetection Dynamics of Single GaN Nanowires," *Nano Lett* **12** (1) (2012), 172-176.
- [15] Andres de Luna Bugallo, et al., "Visible-blind photodetector based on p-i-n junction GaN nanowire ensembles," *Nanotechnology* **21** (31) (2010), 315201.
- [16] S. Tongay, M. Lemaitre and T. Schumann et al., "Graphene/GaN Schottky diodes: Stability at elevated temperatures," *Appl Phys Lett* **99** (10), 102102 (2011).
- [17] Wang, Liancheng, et al. "Interface and transport properties of GaN/graphene junction in GaN-based LEDs." *Journal of Physics D: Applied Physics* **45**.50 (2012): 505102.
- [18] S. J. Chang, M. L. Lee and J. K. Sheu et al., "GaN Metal – Semiconductor – Metal Photodetectors With Low-Temperature-GaN Cap Layers and ITO Metal Contacts," *Ieee Electr Device L* **24** (4), 212-214 (2003).
- [19] J. Pereiro, C. Rivera and A. Navarro et al., "Optimization of InGaN – GaN MQW Photodetector Structures for High-Responsivity Performance," *Ieee J Quantum Elect* **45** (6) (2009), 617-622.
- [20] A. De Luna Bugallo, L. Rigutti and G. Jacopin et al., "Single-wire photodetectors based on InGaN/GaN radial quantum wells in GaN wires grown by catalyst-free metal-organic vapor phase epitaxy," *Appl Phys Lett* **98** (23), 233107 (2011).
- [21] M. Tchernycheva, A. Messanvi and A. de Luna Bugallo et al., "Integrated Photonic Platform Based on InGaN/GaN Nanowire Emitters and Detectors," *Nano Lett* **14** (6), 3515-3520 (2014).
- [22] R. Koester, J. S. Hwang and C. Durand et al., "Self-assembled growth of catalyst-free GaN wires by metal-organic vapour phase epitaxy," *Nanotechnology* **21** (1), 15602 (2010).
- [23] P. Lavenus, A. Messanvi and L. Rigutti et al., "Experimental and theoretical analysis of transport properties of core-shell wire light emitting diodes probed by electron beam induced current microscopy," *Nanotechnology* **25** (25), 255201 (2014).
- [24] Jacopin, Gwéoléc et al. "Single-wire light-emitting diodes based on GaN wires containing both polar and nonpolar InGaN/GaN quantum wells." *Applied Physics Express* **5**.1 (2011): 014101.

## Chapter 5 General conclusion

Nanowire growth has been pioneered several decenies ago with the works of Wagner and Ellis in 1964<sup>[1]</sup>. However, in these early works, the diameter of the wires was in the hudreds of microns scale and no practical applications could be found at that time. The development of epitaxial growth techniques and nanotechnologies has enabled the synthesis of nanowire with diameters going down to tens of nanometers. These novel functionalities and the design freedom offered by these nanoobjects has stimulated a widespread interest in their properties. Regarding nitride materials, the nanostructuring of the active region in the form of nanowires allows not only to explore novel geometries and properties, but also to solve the main problem of nitride thin films, namely the presence of a large number of threading dislocations.

The studies that I have carried out during my PhD thesis follow this general trend to explore the benefits of the III-N nanowires for optoelectronic applications such as light emission and photodetection. My objective was to fabricate nanowire devices and to understand their operation, to identify their weak points and to propose solutions for their performance improvement. The methodology that I have been using is the following : I have started from the investigation of single nanowire devices in order to understand their properties and to disentangle the effect of wire-to-wire inhomogeneities. I have then applied these results to fabricate, understand and improve nanowire array devices. In particular, I have proposed and optimized new fabrication approaches allowing for example to overcome the electrical injection inhomogeneities.

I have started my work by the fabrication and characterization of single lateral nanowire InGaN/GaN LEDs with a transparent graphene contact for hole injection. Single wire LEDs were fabricated and a transparent graphene sheet structured by e-beam lithography for hole injection. Reference single wire LEDs with metal contacts were also fabricated for comparison. The results show the illumination spectra are strongly dependent on the contact location. For an extended contact and a contact localized on the m-plane, a transition from the green to blue emission is observed whereas for a localized contact on the m-plane/semipolar plane junction the emission remains green.

To confirm the results that I have obtained on in-plane graphene-contacted nanowire LEDs, I then focused on single vertical nanowire LEDs with a conformal ITO contact fabricated from a nanowire array. The array LED electroluminescence presented the same spectral features and the same broadening as for the single nanowire devices, in particular, showing two spectral contributions from the m-plane quantum well and from the In-rich region. I have applied the knowledge gained about the electroluminescence dependence on the contact layout to propose and realize a new contacting architecture using ITO etch-back and plasma treatment to inhibit the p-type conductivity. Following this procedure, the unwanted green contribution at medium and high injection was suppressed. The selective contacting of the m-plane and the plasma treatment of the nanowire top appear as a promising solution for controlling the color of core/shell nanowire LEDs with inhomogeneous internal composition. Furthermore, I have analyzed the injection inhomogeneity induced by charge traps at the interface between the nanowire n-GaN core and the radially grown n-GaN underlayer. The presence of traps at this interface impedes the homogeneous injection and reduces the performance of the nanowire array LEDs. In order to overcome this problem, I have proposed and optimized the fabrication of “front contacted” LEDs. This contact architecture allows to inject electrons directly into the n-GaN underlayer. The “front contacted” LEDs present an increased yield of active NWs in the electroluminescence maps from 19% for standard fabrication to 65% for front contacted LEDs, thus reducing the negative impact of the charge traps.

In the last part, I have studied nitride nanowire photodetectors. First, I have used homogeneous GaN nanowires to demonstrate ultraviolet photodetectors using graphene as a top transparent contact. The detector presented a responsivity of 25 A/W at 1 V bias at 357 nm at low excitation power. The photocurrent spectrum showed that the detector response is related to the GaN nanowire photoconductivity and attested the good optical transparency of the graphene electrode at least up to 4.15 eV. Next, I have fabricated and analyzed core/shell InGaN/GaN nanowire photodetectors. I have analyzed single nanowire devices with a localized metal contact and an ITO conformal contact. The influence of contact morphology manifests itself when a bias is applied. Under forward bias, the photodetectors presented a photocurrent gain and the photocurrent rise and decay times are long. Under zero bias, the detector operated as a photodiode and exhibited a fast response.

Finally, I have fabricated and characterized flexible InGaN/GaN NW array photodetectors. The flexible photodetectors presented a response in the visible to UV spectral range starting from 2.8 eV with a zero-bias peak responsivity around 0.1 A/W at 3.36 eV. The on-off switching time under square light pulses was found to be below 0.1 sec under zero bias. The angle dependent measurements prove that the NW density is too low to collect the entire incident light, so that tilting of the sample leads to the increase of the detector responsivity.

To summarize, my work has allowed to improve the understanding of the operation of nanowire LEDs and photodetectors, to identify problems and to propose several solutions. Regarding the perspectives of my work, there is still much room for improvement of the nanowire LEDs. Namely, further optimization of the NW growth avoiding traps and compositional inhomogeneities and a thorough analysis of the current injection are necessary to bring NW LEDs to maturity and in particular to fully benefit from the core/shell geometry for droop reduction. As far as flexible devices are concerned, my work on flexible photodetectors is now pursued by other PhD students in our group in order to develop flexible nanowire-based solar cells and piezogenerators. This is indeed a versatile concept allowing to combine inorganic active material with polymers for high-efficiency flexible devices.

[1] Trentler, Timothy J., et al. "Solution-liquid-solid growth of crystalline III-V semiconductors: an analogy to vapor-liquid-solid growth." *Science* 270.5243 (1995): 1791.

## Appendix A: list of Abbreviations

AlN	Aluminum nitride
BN	Boron nitride
CBED	Convergent beam electron diffraction
CL	Cathodoluminescence
CVD	Chemical vapor deposition
DAP	Donor-acceptor pair
EBIC	Electron beam induced current
EDX	Energy-dispersive X-ray spectroscopy
EL	Electroluminescence
EQE	External quantum efficiency
FIB	Focused ion beam
FWHM	Full width at half-maximum
GaN	Gallium nitride
HSQ	Hydrogen silsesquioxane polymer
ICP	Inductively Coupled Plasma
InN	Indium nitride
ITO	Indium tin oxide
LDs	Laser diodes
LEDs	Light emitting diodes
MBE	Molecular beam epitaxy
MOCVD	Metal organic chemical vapor deposition
NBE	Near band edge
PDMS	Polydimethylsiloxane
PECVD	Plasma-enhanced chemical vapor deposition
QCSE	Quantum confined stark effect
QW	Quantum well
SAG	Selected area growth

SEM	Scanning electron microscope
SiC	Silicon carbon
TEM	Transmission electron microscopy
VLS	Vapor-liquid-solid
ZnO	Zinc oxide
$\mu$ PL	Micro-photoluminescence

## Appendix B: list of publication

### Journals

1. **Hezhi. Zhang** Agnès Messanvi, Christophe Durand, Joël Eymery, Pierre Lavenus, Andrey Babichev, François H. Julien, Maria Tchernycheva, “InGaN/GaN core/shell nanowires for visible to ultraviolet range photodetection” *Phys. Stat. Sol. A* 1-5, (2016)
2. Kumaresan, Vishnuvarthan; Largeau, Ludovic; Oehler, Fabrice; **Zhang, Hezhi**; Mauguin, Olivia; Glas, Frank; GOGNEAU, Noelle; Tchernycheva, Maria; Harmand, Jean-Christophe; “Self-induced growth of vertical GaN nanowires on silica” accepted by *Nonotechnology*, NANO-108394
3. Neplokh V, Messanvi A, **Zhang H**, Julien FH, Babichev A, Eymery J, Durand C, and Tchernycheva M. Substrate-Free InGaN/GaN Nanowire Light-Emitting Diodes. *Nanoscale Res Lett.*10(1):447, 2015
4. **Hezhi. Zhang**, Gwénoél Jacopin, Vladimir Neplokh, Ludovic Largeau, François H. Julien, Olga Kryliouk, Maria Tchernycheva Color control of nanowire InGaN/GaN light emitting diodes by post-growth treatment”, *Nanotechnology*, 465203 (26) 2015
5. Messanvi, Agnès; **Zhang, Hezhi**; Neplokh, Vladimir; Julien, François; Bayle, Fabien; Foldyna, Martin; Bougerol, Catherine; Gautier, Eric; Babichev, Andrey; Durand, Christophe; Eymery, Joël; Tchernycheva, Maria, “Investigation of photovoltaic properties of single core-shell GaN/InGaN wires”, *ACS Applied Materials & Interfaces*, 7 ( 39 ) 2015.
6. Jacopin, Gwenole; Shahmohammadi, Mehran; Ganière, Jean Daniel Ganière; **Zhang, Hezhi**; Ciechonski, Rafal; Vescovi, Giuliano; Kryliouk, Olga; Tchernycheva, Maria, "Excitonic diffusion in InGaN/GaN core-shell nanowires", accepted by *Nanoletters*, nl-2015-03611x.
7. Xing Dai, Agnes Messanvi, **Hezhi Zhang**, Vladimir Neplokh, Christophe Durand, Joël Eymery, François H. Julien and Maria Tchernycheva, “Flexible light-emitting diodes based on vertical nitride nanowires”, *Nano letters* 15(10) 2015
8. M. Tchernycheva, V. Neplokh, **H. Zhang**, P. Lavenus, L. Rigutti, F. Bayle, F. H. Julien, A. Babichev, G. Jacopin, L. Largeau, R. Ciechonski, G. Vescovi and O. Kryliouk “Core-shell InGaN/GaN nanowire light emitting diodes analyzed by electron beam induced current microscopy and cathodoluminescence mapping”, *Nanoscale* 7, 11697(2015).
9. Lavenus P, Messanvi A, Rigutti L, Bugallo A De Luna, **Zhang H**, Bayle F, Julien F H, Eymery J, Durand C, Tchernycheva M, “ Experimental and theoretical analysis of transport properties of core/shell wire light emitting diodes probed by electron beam induced current microscopy”,

*Nanotechnology* 25, 255201 (2014).

10. Tchernycheva M, Messanvi A, de Luna Bugallo A, Jacopin G, Lavenus P, Rigutti L, **Zhang H**, Halioua Y, Julien F. H, Eymery J, Durand C, “Integrated Photonic Platform Based on InGaN/GaN Nanowire Emitters and Detectors”, *Nano Letters* 14, 3515 (2014).
11. Tchernycheva M, Lavenus P, **Zhang H**, Babichev A V, Jacopin G, Shahmohammadi M, Julien F H, Ciechonski R, Vescovi G, Kryliouk O, “ InGaN/GaN Core/Shell Single Nanowire Light Emitting Diodes with Graphene-Based P-Contact”, *Nano Letters* 14, 2456 (2014).
12. **H Zhang**, AV Babichev, G Jacopin, P Lavenus, FH Julien, A Yu Egorov, J Zhang, T Pauport é M Tchernycheva, “ Characterization and modeling of a ZnO nanowire ultraviolet photodetector with graphene transparent contact”, *Journal of Applied Physics* 114, 234505 (2013)
13. A. V. Babichev, **H. Zhang**, P. Lavenus, F. H. Julien, A. Yu. Egorov, Y. T. Lin, L. W. Tu and M. Tchernycheva, “ GaN nanowire ultraviolet photodetector with a graphene transparent contact” *Appl. Phys. Lett.* 103, 201103 (2013)

## **International Conferences (orals)**

1. “Flexible light emitting diodes based on vertical GaN nanowires” Xing Dai, Agnes Messanvi, **Hezhi Zhang**, Christophe Durand, Jođ Eymery, François H. Julien, Maria Tchernycheva. Compound semiconductor week 2015.
2. “InGaN/GaN core-shell single nanowire light emitting diodes with graphene-based p-contact” **H. Zhang**, P. Lavenus, A. V. Babichev, V. Neplokh, G. Jacopin, M. Shahmohammadi, F. H. Julien, R. Ciechonski, G. Vescovi, O. Kryliouk, M. Tchernycheva. International Workshop on Nitride Semiconductors IWN 2014, 24-29 August 2014 Wroclaw, Poland
3. “Wide Bandgap Nanowire Ultraviolet Photodetectors With A Graphene Transparent Contact” **H. Zhang**, A. V. Babichev, P. Lavenus, G. Jacopin, F. H. Julien, A. Yu. Egorov, J. Zhang, T. Pauport é Y. T. Lin, L. W. Tu, and M. Tchernycheva, the international symposium on compound semiconductor. France

## Appendix C: Code of silvaco of 30MQWs photodetector

```

go atlas
# Parameters
#####
# Epilayer # Material # Type # Thickness # Doping # Mobility #
# # # p or n # [nm] # [cm-3] # [cm2/V-s] #
#####
#4 p-Contact # GaN # p # 150 # 1e17 # 50 #
#3 30barrier # GaN # - # 10 # - # 200 #
#2 30well # In0.18GaN # - # 5 # - # 200 #
#1 core # GaN # n # 500 # 1e18 # 100 #
#####

#-----
# SECTION 1 : MESH GENERATION
#-----
#
mesh width=1e8
#
x.mesh loc=0.0 spac=0.25
x.mesh loc=0.5 spac=0.25
#
y.mesh loc=0.0 spac=0.05
y.mesh loc=0.13 spac=0.002
y.mesh loc=0.15 spac=0.0002 #P-GaN 1
y.mesh loc=0.174 spac=0.0005 #1GaN_barrier 2
y.mesh loc=0.180 spac=0.0005 #1InGaN_well 3
y.mesh loc=0.204 spac=0.0005 #2GaN_barrier 4
y.mesh loc=0.210 spac=0.0005 #2InGaN_well 5
y.mesh loc=0.234 spac=0.0005 #3GaN_barrier 6
y.mesh loc=0.240 spac=0.0005 #3InGaN_well 7
y.mesh loc=0.264 spac=0.0005 #4GaN_barrier 8
y.mesh loc=0.270 spac=0.0005 #4InGaN_well 9
y.mesh loc=0.294 spac=0.0005 #5GaN_barrier 10
y.mesh loc=0.300 spac=0.0005 #5InGaN_well 11
y.mesh loc=0.324 spac=0.0005 #6GaN_barrier 12
y.mesh loc=0.330 spac=0.0005 #6InGaN_well 13
y.mesh loc=0.354 spac=0.0005 #7GaN_barrier 14
y.mesh loc=0.360 spac=0.0005 #7InGaN_well 15
y.mesh loc=0.384 spac=0.0005 #8GaN_barrier 16
y.mesh loc=0.390 spac=0.0005 #8InGaN_well 17

```

y.mesh	loc=0.414	spac=0.0005	#9GaN_barrier	18
y.mesh	loc=0.420	spac=0.0005	#9InGaN_well	19
y.mesh	loc=0.444	spac=0.0005	#10GaN_barrier	20
y.mesh	loc=0.450	spac=0.0005	#10InGaN_well	21
y.mesh	loc=0.474	spac=0.0005	#11GaN_barrier	22
y.mesh	loc=0.480	spac=0.0005	#11InGaN_well	23
y.mesh	loc=0.504	spac=0.0005	#12GaN_barrier	24
y.mesh	loc=0.510	spac=0.0005	#12InGaN_well	25
y.mesh	loc=0.534	spac=0.0005	#13GaN_barrier	26
y.mesh	loc=0.540	spac=0.0005	#13InGaN_well	27
y.mesh	loc=0.564	spac=0.0005	#14GaN_barrier	28
y.mesh	loc=0.570	spac=0.0005	#14InGaN_well	29
y.mesh	loc=0.594	spac=0.0005	#15GaN_barrier	30
y.mesh	loc=0.600	spac=0.0005	#15InGaN_well	31
y.mesh	loc=0.624	spac=0.0005	#16GaN_barrier	32
y.mesh	loc=0.630	spac=0.0005	#16InGaN_well	33
y.mesh	loc=0.654	spac=0.0005	#17GaN_barrier	34
y.mesh	loc=0.660	spac=0.0005	#17InGaN_well	35
y.mesh	loc=0.684	spac=0.0005	#18GaN_barrier	36
y.mesh	loc=0.690	spac=0.0005	#18InGaN_well	37
y.mesh	loc=0.714	spac=0.0005	#19GaN_barrier	38
y.mesh	loc=0.720	spac=0.0005	#19InGaN_well	39
y.mesh	loc=0.744	spac=0.0005	#20GaN_barrier	40
y.mesh	loc=0.750	spac=0.0005	#20InGaN_well	41
y.mesh	loc=0.774	spac=0.0005	#21GaN_barrier	42
y.mesh	loc=0.780	spac=0.0005	#21InGaN_well	43
y.mesh	loc=0.804	spac=0.0005	#22GaN_barrier	44
y.mesh	loc=0.810	spac=0.0005	#22InGaN_well	45
y.mesh	loc=0.834	spac=0.0005	#23GaN_barrier	46
y.mesh	loc=0.840	spac=0.0005	#23InGaN_well	47
y.mesh	loc=0.864	spac=0.0005	#24GaN_barrier	48
y.mesh	loc=0.870	spac=0.0005	#24InGaN_well	49
y.mesh	loc=0.894	spac=0.0005	#25GaN_barrier	50
y.mesh	loc=0.900	spac=0.0005	#25InGaN_well	51
y.mesh	loc=0.924	spac=0.0005	#26GaN_barrier	52
y.mesh	loc=0.930	spac=0.0005	#26InGaN_well	53
y.mesh	loc=0.954	spac=0.0005	#27GaN_barrier	54
y.mesh	loc=0.960	spac=0.0005	#27InGaN_well	55
y.mesh	loc=0.984	spac=0.0005	#28GaN_barrier	56
y.mesh	loc=0.990	spac=0.0005	#28InGaN_well	57
y.mesh	loc=1.014	spac=0.0005	#29GaN_barrier	58
y.mesh	loc=1.020	spac=0.0005	#29InGaN_well	59
y.mesh	loc=1.044	spac=0.0005	#30GaN_barrier	60

```

y.mesh loc=1.050  spac=0.0005          #30InGaN_well    61
y.mesh loc=1.100  spac=0.001
y.mesh loc=1.550  spac=0.05            #n_GaN           62

```

```

#-----
# SECTION 2: REGIONS AND ELECTRODES
#-----

```

```

region num=1 material=GaN    y.max=0.15
region num=2 material=GaN    y.min=0.15 y.max=0.174 name=barrier
region num=3 material=InGaN  y.min=0.174 y.max=0.180 x.comp=0.18 name=well qwell led
well.ny=50
region num=4 material=GaN    y.min=0.180 y.max=0.204 name=barrier
region num=5 material=InGaN  y.min=0.204 y.max=0.210 x.comp=0.18 name=well qwell led
well.ny=50
region num=6 material=GaN    y.min=0.210 y.max=0.234 name=barrier
region num=7 material=InGaN  y.min=0.234 y.max=0.240 x.comp=0.18 name=well qwell led
well.ny=50
region num=8 material=GaN    y.min=0.240 y.max=0.264 name=barrier
region num=9 material=InGaN  y.min=0.264 y.max=0.270 x.comp=0.18 name=well qwell led
well.ny=50
region num=10 material=GaN   y.min=0.270 y.max=0.294 name=barrier
region num=11 material=InGaN y.min=0.294 y.max=0.300 x.comp=0.18 name=well qwell led
well.ny=50
region num=12 material=GaN   y.min=0.300 y.max=0.324 name=barrier
region num=13 material=InGaN y.min=0.324 y.max=0.330 x.comp=0.18 name=well qwell led
well.ny=50
region num=14 material=GaN   y.min=0.330 y.max=0.354 name=barrier
region num=15 material=InGaN y.min=0.354 y.max=0.360 x.comp=0.18 name=well qwell led
well.ny=50
region num=16 material=GaN   y.min=0.360 y.max=0.384 name=barrier
region num=17 material=InGaN y.min=0.384 y.max=0.390 x.comp=0.18 name=well qwell led
well.ny=50
region num=18 material=GaN   y.min=0.390 y.max=0.414 name=barrier
region num=19 material=InGaN y.min=0.414 y.max=0.420 x.comp=0.18 name=well qwell led
well.ny=50
region num=20 material=GaN   y.min=0.420 y.max=0.444 name=barrier
region num=21 material=InGaN y.min=0.444 y.max=0.450 x.comp=0.18 name=well qwell led
well.ny=50
region num=22 material=GaN   y.min=0.450 y.max=0.474 name=barrier
region num=23 material=InGaN y.min=0.474 y.max=0.480 x.comp=0.18 name=well qwell led
well.ny=50
region num=24 material=GaN   y.min=0.480 y.max=0.504 name=barrier
region num=25 material=InGaN y.min=0.504 y.max=0.510 x.comp=0.18 name=well qwell led

```

```

well.ny=50
region num=26 material=GaN y.min=0.510 y.max=0.534 name=barrier
region num=27 material=InGaN y.min=0.534 y.max=0.540 x.comp=0.18 name=well qwell led
well.ny=50
region num=28 material=GaN y.min=0.540 y.max=0.564 name=barrier
region num=29 material=InGaN y.min=0.564 y.max=0.570 x.comp=0.18 name=well qwell led
well.ny=50
region num=30 material=GaN y.min=0.570 y.max=0.594 name=barrier
region num=31 material=InGaN y.min=0.594 y.max=0.600 x.comp=0.18 name=well qwell led
well.ny=50
region num=32 material=GaN y.min=0.600 y.max=0.624 name=barrier
region num=33 material=InGaN y.min=0.624 y.max=0.630 x.comp=0.18 name=well qwell led
well.ny=50
region num=34 material=GaN y.min=0.630 y.max=0.654 name=barrier
region num=35 material=InGaN y.min=0.654 y.max=0.660 x.comp=0.18 name=well qwell led
well.ny=50
region num=36 material=GaN y.min=0.660 y.max=0.684 name=barrier
region num=37 material=InGaN y.min=0.684 y.max=0.690 x.comp=0.18 name=well qwell led
well.ny=50
region num=38 material=GaN y.min=0.690 y.max=0.714 name=barrier
region num=39 material=InGaN y.min=0.714 y.max=0.720 x.comp=0.18 name=well qwell led
well.ny=50
region num=40 material=GaN y.min=0.720 y.max=0.744 name=barrier
region num=41 material=InGaN y.min=0.744 y.max=0.750 x.comp=0.18 name=well qwell led
well.ny=50
region num=42 material=GaN y.min=0.750 y.max=0.774 name=barrier
region num=43 material=InGaN y.min=0.774 y.max=0.780 x.comp=0.18 name=well qwell led
well.ny=50
region num=44 material=GaN y.min=0.780 y.max=0.804 name=barrier
region num=45 material=InGaN y.min=0.804 y.max=0.810 x.comp=0.18 name=well qwell led
well.ny=50
region num=46 material=GaN y.min=0.810 y.max=0.834 name=barrier
region num=47 material=InGaN y.min=0.834 y.max=0.840 x.comp=0.18 name=well qwell led
well.ny=50
region num=48 material=GaN y.min=0.840 y.max=0.864 name=barrier
region num=49 material=InGaN y.min=0.864 y.max=0.870 x.comp=0.18 name=well qwell led
well.ny=50
region num=50 material=GaN y.min=0.870 y.max=0.894 name=barrier
region num=51 material=InGaN y.min=0.894 y.max=0.900 x.comp=0.18 name=well qwell led
well.ny=50
region num=52 material=GaN y.min=0.900 y.max=0.924 name=barrier
region num=53 material=InGaN y.min=0.924 y.max=0.930 x.comp=0.18 name=well qwell led
well.ny=50

```

```

region num=54 material=GaN y.min=0.930 y.max=0.954 name=barrier
region num=55 material=InGaN y.min=0.954 y.max=0.960 x.comp=0.18 name=well qwell led
well.ny=50
region num=56 material=GaN y.min=0.960 y.max=0.984 name=barrier
region num=57 material=InGaN y.min=0.984 y.max=0.990 x.comp=0.18 name=well qwell led
well.ny=50
region num=58 material=GaN y.min=0.990 y.max=1.014 name=barrier
region num=59 material=InGaN y.min=1.014 y.max=1.020 x.comp=0.18 name=well qwell led
well.ny=50
region num=60 material=GaN y.min=1.020 y.max=1.044 name=barrier
region num=61 material=InGaN y.min=1.044 y.max=1.050 x.comp=0.18 name=well qwell led
well.ny=50
region num=62 material=GaN y.min=1.050 y.max=1.550
#
electrode name=anode top
electrode name=cathode bottom
#
#-----
# SECTION 3: DOPING PROFILES
#-----
# p type is Mg
# n type is Si
doping region=1 uniform p.type conc=1e17
doping region=62 uniform n.type conc=1e18
#
#-----
# SECTION 4: MATERIAL MODELS
#-----
#
material material=GaN taun0=1e-9 taup0=1e-9 copt=1.1e-8 \
    augn=1.0e-34 augp=1.0e-34
material material=AlGaIn taun0=1e-9 taup0=1e-9 copt=1.1e-8 \
    augn=1.0e-34 augp=1.0e-34
material material=InGaIn taun0=1e-9 taup0=1e-9 copt=1.1e-8 \
    augn=1.0e-34 augp=1.0e-34
#
# Lorentz Broaden factor
material well.gamma0=30e-3
#
material edb=0.080 eab=0.101
#
models wz.kp k.p fermi incomplete srh auger optr print
models regioin=4 k.p chuang spontaneous lorentz

```

```

#
mobility material=GaN mun0=100 mup0=50
mobility material=InGaN mun0=200 mup0=50
#
#-----
# SECTION 5: OUTPUT FLAGS and METHOD
#-----
#
output con.band val.band band.param charge polar.charge e.mobility \
      h.mobility u.srh u.radiative u.auger permi flowlines
#
method climitt=1e-4 maxtrap=10
#
#-----
# SECTION 6: INITIAL SOLUTION
#-----
#
solve init
solve prev
#
save outf=pd_grenoble_30MQWs.str
tonyplot pd_grenoble_30MQWs.str
quit

```

## Appendix D: Synthèse en Français

Les semi-conducteurs III-N ont connu un regain d'intérêt à la fin des années 1990 suite à la démonstration du dopage p de GaN, ce qui a ouvert la porte à une grande palette d'applications telles que les diodes électroluminescentes (LEDs), les diodes laser (LDs), les photodétecteurs et les cellules solaires. Cependant, la qualité du matériau reste le problème clé pour les dispositifs à couches minces de nitrure. Dans les dernières années, la nanostructuration de la région active sous forme de nanofils a été proposée comme une solution prometteuse pour le problème de qualité du matériel. En effet, la relaxation de contrainte par les bords libres de nanofils permet de fabriquer des nano-objets sans défauts sur des substrats à fort désaccord de maille. En outre, la grande surface latérale de nanofils permet d'augmenter la surface d'absorption ou d'émission en utilisant les hétérostructures cœur/coquille. Enfin, la croissance sur des facettes non polaires des nanofils supprime le champ électrique interne et améliore l'efficacité d'absorption / émission.

Dans ce manuscrit, je présente mon travail dédié à la réalisation et la caractérisation des émetteurs et des détecteurs de lumière à base de nanofils de nitrures. Je détaille la fabrication de dispositifs utilisant des outils de nanofabrication à l'état de l'art, ainsi que l'étude de leurs propriétés électriques et optiques. Le premier chapitre résume brièvement les propriétés de base de semi-conducteurs nitrures et décrit les méthodes d'élaboration de nanofils. Dans le deuxième chapitre, je présente mon travail sur la fabrication et la caractérisation de LED à nanofil unique InGaN/GaN ayant un contact transparent en graphène pour injection des trous. L'électroluminescence des LEDs à nanofils uniques montre l'impact de la forme de contact sur les propriétés d'émission. En particulier, la position du contact détermine l'évolution spectrale avec le courant d'injection. À savoir, pour un contact étendu et un contact localisé sur le plan m, une transition d'une émission verte vers l'émission bleue est observée alors que pour un contact localisé sur la jonction entre le plan m et le plan semipolaire l'émission reste verte. Dans le troisième chapitre, je décris la fabrication et la caractérisation des LEDs à nanofils uniques fabriqués à partir d'une matrice de nanofils verticaux avec la morphologie de contact identique aux LEDs à base d'ensemble de nanofils. L'émission montre une évolution similaire à celle des LEDs à nanofils uniques à contact latéral. La dépendance de l'électroluminescence sur la morphologie de contact donne une possibilité de contrôler la couleur d'émission de la LED à l'étape de fabrication. J'utilise un traitement

de plasma de fluor afin de réduire la conductivité de la coquille GaN dopé p pour inhiber l'injection électrique dans la région riche en In du puits quantique. En outre, j'analyse l'effet de inhomogénéité d'injection. Afin d'éviter cet effet, j'ai développé un système de contact par le haut permettant d'injecter les électrons directement dans la sous-couche n-GaN. Les LEDs fabriquées selon cette procédure montrent un rendement amélioré avec 65% de nanofils actifs contre 19% pour une procédure standard. Le dernier chapitre est consacré à l'étude des photodétecteurs à nanofils de nitrure. Je décris d'abord la fabrication et la caractérisation d'un photodétecteur de rayonnement ultraviolet basé sur un ensemble de nanofils de GaN avec un contact transparent de graphène. Ensuite, des détecteurs à nanofils uniques InGaN / GaN ont été fabriqués fonctionnant dans la gamme spectrale du visible à ultraviolet. L'influence de la morphologie de contact est également étudiée en comparant deux types de contacts, à savoir un contact métallique localisé et d'un contact étendu en oxyde d'indium-étain (ITO). Dans la dernière partie, je présente une technique pour la fabrication de photodétecteurs flexibles basée sur des ensembles de nanofils verticaux et je discute leurs performances.

## **Diodes électroluminescentes à base de nanofils**

### **Motivations**

Les diodes électroluminescentes (LEDs) à base de nitrure d'indium constituent un sujet de recherche de grande actualité en vue d'améliorer le rendement et de réduire le prix de l'éclairage à l'état solide. Malgré les performances élevées déjà atteintes et les progrès constants des LEDs à couches minces, la nanostructuration de matériaux apparaît comme une voie prometteuse pour rendre les émetteurs encore plus efficaces.

Les LEDs tridimensionnelles à base de nanofils permettent d'améliorer la qualité cristalline du matériau actif. Elles offrent aussi de nouvelles possibilités pour l'ingénierie des contraintes. De plus, la géométrie cœur-coquille rend possible l'augmentation de la surface active du dispositif pour la même surface physique ce qui permet de réduire la chute d'efficacité à fort courant d'injection. Pour les nanofils ayant l'axe étendu aligné avec la direction [0001], cette géométrie permet également de supprimer l'effet Stark quantique confiné grâce à la croissance sur des plans m non-polaires. De plus, les nanofils ouvrent la voie pour fabriquer des sources de lumière avec de nouvelles fonctionnalités. Par exemple, grâce à la dépendance de l'incorporation d'indium avec le diamètre du fil, il est possible

de changer la couleur d'émission de nano-LEDs épitaxiés sur la même plaque en changeant la taille des nano-ouvertures du template. Grâce à leur petite empreinte au sol, les nanofils peuvent être transférés sur des substrats flexibles comme le plastique ou du métal pour réaliser des LEDs déformables. Nos travaux sur ce sujet seront détaillés par la suite dans la section «perspectives».

Outre des LEDs macroscopiques, les nanofils permettent également de fabriquer des sources de lumière brillantes et ultra-compactes. Ces nano-LEDs peuvent être prélevées de leur substrat pour être par la suite intégrées dans des circuits photoniques planaires. Elles peuvent également être utilisées dans une architecture verticale comme des sources ponctuelles pour des applications de stimulation optique dans le biomédical ou pour réaliser des matrices de micro-pixels.

### **Etat de l'art**

Les premières réalisations de LEDs à nanofils de nitrides ont utilisé la géométrie axiale avec une région active contenant des puits quantiques (appelés dans ce cas des «disques quantiques») GaN/InGaN placés entre deux segments dopés n et p respectivement. On peut citer notamment les travaux de Kim et al. démontrant une LED à nano-aiguilles épitaxiés par HVPE émettant à 470 nm ou encore la démonstration par Kikuchi et al. d'une LED à base de nanofils coalescés épitaxiés par EJM avec une longueur d'onde d'émission accordable du bleu au rouge. Les LEDs utilisant la structure cœur/coquille avec des puits quantiques InGaN/GaN sur les facettes latérales sont apparues peu après avec la première démonstration réalisée par le groupe de Lieber à Harvard utilisant la croissance catalysée. Cette réalisation pionnière a été suivie par de nombreuses études utilisant la croissance spontanée et plus tard la croissance sélective. Actuellement, les grands groupes industriels (e.g. OSRAM) aussi bien que des start-ups (e.g. GLO, Aledia) investissent beaucoup d'efforts pour amener la technologie des LEDs à nanofils organisés au niveau de maturité permettant de concurrencer la technologie planaire.

La croissance organisée permet un bien meilleur contrôle de la morphologie des fils par rapport à la croissance spontanée ce qui se traduit par une réduction de la fluctuation de composition entre les nanofils et donc par une ingénierie de l'émission plus facile et un élargissement spectral d'émission plus faible. Cependant, la complexité de la région active tridimensionnelle rend le contrôle de l'homogénéité de la région active à l'échelle d'un fil unique très difficile. En particulier, le

changement de couleur d'émission avec le courant d'injection a été observé non seulement dans des nanofils auto-assemblés, mais aussi dans des LEDs à nanofils organisés. Le passage d'une géométrie 2D à une configuration 3D affecte aussi les propriétés électriques et optiques des LEDs.

### **Résumé des travaux réalisés aux LEDs à nanofils**

Je me focalise sur les structures LEDs cœur-coquille élaborées par épitaxie en phase vapeur aux organométalliques (MOVPE pour *Metal Organic Vapor Phase Epitaxy*) dans la direction parallèle à l'axe c du cristal wurtzite. L'optimisation des performances des dispositifs nanostructurés passe tout d'abord par une compréhension des propriétés de l'émetteur unique telle que leur composition (incluant les fluctuations de composition intra-fil à l'échelle nanométrique), leur activité optique, leurs propriétés électriques. Une étude fondamentale de ces aspects constitue la partie principale de mon travail exposé ici. Le fonctionnement de la LED macroscopique dépend aussi des caractéristiques de l'ensemble des nanofils telles que les fluctuations morphologiques et structurales d'un fil à l'autre, les chemins d'injection électrique dans le réseau de nanofils, les effets optiques collectifs, ... Dans ce chapitre j'adresserai brièvement les caractérisations électriques et optiques des ensembles de nanofils en utilisant la microscopie de courant induit par faisceau d'électrons (EBIC pour *electron beam induced current*) et la cartographie d'électroluminescence.

En ce qui concerne les émetteurs uniques, leurs propriétés ont été également étudiées en détachant les nanofils de leur substrat et en les contactant électriquement dans une géométrie planaire ou encore en contactant des nanofils individuels dans un ensemble utilisant des nanosondes dans un microscope MEB. Nous avons également utilisé la géométrie planaire pour analyser l'électroluminescence de nanofils uniques en fonction du courant d'injection pour différentes géométries de contact. Nous avons montré expérimentalement et en utilisant un simple modèle électrique, que pour une faible puissance, l'injection est plus favorable dans la région enrichie en indium tandis que le courant électrique se concentre sous le contact à forte puissance. Entre autres, nous en avons conclu que le spectre d'électroluminescence peut dépendre de la géométrie des contacts si la composition en indium n'est pas homogène dans la région active. Il est donc important d'analyser les nanofils uniques utilisant le même schéma de contactage que pour le dispositif à base d'ensemble de nanofils. En fabricant des LEDs à nanofils uniques verticaux avec un contact conforme, nous avons

montré que l'élargissement de l'électroluminescence (EL) pour les nanofils uniques est identique à celui de l'ensemble.

La dépendance de l'EL avec la géométrie des contacts mentionnée précédemment peut être utilisée pour contrôler la couleur d'émission des LEDs à nanofils avec une composition inhomogène lors de l'étape de fabrication. En effet, si une variation de composition dans la région active ne peut pas être évitée à l'étape de croissance, l'injection électrique dans des régions non-désirées peut être inhibée par un traitement dédié. Nous avons développé différentes procédures de contactage pour contrôler la couleur d'émission des LEDs présentant des régions enrichies en indium. L'inhibition de l'émission verte non-désirée a été obtenue en utilisant un traitement par plasma fluoré pour réduire localement la conductivité de la couche p.

En ce qui concerne l'analyse des propriétés électriques, il y a aujourd'hui un fort regain d'intérêt pour la microscopie de courant induit par faisceau d'électron. En effet, pour les matériaux nanostructurés les caractérisations macroscopiques ne fournissent que des valeurs moyennées des paramètres clés, ce qui n'est pas suffisant pour comprendre le fonctionnement du dispositif. En revanche, l'EBIC offre une résolution spatiale inégalée permettant d'analyser les propriétés structurales et électriques des nanofils individuels constituant la LED et en particulier de mettre en évidence les défauts de fonctionnement et d'en comprendre leur origine. La technique d'EBIC couplée avec la spectroscopie de cathodoluminescence permet de sonder à la fois les propriétés électrique et optique à l'échelle d'un fil unique. Nous avons analysé des nanofils clivés le long de leur axe pour sonder l'homogénéité de leurs propriétés électriques (e.g. homogénéité du dopage). Nous avons également pu corrélérer la décroissance du signal EBIC accompagnée d'une croissance du signal de cathodoluminescence vers le sommet des fils avec la variation de composition du puits quantique et de la couche de blocage d'électrons montrant que la chute du signal électrique est liée à une extraction moins efficace des porteurs dans les régions plus riches en indium. Finalement, nous avons identifié des anomalies électriques apparaissant dans certains fils à l'interface cœur/couche radiale dopée n qui sont associées à l'inhibition de l'électroluminescence. En changeant la procédure de fabrication pour injecter les électrons directement dans cette couche radiale et non pas dans le cœur du fil nous avons pu augmenter d'un facteur 3 le pourcentage de nanofils produisant de l'électroluminescence.

## **Photodétecteurs à base de nanofils nitrures**

### **Motivations**

Parmi les différents domaines spectraux, la gamme de l'ultraviolet est stratégique pour plusieurs applications industrielles, médicales, scientifiques, ou de sécurité etc. Pour la plupart des applications il est important de rejeter la lumière visible et ne détecter que la partie UV du spectre. Les semiconducteurs à large bande interdite comme les alliages AlGaN sont par nature aveugle à la lumière visible voire la lumière du soleil, ce qui permet d'en réaliser des détecteurs sans filtres supplémentaires pour rejeter la partie du spectre non-souhaité. Comme tout les autres composants optoélectroniques à couche minces de nitrures, la performance des détecteurs UV se dégrade du fait de la présence de dislocations. Dans ce contexte, au premier regard, le remplacement des couches bidimensionnelles par des nanofils peut être bénéfique.

La qualité cristalline du matériau n'est pas la seule motivation. Le développement de détecteurs à base de nanofil vise à exploiter des propriétés qui n'ont pas d'équivalent dans les détecteurs à couche mince. Les faibles dimensions des nanofils permettent la miniaturisation extrême. Ils peuvent potentiellement servir comme des sondes pour la microscopie en champ proche. On peut imaginer l'intégration des détecteurs à nanofils dans des plateformes fonctionnelles les utilisant pour des interconnexions optiques ou pour la détection photonique de molécules biologiques. Les détecteurs à nanofils ont été aussi mis en exergue pour réaliser des détecteurs de photons uniques. Organisés en matrices, les nanofils offrent la perspective de réaliser des imageurs sensibles avec des pixels ultra-petits pour atteindre une résolution spatiale à la limite de diffraction. Les propriétés de piégeage de la lumière dans l'ensemble ou de concentration de lumière dans des fils individuels sont avantageuses pour bénéficier de la forte absorption de la lumière avec une faible quantité de matériau actif.

Le nanofil constitue un élément de détection extrêmement sensible, où la séparation des porteurs photogénérés, la modulation de surface et la haute qualité cristalline permet d'atteindre des gains photoconducteurs inégalés excédant de plusieurs ordres de grandeur les valeurs atteintes pour les couches minces. Cette propriété est générique à plusieurs matériaux III-V et II-IV sous forme filaire. Comme je vais le discuter par la suite, la forte réponse des photoconducteurs à nanofils est directement lié avec le rapport surface/volume important. En ce qui concerne plus spécifiquement les nanofils de GaN, de nombreuses études expérimentales ont rapporté un fort gain photoconducteur. Certaines

études ont montré une photoconductivité persistante dans les nanofils GaN ou un photocourant dans le domaine du visible lié à des défauts, etc. Cependant, les études plus récentes n'ont pas relevé ces problèmes.

Je note aussi que malgré une quantité inépuisable de publications sur les photodétecteurs à nanofils, leurs performances en termes de bruit et de dérivité restent très peu étudiées. Des estimations basées sur leur comportement électrique ne sont pas très optimistes du fait d'un fort courant d'obscurité. Tout de même, on peut citer une valeur de dérivité égale à  $1.43 \times 10^{15} \text{ cmHz}^{1/2}\text{W}^{-1}$  rapportée dans la littérature pour un détecteur hybride nanofils/couche bidimensionnelle avec un traitement de passivation de la surface.

### **Photoconducteurs à base de nanofils de GaN**

La plupart des études de photoconducteurs à base de nanofils de GaN a été faite sur des nanofils uniques. Une forte dépendance du diamètre du fil a été observée et interprétée en terme de déplétion totale ou partielle de nanofil à cause du pinning du niveau de Fermi en surface. Toutes ces études montrent un gain photoconducteur extrêmement élevé

En ce qui concerne les ensembles de nanofils, il existe peu de travaux. Dans notre groupe, nous avons fabriqué un photodétecteur à base d'ensemble de nanofils GaN épitaxiés par MBE dans l'équipe du Prof. L. W. Tu à Taiwan. Le schéma du détecteur est montré dans la figure 1 a). Les fils sont conservés sur leur substrat (Si(111) dopé n), encapsulés partiellement dans un diélectrique et contactés en surface avec un matériau transparent. A cette époque, nous nous étions intéressés à l'optimisation des contacts à base de graphène pour améliorer la transparence dans la gamme spectrale UV. Nous avons déposé une couche de graphène sur le sommet des fils qui a été structurée par lithographie optique et gravure plasma. La figure 1 b) montre une image MEB de la région contactée (les nanofils sont visibles à travers la couche de graphène). Il s'avère que le graphène n'est pas bien adapté pour ce type d'application car il reste suspendu sur les fils les plus hauts et ne contacte qu'une partie des nanofils. Néanmoins nous avons pu analyser les performances du dispositif. Comme le montre l'insert de la figure 1 c), le détecteur répond uniquement à la partie UV du spectre pour des énergies supérieures à 3 eV (ce qui prouve que le substrat Si ne contribue pas au photocourant). La réponse ne montre pas de décroissance à haute énergie jusqu'à 4,2 eV ce qui laisse penser que la transparence a été effectivement améliorée en comparaison du contact ITO.

La magnitude de la réponse a été mesurée. Elle atteint 25 A/W à 1 V à la longueur d'onde de  $\lambda=365$  nm. L'efficacité quantique est de 1 pour une réponse de 0,29 A/W, ce qui veut dire que le détecteur présente un gain photoconducteur de  $10^2$ . Le gain est bien inférieur aux valeurs rapportées pour des fils uniques. Il peut y avoir deux raisons : (i) le contact graphène ne touche qu'une faible fraction des nanofils, les autres fil ne sont pas contactés et (ii) la réponse des détecteurs à fil unique est systématiquement surestimée en sous-estimant leur surface effective de l'absorption (il est de coutume de prendre la surface égale à la surface projetée du nanofil sans tenir compte de la section d'absorption plus large pour ces objets sub-longueur d'onde). La réponse diminue avec la puissance optique incidente). La décroissance de la réponse à haute puissance peut se comprendre par la saturation du deuxième terme dans l'équation (\*) : la surface de conduction ne peut pas excéder la section du nanofil, il y a donc bien une limite supérieure à la modulation de la région dépliée surfacique.

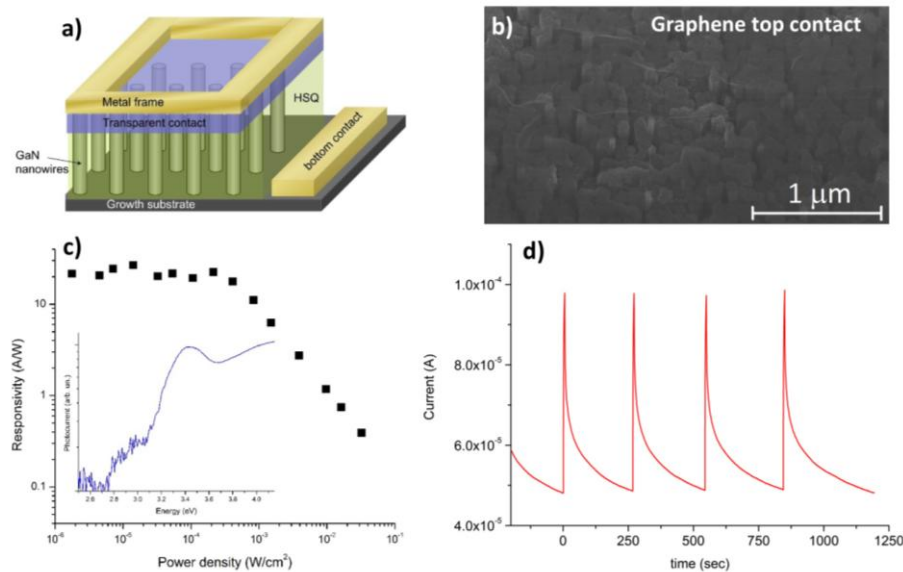


Figure 1. a) Schéma du photoconducteur à base d'ensemble de nanofils GaN. b) Image MEB montrant la morphologie du contact graphène. c) Réponse du détecteur en fonction de la densité de puissance. L'insert montre le spectre de photocourant. d) Réponse temporelle à des impulsions de lumière d'une durée de 5 s.

Le comportement temporel du détecteur montré dans la figure 1 d) est catastrophiquement lent. Le temps de retour à l'équilibre se chiffre en centaines de secondes, montrant que les nanofils sont sujets

au phénomène de la photoconductivité persistante. Je note tout de même que des temps caractéristiques plus courtes (quelques centaines de millisecondes) ont été rapportés pour des fils uniques à structure n-i-n. D'après le modèle de Calarco, le temps de retour à l'équilibre dépend fortement du diamètre des fils et de leur dopage, ce qui peut expliquer la différence entre nos observations et les résultats de la littérature.

### **Photodiodes p-n radiaux à base de nanofils de GaN/InGaN**

Pour un grand nombre d'applications la vitesse de fonctionnement est un paramètre important. La section précédente montre qu'il est difficile de se débarrasser des effets lents liés aux processus de surface si on utilise des photodiodes à géométrie axiale. Les hétérostructures cœur/coquille sont des bons candidats pour protéger la génération et le transport des porteurs des phénomènes de surface.

Nous avons étudié des photodétecteurs à base de nanofils uniques contenant une hétérostructure radiale n-p. Ces échantillons étaient dédiés à la réalisation de connexions optiques dans le domaine spectral du visible entre des émetteurs et détecteurs à base de nanofils couplés par des guides d'onde. Des puits quantiques InGaN ont été donc insérés dans la jonction p-n. Les nanofils ont été fabriqués par MOVPE au CEA-Grenoble dans le cadre de la thèse GaNEx d'A. Messanvi. La structure des échantillons illustrée dans l'insert de la figure 2 b) est similaire à celle des nanofils LED discuté dans le chapitre III suivant. Les fils sont composés d'un tronc GaN fortement dopé n ayant une surface latérale libre et d'une partie supérieure cœur/coquille contenant un cœur n-GaN, 30 puits quantiques  $\text{In}_{0,18}\text{Ga}_{0,82}\text{N}/\text{GaN}$  et une coquille p-GaN.

Les fils uniques ont été contactés en utilisant soit des rubans métalliques localisés soit des contacts étendus en graphène ou ITO. Les tendances sont similaires pour les différents contacts. Dans la suite, je discute l'exemple des fils contactés par une couche d'ITO avec la morphologie des nanofils contacté montré sur la figure 2 a). La base en GaN fortement dopé n est contacté avec un ruban métallique, tandis que la région cœur/coquille est couverte par le contact transparent en ITO.

Les photodétecteurs présentent un comportement rectifiant. La figure 15 b montre les courbes I-V dans l'obscurité et sous illumination avec une diode laser à 370 nm. La réponse sous tension nulle est de 0,14 A/W (prenant pour le calcul la surface de la région cœur/coquille). On constate que pour des tensions positives le photocourant s'inverse et atteint des valeurs très élevées.

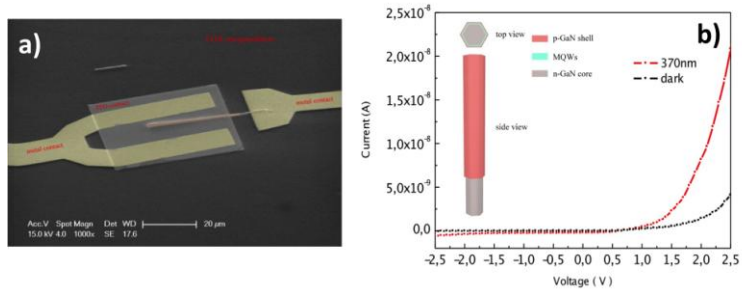


Figure 2. a) Image MEB d'un photodiode à nanofil unique cœur/coquille InGaN/GaN. b) Caractéristiques I-V dans l'obscurité et sous éclairage avec une diode laser  $\lambda=370$  nm. L'insert montre le schéma de la structure des nanofils.